Doctoral Dissertation

SURFACE REACTION MECHANISMS OF PLASMA-ENHANCED ATOMIC LAYER ETCHING FOR SILICON NITRIDE

TERCERO JOMAR UNICO

International Program of Materials and Manufacturing Science

Division of Materials and Manufacturing Science

Graduate School of Engineering

OSAKA UNIVERSITY

Japan

July 2024

Acknowledgments

I would like to thank Professor Satoshi Hamaguchi for his guidance, support, and encouragement throughout my Ph.D. His insights, comments, and suggestions have greatly improved this research and contributed to my academic growth.

I am also grateful to my mentors, Nicolas Mauchamp and Michiro Isobe, for introducing me to the research group's MD simulation code. Their guidance has been crucial in refining this research. I would also like to thank our collaborators, Dr. Masanaga Fukasawa and Dr. Akiko Hirata from Sony Semiconductor Solutions Corporation, for providing the experimental support to compare my calculations and for their important contributions to this research.

Thank you to my labmates for their help and support. I also want to acknowledge Umemura-san, our lab secretary, for her assistance with official matters and language support.

I am grateful to the QLEAR Fellowship for the financial support that made this research possible and for offering activities that greatly benefit its members.

Finally, I want to express my deepest gratitude to my family for their love and support, and to God for giving me strength and guidance throughout this journey.

Abstract

As semiconductor devices continue to become smaller and incorporate more complex 3D structures, the demand for highly precise nano-scale fabrication has significantly increased. This growing need has led to a strong interest in advanced etching techniques. Atomic layer etching (ALE) has emerged as a key method for achieving atomic-scale precision. This level of control is particularly useful in addressing the challenges of modern semiconductor manufacturing.

In this study, molecular dynamics (MD) simulations were performed to explore the etching mechanisms during plasma-enhanced atomic layer etching (PE-ALE) of silicon nitride (SiN) surfaces. Recent experiments have shown that the PE-ALE process, involving hydrofluorocarbon (HFC) adsorption followed by argon ion (Ar^+) irradiation, can lead to an etch-stop phenomenon. The simulations revealed that carbon (C) remnants at the end of a PE-ALE cycle can result in further C accumulation in subsequent cycles. Under typical Ar^+ ion irradiation conditions, nitrogen (N) atoms are preferentially removed over silicon (Si) atoms. This selective removal increases the Si-richness of the SiN surface, thereby promoting C accumulation through the formation of Si-C bonds. Additionally, fluorine (F) atoms facilitate Si removal, whereas hydrogen (H) and C atoms contribute to N removal from the SiN surface.

Additionally, the influence of introducing oxygen (O) ion irradiation at the

end of each cycle of the SiN PE-ALE process was examined to address etch-stop caused by excessive HFC polymer accumulation. This thick polymer layer blocks and obstructs ion impact during the desorption step. To prevent etch-stop, an oxygen (O_2) plasma irradiation step was added after the desorption step of the conventional two-step SiN PE-ALE process. Differences between the conventional two-step and the modified three-step PE-ALE processes, which include the O_2 plasma irradiation, were discussed. In the simulations, low-energy CH_2F radicals were deposited on the SiN surface during the adsorption step. The modified surface was then irradiated with energetic Ar^+ ions and subsequently etched in the desorption step. In the additional O_2 plasma irradiation step, the resulting surface was irradiated with low-energy O species, which removed excess C atoms by promoting the formation of volatile CO molecules. This O irradiation step was found to effectively prevent C layer accumulation on the surface.

Further simulations were performed to examine the interactions between the SiN surface and various inert gas ion irradiations, including Ar^+, krypton (Kr^+), and xenon (Xe^+). Changes in surface height, penetration depths of HFC species, and thickness of the damaged layer over several PE-ALE cycles were observed. The results showed that Ar^+ ions etched the SiN surface more efficiently than Kr^+ or Xe^+ ions under the same conditions. The slower etching rates observed with Kr^+ or Xe^+ ion irradiation were attributed to the accumulation of HFC species. Despite these differences in etching efficiency, the thickness of the damaged layers showed no significant differences when Ar^+, Kr^+, and Xe^+ ions were used in the desorption step.

Contents

Chapter 1

Introduction

This introduction provides an overview of the study's background, including the primary research focus and methodologies employed. The study focuses on Plasma-enhanced Atomic Layer Etching (PE-ALE) techniques. The material of interest, silicon nitride (SiN), is studied in depth, as are the challenges and problems associated with its PE-ALE processing. The main objectives and limitations of the study are also emphasized, for an in-depth analysis of the subject matter.

Background of the Study

1.1 Atomic Layer Etching

Atomic Layer Etching (ALE) is a sophisticated etching process used in the semiconductor industry to create micro- and nano-scale structures with atomic-level precision. ALE uses a controlled, layer-by-layer material removal procedure, similar to Atomic Layer Deposition (ALD), which deposits material in the same way. This level of accuracy is essential for producing the fine features required in current semiconductor devices like transistors and memory cells [1, 2].

The ALE process consists of two cyclical self-limiting steps: adsorption and desorption. During adsorption, a reactive gas or plasma alters and modifies the substrate surface layer. This is followed by desorption or removal step to selectively remove the modified surface layer, etching one atomic layer at a time, ideally. These series of steps are repeated, providing fine control over the etching process while minimizing damage to the underlying material.

ALE has various advantages, including atomic-level precision, high selectivity, minimal damage, and uniformity across large surfaces. These characteristics make ALE excellent for manufacturing modern semiconductor devices such as FinFETs, DRAM, and NAND flash memory. This approach is also utilized in nanotechnology to create nanoscale devices and surface engineering to improve the characteristics and performance of existing semiconductor device technologies.

1.2 Plasma-enhanced Atomic Layer Etching

Plasma-enhanced atomic layer etching (PE-ALE) is a highly precise technique used in the semiconductor industry to remove material surfaces layer-by-layer. This technique allows to satisfy the current needs of the semiconductor industry, where the devices become smaller and more complex, and the demand for such high-precision fabrication methods has significantly increased.

The PE-ALE technique is a set of cyclic steps involving sequential and self-limiting surface reactions, enabling exceptional control over etching at the atomic scale [1–4]. Each cycle typically consists of two steps: an adsorption step in which reactive precursors adsorb onto the material surface, and a desorption step in which low-energy inert-gas ion irradiation, such as Ar ions, is use to remove or etch the modified surface layer. Figure 1.1 shows the ideal scenario for a PE-ALE process: etching a monolayer of the material's surface following one cycle of adsorption and desorption steps. In contrast, Fig. 1.2 shows a more realistic case where more than a monolayer of the material's surface was etched.

This cycles allows for achieving anisotropic etching with atomic-scale accuracy, which is essential to etch very thin surface layer. The ability to control the etched depth in each cycle by adjusting the number of cycles is a significant advantage, providing great control over the device fabrication process.

In a stable process, the total number of PE-ALE cycles can precisely control the overall etched depth, where the etched depth in each cycle stays almost constant over a longer number of cycles. The depth of etching obtained in a single PE-ALE cycle is referred to as etch-per-cycle (EPC). The EPC should ideally stay constant over the course of the cycle. On the other hand, extending the cycle time or the length of the desorption step does not further enhance the etched depth

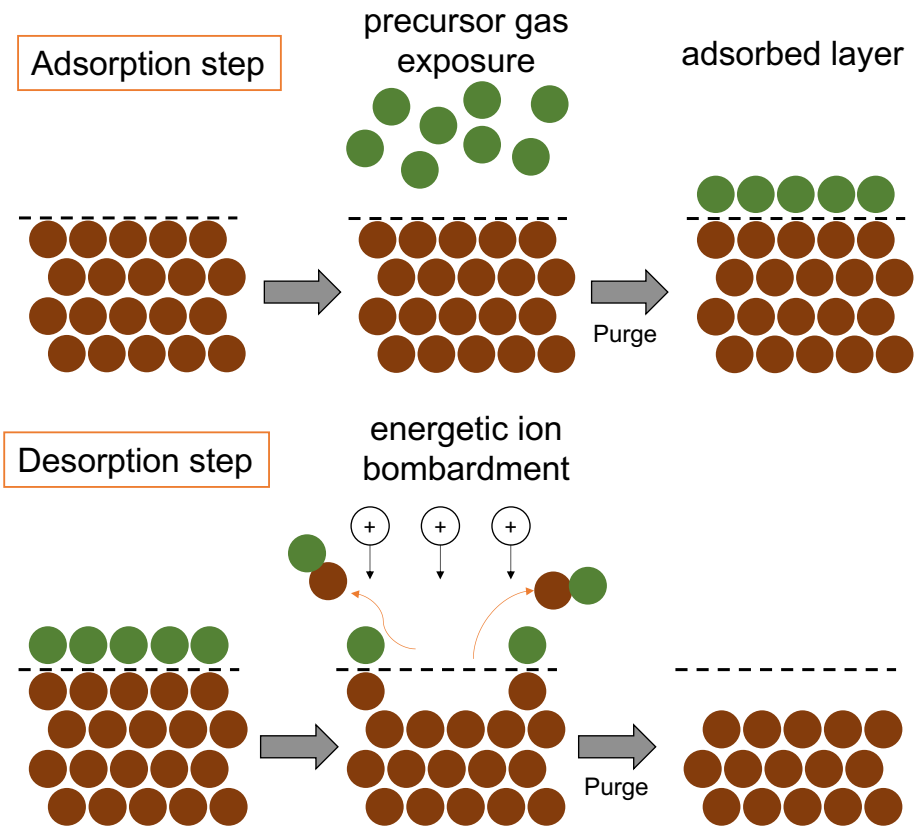

Figure 1.1: A schematic representation of an ideal PE-ALE process, demonstrating the removal of a monolayer from a material's surface following the adsorption and desorption steps.

once a particular etched depth is attained. This type of behavior is referred to be a "self-limiting" mechanism.

PE-ALE has been extensively studied for materials like silicon (Si) [5–9], silicon dioxide (SiO_2)[10–15], and silicon nitride (SiN) [16–23]. In 1990, Horiike et al. presented the Si PE-ALE process for the first time for semiconductor applications, using Ar plasma irradiation and halogen adsorption [24]. Since then, plenty of research has been done on chlorine-based PE-ALE methods for Si, demonstrating the usefulness of the method for achieving efficient etching performance. Similar methods have been used to SiO_2 and SiN, proving the adaptability of PE-ALE

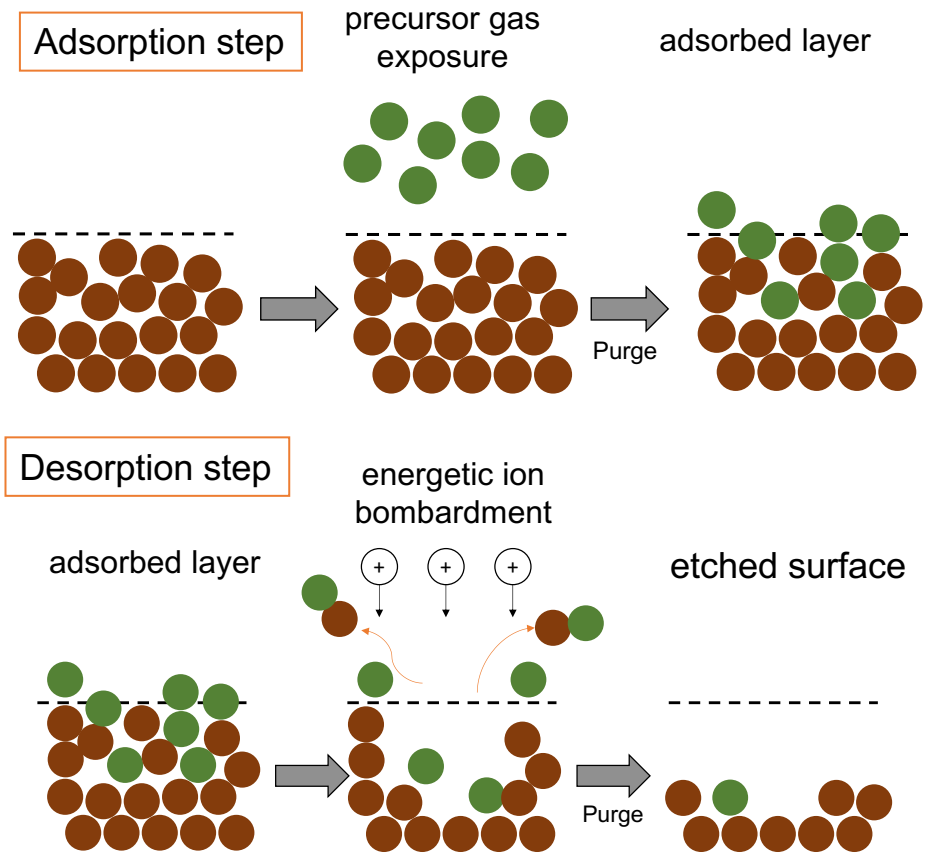

Figure 1.2: A schematic representation of an "actual" PE-ALE process, showing an imperfect material surface and the removal of more than a monolayer from a material's surface after adsorption and desorption steps.

process in the manufacturing process of semiconductors.

1.3 Silicon Nitride

Silicon nitride (SiN) is a covalently bonded compound known for its unique properties, making it adaptable to a wide range of applications. In the semiconductor industry, SiN is commonly used as etch masks and spacers because of its excellent characteristics[25–28]. These properties are essential in integrated circuit fabrication, where SiN protects underlying layers from the corrosive effects of etchants employed in precise material removal processes.

SiN plays an important role in the manufacturing process, allowing for higher storage density and performance in modern semiconductor technologies such as 3D NAND memory. In 3D NAND technology, memory cells are stacked vertically to maximize the use of device area, which improves performance by increasing the number of devices on a semiconductor. SiN acts as a stable dielectric layer that isolates and separates memory layers [29–31]. Its resistance to high temperatures and and chemical stability ensures the integrity and durability of NAND flash memory devices, allowing them to satisfy the demanding needs of modern data storage applications.

Furthermore, SiN's application shows its importance in semiconductor development. Beyond etch masks and spacers, SiN's characteristics make it essential for ensuring the functionality and longevity of semiconductor components. Its ability to withstand extreme processing conditions and resist chemical corrosion demonstrates its continues importance in advancing semiconductor technologies and expanding electronics and data storage capabilities.

1.4 Challenges in Silicon Nitride PE-ALE

Despite its benefits, PE-ALE faces challenges. One significant issue is the occurrence of etch stops, caused by the accumulation of residual species, such as carbon, on the etched surface [32–34]. These residues can impede the ion impact during the desorption step, causing etch stop of the PE-ALE process. Carbon accumulation is particularly problematic when using hydrofluorocarbon (HFC) precursors during the adsorption step, as seen in PE-ALE processes for SiN[23]. Therefore, understanding the mechanisms of etching and formations of C accumulations, as well as developing methods to prevent such issues are essential to improve the PE-ALE process technologies.

As previously discussed, precise control of etch selectivity and damage reduction become more and more important as devices get smaller. The excessive accumulation of carbon from HFC precursors creates a major challenge in SiN PE-ALE process because they prevent effective ion bombardment during the desorption step. Possible solutions have been proposed by researchers, such as adding extra steps like O_2 plasma irradiation, which has been demonstrated to reduce carbon buildup and increase stability throughout the etching process [13, 35]. Therefore, in order to improve the current SiN PE-ALE process and achieve efficient etching performance, it is essential to have an extensive knowledge of surface interactions at the atomic level.

1.5 Objectives of the Study

The main objectives of this study are as follows:

(a) **Study the Etch-Stop Mechanisms in SiN PE-ALE**

- Use classical MD simulations to understand the etch-stop mechanism observed in SiN PE-ALE process.
- Study the surface modification and adsorption of HFC and understand its influence on the SiN PE-ALE process.
- Investigate the surface etching mechanisms during the Ar^+ ion irradiation step.

(b) **Investigate the Role of O ions in Mitigating Etch-stop in SiN PE-ALE process**

- Explore the effects of the additional O_2 plasma irradiation step to prevent etch-stop in SiN PE-ALE process.
- Evaluate the efficiency of the three-step PE-ALE process in removing the HFC layer and study the role of O atoms in preventing C accumulation by facilitating the formation of CO species.

(c) **Evaluate the Impact of Different Inert-Gas Ions in SiN PE-ALE process**

- Perform MD simulations to analyze the etching efficiency and surface damage formations in SiN PE-ALE process by employing various inert-gas ions (Ar^+, Kr^+, Xe^+) during the desorption step.

- Determine the etched depth and the extent of C layer accumulation and surface damage over multiple PE-ALE cycles for each inert gas ion.

1.6 Scope of the Study

This study aims to investigate various aspects of the SiN PE-ALE process using classical MD simulations. Firstly, it aims to understand the etch-stop mechanism observed in the SiN PE-ALE process, focusing on the interaction between the SiN surface and H-rich hydrofluorocarbon species, represented by CH_2F, and F-rich hydrofluorocarbon species, represented by CHF_2 radicals. These reactive species play an important role in understanding the etch-stop phenomenon.

Secondly, this research aims to study the surface reaction mechanisms occurring during the Ar^+ ion irradiation step. By examining the removal of the HFC layer, chemically enhanced etching of SiN, and physical sputtering of SiN, this research aims to understand the complex dynamics of species adsorption, which involves surface modification, and desorption, which involves removal and etching of surface species.

Furthermore, this research aims to study the influence of adding the O_2 plasma irradiation step, thereby modifying the conventional two-step process into a three-step PE-ALE process. It seeks to understand how this addition helps prevent the previously observed etch-stop. By introducing O ions in the simulations, the study aims to prevent the accumulation of carbon species and enhance the stability of the etching process.

Lastly, this research evaluates the impact of different inert-gas ions (Ar^+, Kr^+, Xe^+) and aims to understand their etching efficiency and the formation of surface damage on the SiN material during the SiN PE-ALE process. This is achieved by comparing the etched depth, extent of carbon layer accumulation, and surface damage induced by each inert gas ion over multiple PE-ALE cycles.

However, like any other research, this study has its limitations. For the reactive

species, we cannot consider all the radicals present in the plasma. To simplify the process, we have only considered two HFC radicals (CH_2F and CHF_2) to represent the HFC species and their interactions with the surface. Additionally, charge distributions are not considered in the simulations due to the complexity of the calculations. Therefore, in our simulations, all species were assumed to be charge neutral or was treated as fast neutrals.

Chapter 2

Molecular dynamics simulations

This chapter focuses into the underlying concepts of molecular dynamics (MD) simulations, as well as the techniques, algorithms, and tools that make this method applicable in a wide range of scientific areas. It also covers fundamental subjects such as energy conservation and ensemble theory, which serve as the foundation for a complete understanding of the technique's applications and limitations.

2.1 Basic Principles and Implementation

2.1.1 Overview and Workflow

MD simulations is a powerful computational technique widely utilized in a variety of scientific research across diverse disciplines. Originating from the pioneering work of Alder and Wainwright in 1957 [36], MD has since developed into an advanced technique to study the dynamic behavior of atoms and molecules in complex systems. The fundamental principles of MD is based on the numerical integration of Newton's equations of motion to simulate or model the trajectories of particles within a defined system. The interatomic interactions in these simulations are described by empirical force fields, parameterized based on experimental observations and quantum mechanical calculations [37–40].

Newton's fundamental equation of motion describes the movement of particle i with mass m at position r and force F:

$$\frac{d^2 r_i}{dt^2} = \frac{F_i}{m_i} = -\nabla U(r_i), \tag{2.1}$$

in which the gradient of the potential energy function $U(r_i)$ with respect to the position r_i is represented by $\nabla U(r_i)$.

MD simulations have been extensively used in chemistry, physics, materials science, and biology. They yield insights into the structural features, dynamic processes, and thermodynamic behaviors of molecular systems under various conditions. Beyond fundamental research, MD simulations are crucial in drug development, materials design, and nanotechnology. Integrating computational models with real-world data fosters interdisciplinary collaboration, accelerating scientific advancements and innovations in fields ranging from pharmaceuticals to

materials science.

2.1.2 Algorithms and softwares

In classical molecular dynamics (MD) simulations, key approaches include the Verlet and Velocity Verlet algorithms, which are essential for accurately calculating the trajectories of particles over time. The Leapfrog algorithm is another popular method, offering computational efficiency and stability. These approaches solve Newton's equations of motion for particles, allowing for the simulation of complex molecular systems. Efficient energy minimization techniques, such as the steepest descent and conjugate gradient methods, are also crucial for preparing initial configurations.

Several software packages are widely used for classical MD simulations. GROMACS is known for its speed and flexibility, making it ideal for simulating biomolecular systems[41]. LAMMPS (Large-scale Atomic/Molecular Massively Parallel Simulator) excels in simulating materials science problems due to its ability to handle large-scale systems and various interatomic potentials[42]. AMBER is a suite of programs primarily designed for biomolecular simulations, offering robust tools for modeling proteins and nucleic acids[43]. For this study, an in-house code tailored to study ion–surface interactions during plasma processes was used. These software tools provide comprehensive features for setting up, running, and analyzing MD simulations.

2.2 Atomic Interactions and Potentials

2.2.1 Force fields and Interatomic Potentials

To mimic the behavior of material systems, a variety of potential functions are used. The selected interatomic potential determines how particles interact with one another and impacts the behavior of the simulations. The Lennard-Jones potential, shown in Equation 2.2, is a potential model that characterizes the attraction and repulsion between particles according to their distance from one another.

$$U(r) = 4\epsilon \left(\left(\frac{\sigma}{r}\right)^{12} - \left(\frac{\sigma}{r}\right)^{6} \right) \tag{2.2}$$

Two terms make up the Lennard-Jones potential equation: the first one denotes repulsion and the second one, attraction. Figure 2.1 [44] shows the energy versus distance curve for the Lennard-Jones potential, which shows the ideal distance between particles when the net force is zero.

In classical MD simulations, most interactions are described by an interatomic potential function given by

$$\Phi = \Phi(r_i) = \Phi(r_1, r_2, r_3, \ldots, r_N) \tag{2.3}$$

where r_i represents the position of the ith atom and N is the total number of atoms in the system.

The total potential energy is commonly expressed using a Taylor series expansion:

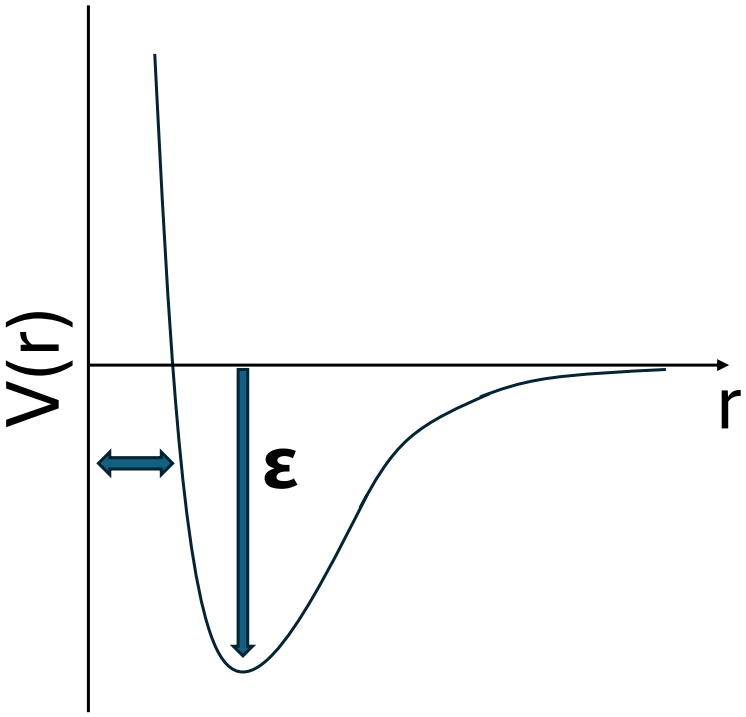

Figure 2.1: The relationship between energy and distance in an LJ potential.

$$\Phi = \sum_{i} v_1(r_i) + \sum_{i<j} v_2(r_i, r_j) + \sum_{i<j<k} v_3(r_i, r_j, r_k) + \dots \tag{2.4}$$

It was proposed by Stillinger and Weber [45] that the combination of two-body (v_2) and three-body (v_3) potential terms optimally represents the total potential energy of a system. For instance, the potential functions for Si-O-Cl and Si-O-F systems are created, expressing the total energy as a sum of the two and three-body potentials, in silicon-based materials characterized by strong and directional atomic bonding. The Stillinger-Weber-type potential functions for these Si-O-Cl and Si-O-F systems were specifically developed by Ohta et al. (2001) [46], where the total energy is represented by the sum of the two and three-body potentials, as given by

Interaction	a (eVÅ^{2q})	b	q	d(Å)	r_c
Si-Si	170.0	38.3	1.89	0.614	3.6
N-N	76.9	24.7	1.69	1.14	2.4
Si-N	425.042	83.5068	1.7302	1.6060	2.99

Table 2.1: Parameters of the two-body potentials for Si-Si, N-N, and Si-N.

$$\Phi = \sum_{i<j} v_2(\mathbf{r}_i, \mathbf{r}_j) + \sum_{i<j<k} v_3(\mathbf{r}_i, \mathbf{r}_j, \mathbf{r}_k) \tag{2.5}$$

where

$$v_2(\mathbf{r}_i, \mathbf{r}_j) = a r_{ij}^{-2q} exp\left(\frac{2d}{r_{ij} - r_c}\right) - b r_{ij}^{-q} exp\left(\frac{d}{r_{ij} - r_c}\right) \tag{2.6}$$

If $r_{ij} < r_c$, then this is true; otherwise, $v_2 = 0$. Where r_c is the cut-off distance, and a, b, d, and q are parameters based on the element type of the ith atom in the equation.

Figure 2.2 shows the curves for Si-Si, N-N, and Si-N interactions that are present in the system. Using Eq. 2.6, the parameters a, b, q, d, and the cutoff distance, r_c , were calculated. These values depend on the i and j atomic species. Table 2.1 shows the some of the parameter values for two-body interactions.

For the three-body interaction, the potential term is given by:

$$\begin{aligned} v_3(\mathbf{r}_i, \mathbf{r}_j, \mathbf{r}_k) = & h_{jik}(r_{ij}, r_{ik}, \theta_{jik}) \\ & + h_{ijk}(r_{ji}, r_{jk}, \theta_{ijk}) \\ & + h_{ikj}(r_{ki}, r_{kj}, \theta_{ikj}) \end{aligned} \tag{2.7}$$

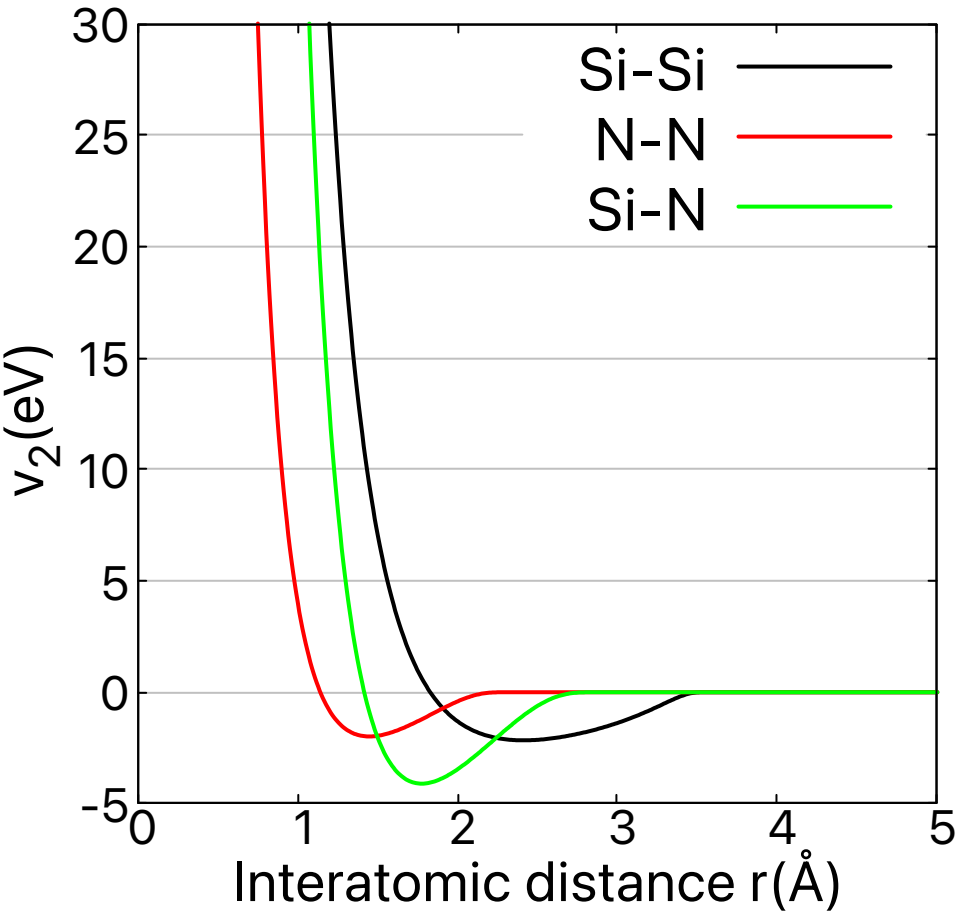

Figure 2.2: Two-body potential as a function of the interatomic distance for Si-Si, N-N, and Si-N interactions.

The angle between the i$^{\text{th}}$, j$^{\text{th}}$, and k$^{\text{th}}$ atoms is represented by θ_{jik} in this case, and the distance between the i$^{\text{th}}$ and j$^{\text{th}}$ atoms is indicated by r_{ij}. In this case, θ_{ijk}, $\mathrm{r_{ji}}$, $\mathrm{r_{jk}}$, and $\mathrm{h_{ijk}}$) are given by,

$$h_{ijk}(r_{ji}, r_{jk}, \theta_{ijk}) = k_{ijk} \left|\cos\theta_{ijk} - \Theta_{ijk}\right|^{\gamma_{ijk}} f_{ij}(r_{ij}) f_{jk}(r_{jk}) \tag{2.8}$$

where the parameters k_{ijk}, θ_{ijk}, and Θ_{ijk} are element-type-dependent. $f_{ij}(r_{ij})$ is a smoothing function in this equation, where $f_{ij}(r_{ij}) = 0$ if $r_{ij} \geq r_c$ and $f_{ij}(r_{ij}) = 1$ if $0 < r_{ij} << r_c$. Once more, the cut-off distance between the i$^{\text{th}}$ and j$^{\text{th}}$ atoms is denoted by r_c. Furthermore, $v_2(\mathbf{r}_i, \mathbf{r}_j)$ can be used to further define the function $f_{ij}(r_{ij})$, such that

$$f_{ij}(r_{ij}) = \begin{cases} 1, & \text{if } r_{ij} \leq r_{\min} \\ \dfrac{v_2(\mathbf{r}_i, \mathbf{r}_j)}{v_{2,\min}}, & \text{if } r_{\min} < r_{ij} < r_c \\ 0, & \text{if } r_{ij} \geq r_c \end{cases} \tag{2.9}$$

2.2.2 Periodic Boundary Conditions

To simulate small systems, periodic boundary conditions (PBC) are typically used to replicate or mimic bulk materials and represent the atomic movements within the bulk. PBC are commonly employed in the x and y directions, or depending on the preferred orientation, of the simulation box to represent an infinitely wide surface in material system simulations. To compute and examine the bulk properties, a small portion of the material is built and replicated infinitely in predetermined directions [47, 48]. The atoms at the edges of the simulation box interact with atoms in adjacent boxes or their replicas. When an atom leaves the primary cell, a similar atom enters from the other side of the boundary, as seen in Fig. 2.3.

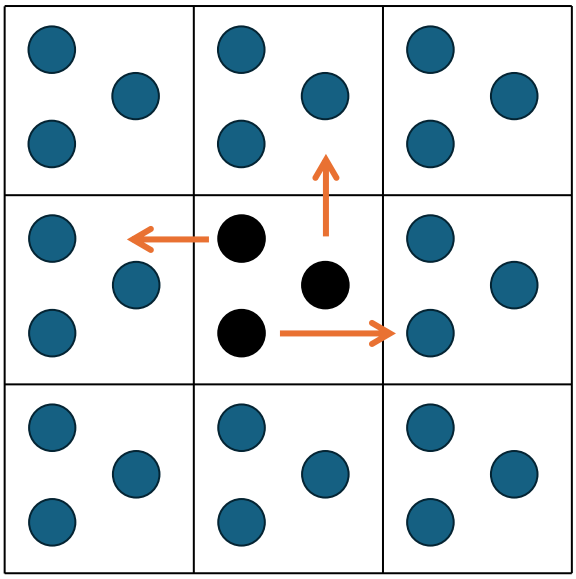

Figure 2.3: Under periodic boundary conditions, when a particle exits the simulation box, it is replaced by an image particle entering from the opposite side. Both real and image neighbors are included when computing particle interactions within the given cutoff range.

2.2.3 Verlet Algorithm

In the past, scientists tried out different ways to solve Newton's equations of motion. These equations describe how things move when forces act on them. One popular method they found is called the Verlet algorithm. It is extensively employed, particularly in investigations of the motion of molecules[37]. The velocity Verlet method is an additional variation of this technique that is also very helpful. It is useful in determining not only the location of particles but also their velocity and acceleration[49]. This approach is well-known for maintaining accuracy and consistency over the course of a simulation.

$$p_i\left(t+\frac{1}{2}\delta t\right) = p_i(t) + \frac{1}{2}\delta t f_i(t) \tag{2.10}$$

$$r_i(t+\delta t) = r_i(t) + \frac{\delta t}{m_i} p_i\left(t+\frac{1}{2}\delta t\right) \tag{2.11}$$

$$p_i(t+\delta t) = p_i\left(t+\frac{1}{2}\delta t\right) + \frac{1}{2}\delta t f_i(t+\delta t) \tag{2.12}$$

In the given equations, p is the momentum, r is atomic position, t is time, and m is the atomic mass. These equations work by first determining the forces acting on the particles, and then updates their positions and velocities at regular intervals, δt. Using this, the atoms movement and its changes over time can be modeled.

During the computations, few things are needed to considered. First, the dynamical properties during the system evolution at predetermined time scales must be predicted accurately to confirm that the long-term predictions could be accurate. Second, it must ensured that the energy of the system is conserved during this process[48]. During the calculations, the simulation time is continuously updated until the specified simulation period is reached.

2.3 Energy Conservation and Ensembles

2.3.1 Energy calculations and conservation

Energy calculations and conservation are essential in classical MD simulations. The total energy of a system is divided into kinetic and potential energy components, with accurate calculations ensuring system stability and physical realism. Energy conservation is achieved through algorithms such as the Verlet and Velocity Verlet methods, which update particle positions and velocities while minimizing numerical errors. These algorithms help preserve the system's overall energy over time, which is crucial for the reliability and accuracy of simulations.

2.3.2 Common ensembles (NVE,NVT,NPT)

- The NVE (constant Number of particles, Volume, and Energy) ensemble, also known as the microcanonical ensemble, keeps the number of particles, volume, and total energy fixed throughout the simulation. This ensemble is ideal for studying isolated systems where energy conservation is crucial, as it does not exchange energy with its surroundings. The NVE ensemble is often used to observe the natural evolution of a system without external influences. In practice, the Verlet or Velocity Verlet algorithms are commonly employed to maintain energy conservation in NVE simulations[50].

- The NVT ensemble, also known as the canonical ensemble, has a constant number of particles, volume, and temperature. This is accomplished by using thermostat algorithms such as the Berendsen thermostat and the Langevin thermostat to regulate the system's temperature and keep it within a specified range. The Berendsen thermostat gradually adjusts the

temperature to the desired value, whereas the Langevin thermostat incorporates stochastic forces and friction to simulate the interaction with an implicit heat bath, resulting in more accurate temperature control in some instances. The NVT ensemble is excellent for investigating systems at equilibrium when thermal impacts are significant, as it allows for the simulation of more realistic conditions by simulating a system in contact with a heat bath[51, 52].

- The NPT ensemble, also known as the isothermal-isobaric ensemble, keeps the number of particles, pressure, and temperature constant. This ensemble uses both a thermostat and a barostat to regulate the system's temperature and pressure, allowing the volume to be adjusted as needed. It is especially useful for modeling realistic settings when both temperature and pressure change, as in the study of phase transitions and material properties under various climatic conditions. By precisely regulating these factors, the NPT ensemble provides a more complete knowledge of a system's behavior in a variety of real-world situations[53].

Chapter 3

Etch-stop mechanisms in PE-ALE of SiN

3.1 Introduction

As the dimensions of advanced semiconductor devices continue to diminish and complex three-dimensional device structures are employed, the demand for high-precision fabrication of nano-scale devices has increased significantly. Plasma processes [54–59] such as plasma-enhanced chemical vapor deposition (PE-CVD),[60, 61] physical vapor deposition (PVD),[62–65] and reactive ion etching (RIE)[66–68] have been widely used to deposit functional materials and fabricate complex device structures by transferring mask patterns to the material surfaces. As a technique to achieve anisotropic etching processes with atomic-scale accuracy, plasma-enhanced atomic layer etching (PE-ALE) has attracted much attention from those working in advanced semiconductor manufacturing. In a PE-ALE process, the material surface is etched atomic-layer by atomic-layer ideally or, at least, thin-layer by thin-layer.

[1–8, 10–15, 18, 20–24, 33, 35, 69–76]

PE-ALE processes consist of cyclic processes involving sequential and typically self-limiting surface reaction processes. In a typical ALE process, each cycle consists of two steps (i.e., half-cycles), i.e., the adsorption step, where reactive precursors are adsorbed on the material surface, and the desorption step, where surface reactions form volatile species containing atoms of the surface material and therefore surface etching occurs. In PE-ALE, argon (Ar^+) ion irradiation from an Ar plasma is typically used to cause the desorption of surface materials although other inert-gas ions such as Krypton (Kr^+) or xenon (Xe^+) ions can also be used in this step.[77] The energy of the incident inert gas ions is ideally set high enough to etch the surface with adsorbed reactive species, but low enough not to etch the pristine material surface. In this way, once the adsorbed reactive species are nearly exhausted, the etching stops and thus a self-limiting desorption of the surface material can be achieved.

For semiconductor process applications, Horiike et al. performed PE-ALE processes of silicon (Si), using halogens in the adsorption step and Ar plasma irradiation in the desorption step [5, 24]. Subsequently, extensive research was performed on PE-ALE processes of Si with chlorine (Cl) adsorption. [6–8, 74, 76] The technique was also extended to PE-ALE of silicon dioxide (SiO_2)[10–15, 33] and silicon nitride (SiN). [18, 21, 22] (It should be noted that, in this article, we use the abbreviation SiN to denote general silicon nitride with an arbitrary stoichiometry, i.e., SiN_x, as typical SiN films used in the semiconductor industry are neither crystalline nor stoichiometric.) As in selective RIE of SiO_2 over Si,[78] fluorocarbon (FC) radicals are typically used as adsorbent in PE-ALE of SiO_2. Similarly, as in selective RIE of SiN over SiO_2,[79] hydro-fluorocarbon

(HFC) radicals are used in PE-ALE of SiN.

In PE-ALE of SiN, precursor species of the adsorption steps are typically generated from plasma with HFC gases such as CH_3F.[20, 23] The sputtering threshold energy of SiN by Ar^+ ion irradiation is lower than 50 eV. [80–82] However, all PE-ALE experiments of SiN using HFC adsorption and Ar^+ ion irradiation for desorption use ion energy significantly higher than the sputtering threshold energy. Furthermore, even at such high ion energy, unless the ion irradiation time is sufficiently long, an etch-stop occurs during PE-ALE of SiN. For example, in the SiN PE-ALE of Ref. 23, where the typical ion irradiation energy was about 330 eV and the ion irradiation time was 10 s, an etch-stop was observed rather quickly. On the other hand, in the SiN PE-ALE process of Ref. 20, where the typical ion irradiation energy was about 110 eV and the ion irradiation time was 120 s, the PE-ALE cycles proceeded without any etch-stop. To avoid an etch stop in PE-ALE of SiN, either high ion energy or a relatively long Ar^+ ion irradiation time is required. However, if the ion energy is too high or the ion irradiation time (i.e., the desorption step) is too long, the etching is mostly dominated by physical sputtering and, therefore, the self-limiting nature of PE-ALE is lost.

The goal of this study is to clarify the mechanisms of possible etch-stops in PE-ALE of SiN. As mentioned earlier, in a typical two-step PE-ALE process of SiN, an etch-stop may occur if the incident ion energy is low or the ion irradiation time is too short. It contrasts with PE-ALE of Si and, to some extent, that of SiO_2, for which etch-stop is less likely to occur.

For PE-ALE of Si, Cl is typically used in the adsorption step although other halogen species such as fluorine (F) or bromine (B) could also be used. For PE-

ALE of SiO_2, fluorocarbon (FC) precursors are used in the adsorption step. In a very simplistic way, the reason that an etch-stop is less likely to occur in PE-ALE of Si or SiO_2 can be understood in the following manner: In the ideal desorption process where the minimum energy to cause the formation of volatile molecules via surface reactions is provided, all reactive chemical species provided to the surface in the adsorption step should leave the surface by the end of each PE-ALE cycle such that the new cycle can start with a clean material surface. For example, in an ideal PE-ALE process of Si with Cl adsorption, volatile species $SiCl_4$ can be formed in the desorption step via reaction

$$\mathrm{Si} + 4\,\mathrm{Cl} \longrightarrow \mathrm{SiCl_4}$$

In reality, however, many $SiCl_x$ species with $0 \leq x \leq 3$ can also desorb from the surface if ion irradiation is used for the desorption step. Similarly, in a PE-ALE process of SiO_2 with CF_3 adsorption, the surface reaction

$$3\,\mathrm{SiO_2} + 4\,\mathrm{CF_3} \longrightarrow 3\,\mathrm{SiF_4} + 4\,\mathrm{CO} + \mathrm{O_2}$$

can occur and all the reaction products (i.e., all species on the right-hand side) are volatile. As in the case of PE-ALE of Si, in reality, many other species such as SiF_x with $0 \leq x \leq 3$ can also desorb from the surface if ion irradiation is used for the desorption step.

However, in a PE-ALE of SiN with adsorption of CH_2F or CHF_2 radicals (as we shall discuss in this work), if the SiN surface has a stoichiometry of Si_3N_4, possible surface reactions always leave some C atoms on the surface as

$$3\,\mathrm{Si_3N_4} + 12\,\mathrm{CH_2F} \longrightarrow 3\,\mathrm{SiF_4} + 4\,\mathrm{NH_3} + 3\,\mathrm{CH_4} + 9\,\mathrm{C} \tag{3.1}$$

or

$$3\,\mathrm{Si_3N_4} + 12\,\mathrm{CHF_2} \longrightarrow 3\,\mathrm{SiF_4} + 4\,\mathrm{NH_3} + 3\,\mathrm{CF_4} + 9\,\mathrm{C} \tag{3.2}$$

In other words, even under ideal conditions where all chemical reactions could form volatile reaction products such as SiF_4 and NH_3, some C may remain on the surface unless they are sputtered off by incident Ar^+ ions. Such leftover C atoms tend to attract more C atoms in the subsequent HFC adsorption species and then lead to C accumulation over PE-ALE cycles.

In this study, molecular dynamics (MD) simulations are used to analyze the effects of HFC adsorption and Ar^+ irradiation on PE-ALE of SiN. The effects of H-rich (CH_2F) and F-rich (CHF_2) precursor radicals on the etching efficiency are compared. The effects of Ar^+ ion energy and ion irradiation time (i.e., ion dose) on the etching efficiency and self-limiting properties are also examined. In this study, unlike the earlier study of Ref. 83, we mostly focus on the analysis of a single cycle. The etch stop effects observed over a few cycles similar to what was observed experimentally in Ref. 23 are also discussed.

3.2 MD simulation

In this study, classical MD simulations were performed with an in-house code tailored to study ion-surface interactions during plasma processes. This section outlines the simulation methods. As in Ref. 83, a model material of SiN is a β-Si_3N_4 crystal with lattice constants being $a = b = 7.6$ Å and $c = 2.91$ Å with a top surface area of 4.04 x 2.33 nm^2 is used to represent a SiN surface layer. Typical SiN films in semiconductor applications are amorphous and may contain some hydrogen (H). However, in this simulation study, we use a well-defined crystalline SiN as the model material because it is uniquely defined and, therefore, the simulation results can be reproduced easily in later assessments. Furthermore, as we shall see later, ion bombardment causes amorphization and,

therefore, our simulation results based on the crystalline SiN do not differ much from those based on amorphous SiN with a similar density.

Periodic boundary conditions were implemented horizontally to assume an infinitely large surface layer. The initial depth of the model material was set at 2.25 nm and additional Si_3N_4 layers are added to the bottom of the model material to ensure that the model material maintains a sufficient depth as the etching process proceeds. More specifically, if the system's temperature (or average kinetic energy) exceeds a certain threshold value or an injected or recoiled atom passes through the bottom of the model material, the last injection simulation is discarded and a new injection simulation is re-done with the thicker material model. During the MD simulation, the atoms in the bottom layer of the model material are held fixed in position to prevent a downward drift of the system caused by the momentum transfer from incident species.

Figure 3.1 shows a side view of the SiN model material, where each atom is represented by a sphere with a color and a size indicating its atomic species and typical atomic interaction radius, and the depth profiles of the atomic densities. In (b), the vertical axis indicates the depth (or height) measured from the position of the top surface of SiN, taking a negative value if the position is below the top surface of SiN. The atomic density is evaluated as the number of each atomic species per unit volume averaged over a depth interval of 3 Å. The undulating curves for Si and N indicate that the material is crystalline. The horizontal broken lines in (a) indicate the depth positions of (b).

The interatomic force fields and potential functions used in the simulations of this study are reactive-force-field potential functions and the same as those in Ref. 83, which are described in the form similar to those of Stillinger-Weber

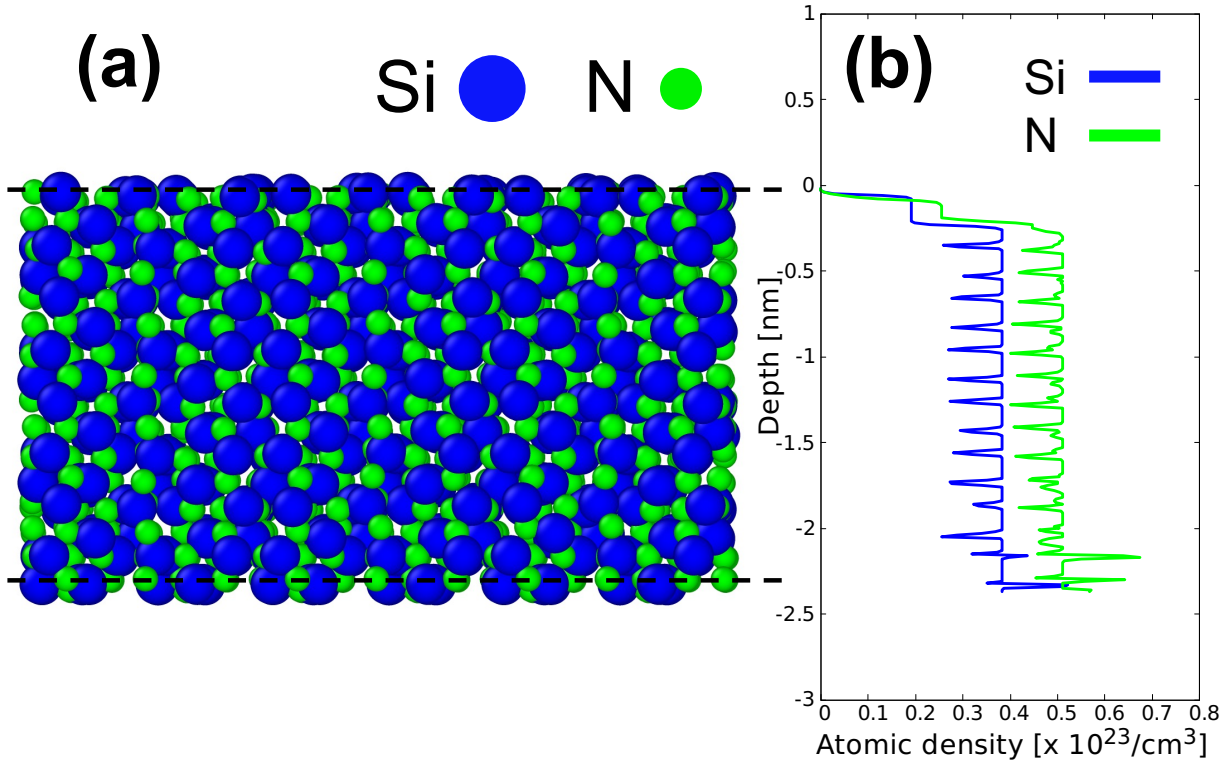

Figure 3.1: (a) Ball-model representation of the initial SiN model material, thermalized at 300 K. The model's initial height is 2.25 nm, but more SiN layers are added from the bottom automatically to maintain a sufficient depth during MD simulation. Blue and green spheres represent Si and N atoms. (b) The corresponding depth profiles of atomic densities of the initial SiN model material.

potential functions[45, 46, 84] with bond orders determined by the number of atoms surrounding oxygen (O), carbon (C), or nitrogen (N) atoms, as in Tersoff and Brenner potentials. [85–88] The ion or radical irradiation is simulated with a series of "injection simulation cycles", as in earlier simulations presented in, e.g., Refs.76, 89–97. The equations of motion are numerically integrated with variable time steps, usually ranging from 0.2 to 0.5 fs, to ensure the conservation of total energy of the system. In this study, all species are injected with a specified incident energy at a normal angle, and hit the surface at random locations. We do not consider the effects of electrical charges of incident ions except for the fact that

incident ions typically have high kinetic energies. In other words, the interatomic interactions among specific species are assumed to be the same whether some of those species are ionized or not. This may be justified if an incident ion is charge-neutralized right before it interacts with surface atoms due to the Auger effects. The angle of incidence is assumed to be normal to the initial top surface for all species in this study.

In each injection simulation cycle of Ar^+ ion irradiation, a single Ar ion is injected from a position slightly above the material surface with a given incident ion energy. In each injection simulation cycle for HFC radical irradiation, a single HFC radical species is injected with a kinetic energy of each radical species being 0.5 eV. The horizontal position of an injected species is selected randomly in each injection simulation cycle. The incident energy of 0.5 eV for a single radical species is higher than their typical thermal energy in plasma but much lower than typical bond energies. The superthermal incident energy speeds up the gas-phase transport of these species without much affecting their interaction with surface atoms.

The duration of each injection simulation cycle corresponds to a physical time of 2 ps. The initial temperature of the surface is set at 300 K. In each injection cycle, the microcanonical ensemble (NVE) simulation, where the total energy of the system is conserved, is employed for the first 700 fs. Subsequently, the system is gradually cooled with the Langevin thermostat[51, 98] for the subsequent 1200 fs and then with the Berendsen thermostat[99, 100] for another 100 fs. The cooling operation is applied to all atoms in the system and brings the system temperature back to the initial temperature of 300 K before the next injection cycle simulation starts.

3.3 Results and discussions

3.3.1 HFC adsorption

PE-ALE processes are simulated with a combination of ion and radical injection cycles. The adsorption step of a SiN PE-ALE process is simulated by depositing a single CH_2F or CHF_2 radical species for each injection cycle until the deposited film thickness reaches about 2 nm, as observed in past experiments. [20, 23] For CH_2F adsorption, it took a radical dose of 1.49×10^{16} cm^{-2}, corresponding to 1,400 injection cycles, to deposit an HFC layer of the desired film thickness. For CHF_2, it took a radical dose of 1.17×10^{16} cm^{-2}, corresponding to 1,100 injection cycles, to achieve the same in our simulations. This is because the sticking probabilities of these radical species and the deposited film densities are slightly different.

Figure 3.2 shows the HFC films deposited on SiN obtained from MD simulations. Here (a) and (b) show the side views of the deposited HFC polymers and the underneath SiN layers, where each atom is represented by a sphere. In (c) and (d), the depth profiles of the atomic densities are plotted, corresponding to the side view images of (a) and (b). In (c), the atomic density of H (indicated by the red curve) is approximately twice as high as those of C and F, verifying the adsorption of the CH_2F radicals on the surface. Similarly, in (d), the atomic density of F is twice as high as those of C and H. It is also seen that the film density (e.g., C density) in (c) is slightly higher than that in (d).

3.3.2 Ar^+ ion irradiation

After the adsorption of HFC radical species, the desorption step with Ar^+ ion irradiation was examined up to an ion dose of 1.86×10^{16} cm^{-2}. The ion dose is

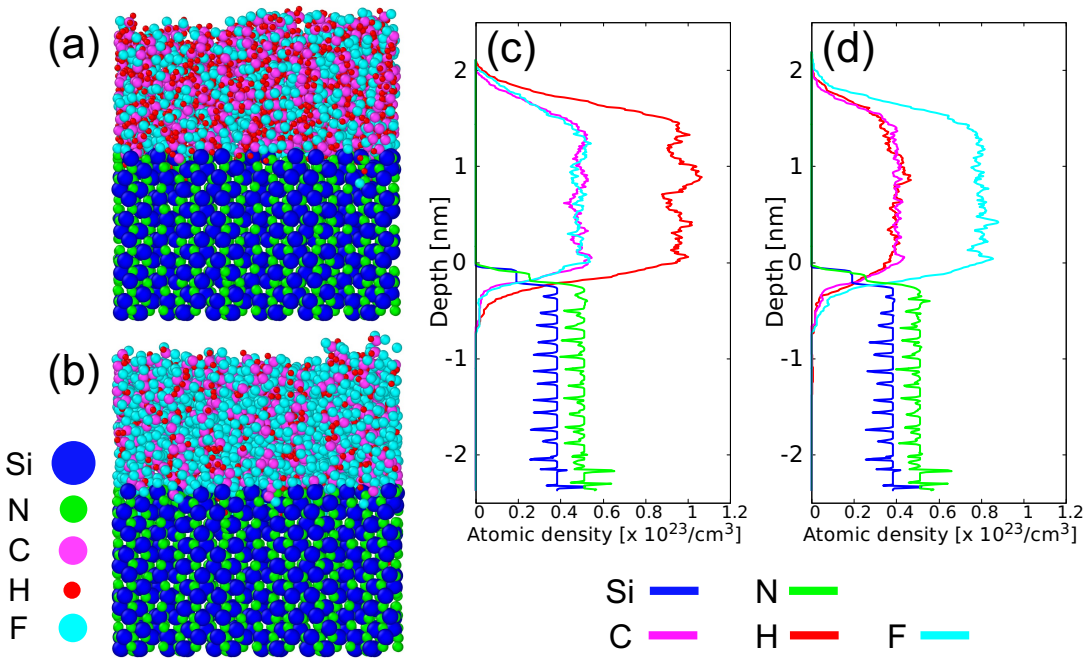

Figure 3.2: Ball-model representations of the surface regions after the adsorption of 2 nm HFC layers with (a) CH_2F and (b) CHF_2 radicals, and the corresponding depth-profiles of atomic densities for (c) CH_2F and (d) CHF_2 adsorbed surfaces. The incident energy of each radical was set at 0.5 eV with radical doses of 1.49 $\times$ 10^{16} cm^{-2} and 1.17 $\times$ 10^{16} cm^{-2} for CH_2F and CHF_2. As in Fig. 3.1, Si and N atoms are represented by blue and green spheres while H, F, and C atoms are represented by red, cyan, and magenta spheres, respectively.

typically proportional to the ion irradiation time. The time-averaged ion flux on the material surface can be given approximately by $\Gamma_i = n_i u_B$ under the assumption that a collisionless sheath is formed. Here n_i is the ion density and $u_B = \sqrt{k_B T_e}/m$ is the Bohm velocity with k_B, T_e, and m being the the Boltzmann constant, electron temperature, and ion mass, respectively. For example, if $T_e = 3$ eV and $n_i = 10^9$ cm^{-3}, the ion dose of 1.86 $\times$ 10^{16} cm^{-2} corresponds to approximately 60 s. [76, 101]

The changes in depth (or surface height) are plotted as functions of the Ar^+ ion dose in Fig. 3.3. The incident ion energies were 50, 150, and 300 eV for (a),

(b), and (c), respectively. The depth of 0 nm corresponds to the position of the initial SiN model material's top surface. (The exact position of the material's top surface is defined as the position where the atomic density of the material is 0.2×10^{23} cm^{-3} in this article.) The curve denoted as "physical sputtering" represents the top surface position when a pristine SiN surface is irradiated by Ar^+ ions. The curves denoted as "with CH_2F" and "with CHF_2 represent those when the CH_2F and CHF_2 adsorbed surfaces are irradiated by Ar^+ ions.

Here three distinct slopes are observed for CH_2F and CHF_2 adsorbed surface heights. The initial steep slope, denoted by I, indicates the fast etching process of the deposited HFC polymer layer. The following less-steep slope, denoted by II, indicates the etching of the SiN surface mixed with HFC atoms, where chemical reactions of HFC atoms with Si and N contributed to the etching process. The final and least steep slope, denoted by III, indicates the physical sputtering of SiN after HFC atoms were nearly exhausted from the surface. The slope III is similar to the slope for pristine SiN being physically sputtered, as seen in (b) and (c). It should be noted that some knocked-on HFC polymer atoms might have remained near the surface region even during the physical sputtering phase of slope III, as will be discussed later.

In (a), it is seen that the slope I for the CH_2F layer is steeper than that for the CHF_2 layer although the CH_2F layer of this study is denser than the CHF_2 layer. It suggests that the presence of more abundant H atoms contributed to the efficient removal of C. In (b) and (c), although the slopes for CH_2F and CHF_2 layer etching were nearly the same, the transition from slope I to slope II occurred at a slightly larger film thickness in the case of CHF_2 than CH_2F. (In phase II, the curve for CHF_2 was slightly above the curve for CH_2F.) It indicates a change

in the chemical composition of the etched material occurred slightly earlier in the case of CHF_2 than CH_2F. This is likely to be caused by incident Ar^+ ion impact initiating chemical reactions of Si with F near the HFC and SiN boundary earlier in the presence of more abundant F atoms. Because the etch rate (i.e., etched depth per unit ion dose or unit time) is higher for slope II than slope III, the surface chemical reactions between the SiN surface with adsorbed atomic species enhanced the etching of SiN.

Figure 3.4 shows the ratio of the number of Si- or N-containing desorbed species to the number of all Si- or N- containing desorbed species, accumulated over the phases of slopes I and II, i.e., from the start of Ar^+ ion irradiation to an ion dose of 9.04 x 10^{15}cm^{-2}. Desorbed species from the CH_2F and CHF_2 adsorbed surfaces are plotted, as indicated. The ion energy was 150 eV, corresponding to Fig. 3.3(b). It is seen that, besides mono or diatomic ejection of Si and SiN species, Si atoms were most likely removed as fluorides, i.e., SiF_x ($0 \leq x \leq 3$) species. The excess H atoms in the CH_2F adsorption layer seem to have contributed to the removal of N atoms by forming HCN and NH. It is seen that most species desorbed as fragments of molecules and, therefore, the chemical reactions given in Eqs. (3.1) and (3.2) were not the main surface reactions. Nevertheless, some C atoms may remain on the surface at the end of phase II, as chemical reactions of Eqs. (3.1) and (3.2) suggest qualitatively.

Figure 3.5 shows the total number of Si and N atoms removed from the surface over the duration of Ar^+ irradiation up to the ion dose specified on the horizontal axis. Other removed species such as C and F are not listed. The Si and N atoms desorbed in any forms such as monoatomic Si or fluorides SiF_x are counted in Fig. 3.5. It is seen in all cases that N atoms are preferentially removed than Si

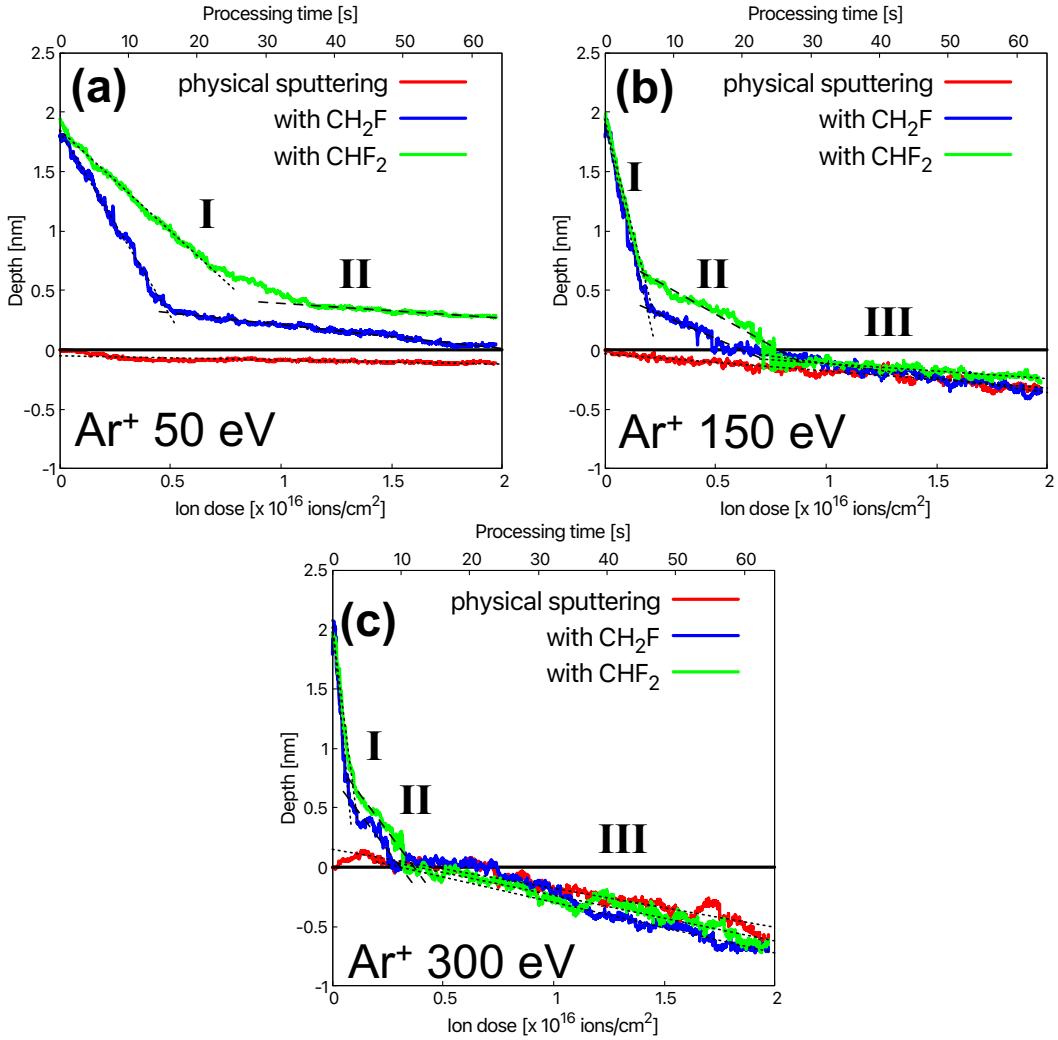

Figure 3.3: Changes in surface height as functions of the Ar^+ ion dose at incident energies of (a) 50 eV, (b) 150 eV, and (c) 300 eV. The upper horizontal axis indicates the process time when the ion current density is 0.05 mA/cm^2. The curves are for the pristine SiN, denoted as "physical sputtering," as well as the CH_2F and CHF_2 adsorbed surfaces, as indicated therein. The broken and dotted lines are guides to the eye for their overlapping curves.

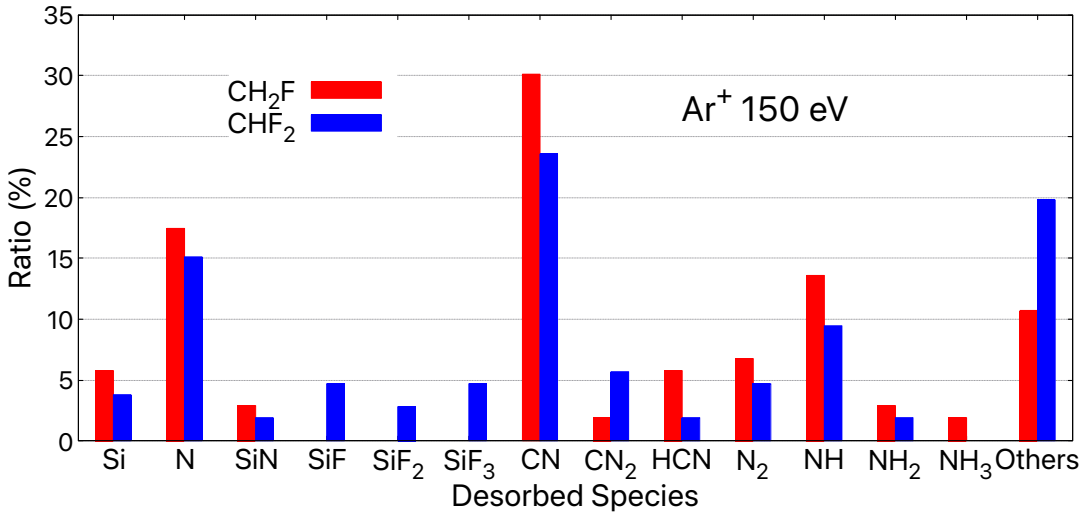

Figure 3.4: Ratios of the number of Si- or N-containing desorbed species to the total number of all Si- or N-containing desorbed species from CH_2F and CHF_2 adsorbed surfaces during 150 eV Ar^+ ions irradiation up to an ion dose of 9.04 $\times$ 10^{15} cm^{-2}, i.e., phases I and II of Fig. 3.3(b). The 'Others' category is the sum of the corresponding (typically small) ratios for all other Si- or N- containing desorbed species.

atoms, especially at an early stage; in steady state, the number ratio of removed Si and N atoms should be 3:4, based on the stoichiometry of the SiN model material of this study. Thus physical sputtering tends to form a Si-rich layer at the top of the SiN film. It is also seen in (a) that the physical sputtering yield by 50 eV Ar^+ ions is extremely small (< 0.004). In other words, the physical sputtering threshold energy of the SiN model material by Ar^+ ion irradiation is about 50 eV. Here the sputtering yield is defined as the number of specific atoms (e.g., Si) removed from the surface per ion impact. It should be noted that the slope value of the N or Si curve in Fig. 3.5 represents the sputtering yield for N or Si atoms.

In the cases of physical sputtering in (a), (d), and (g), the slope of the curve changes slightly as the ion dose increases. This indicates the amorphization of the material surface caused by the ion bombardment at an early stage and the

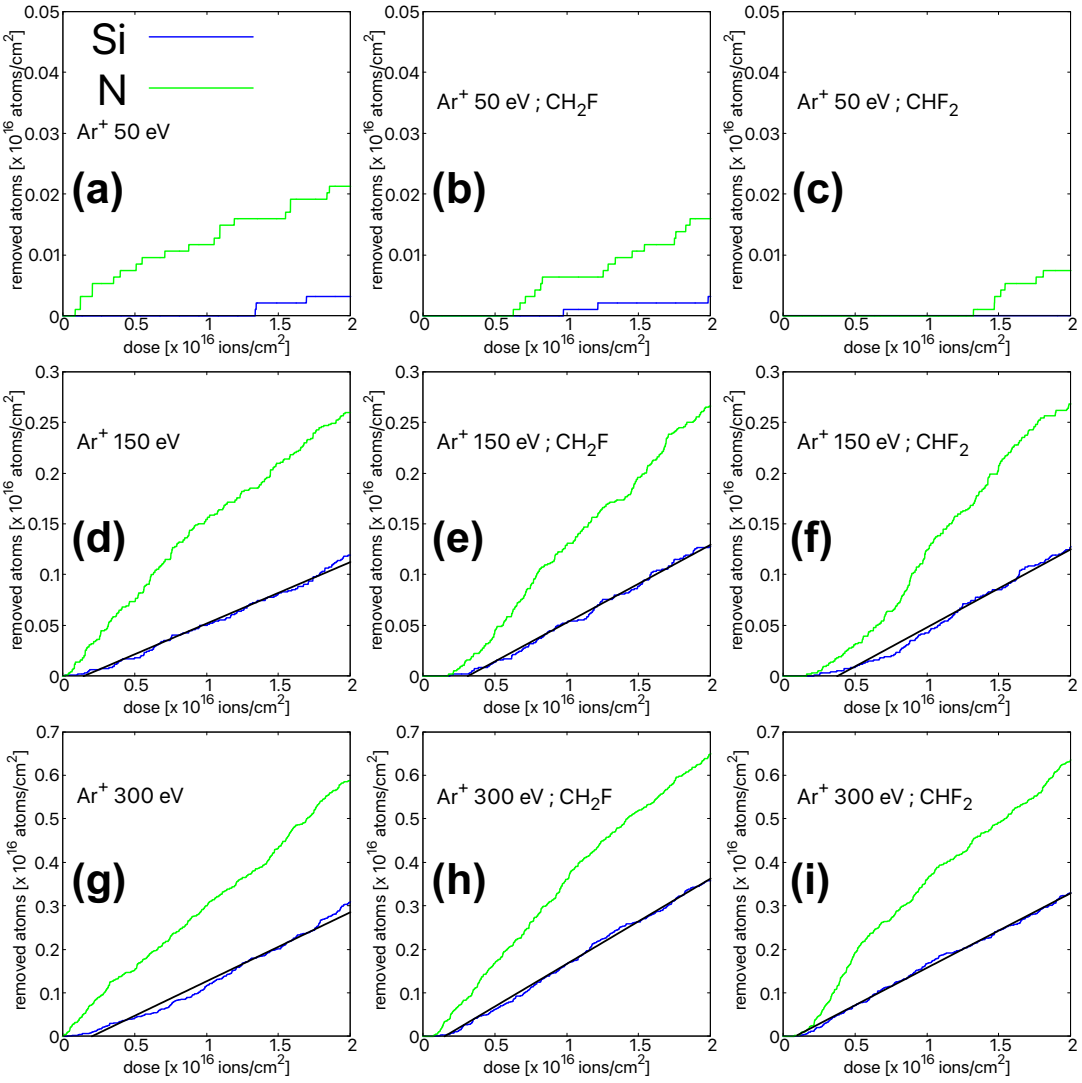

Figure 3.5: Numbers of removed Si and N atoms from (a), (d), (g) pristine, (b), (e), (h) CH_2F adsorbed, and (c), (f), (i) CHF_2 adsorbed SiN surfaces per unit area as functions of the Ar^+ ion dose. The incident ion energies are (a)-(c) 50 eV, (d)-(e) 150 eV, and (g)-(i) 300 eV. The blue and green curves are for Si and N atoms. The black lines in (d)-(i) fit the Si curves as guides to the eye.

consequent changes in the sputtering yields. In the cases of HFC-adsorbed surfaces, there are incubation periods for the removal of N and Si atoms; e.g., the removal of N atoms initiated after an ion dose of approximately 0.5×10^{16} ions cm^{-2} in (b) and around 1.25×10^{16} ions·cm^{-2} in (c). These ion doses are required for Ar^+ ions to remove the HFC layers and to form mixed SiN layers with HFC atoms.

At 150 eV, as shown in (d), (e), and (f), the slopes of the Si curves are similar, indicating the chemical reactions did not much enhance the sputtering yields of Si atoms. At 300 eV, however, as seen in (g), (h), and (i), the slopes of the Si curves of (h) and (i) are slightly larger than that of (g), indicating that chemical reactions due to the presence of HFC atoms increased the removal rate of Si atoms from the surface. (The slope values of the Si curves, fit by the solid lines, in (g), (h), and (i), are 0.159, 0.196, and 0.172, respectively, representing the Si sputtering yields.) For the ALE application, we take advantage of these etching conditions where chemically enhanced etching is observed. However, it should be noted that the ion energy of 300 eV is much higher than the physical sputtering threshold energy of about 50 eV. Therefore, no well-defined self-limiting etching can be expected for the SiN ALE with such Ar^+ ion irradiation conditions.

Figure 3.6 shows the ratio of the number of Si- or N-containing desorbed species to the total number of all Si- or N-containing desorbed species, accumulated over an ion dose of 1.86 x 10^{16} cm^{-2}. In (a), the surfaces was the CH_2F adsorbed surface and, in (b), the CHF_2 adsorbed surface. The ion energies were 50, 150, and 300 eV, as indicated in the figure.

It is seen that the ratios of monoatomic Si and N and diatomic SiN increase as the ion energy increases, indicating these species were ejected from the surface by physical sputtering. Other species involve some chemical reactions and their

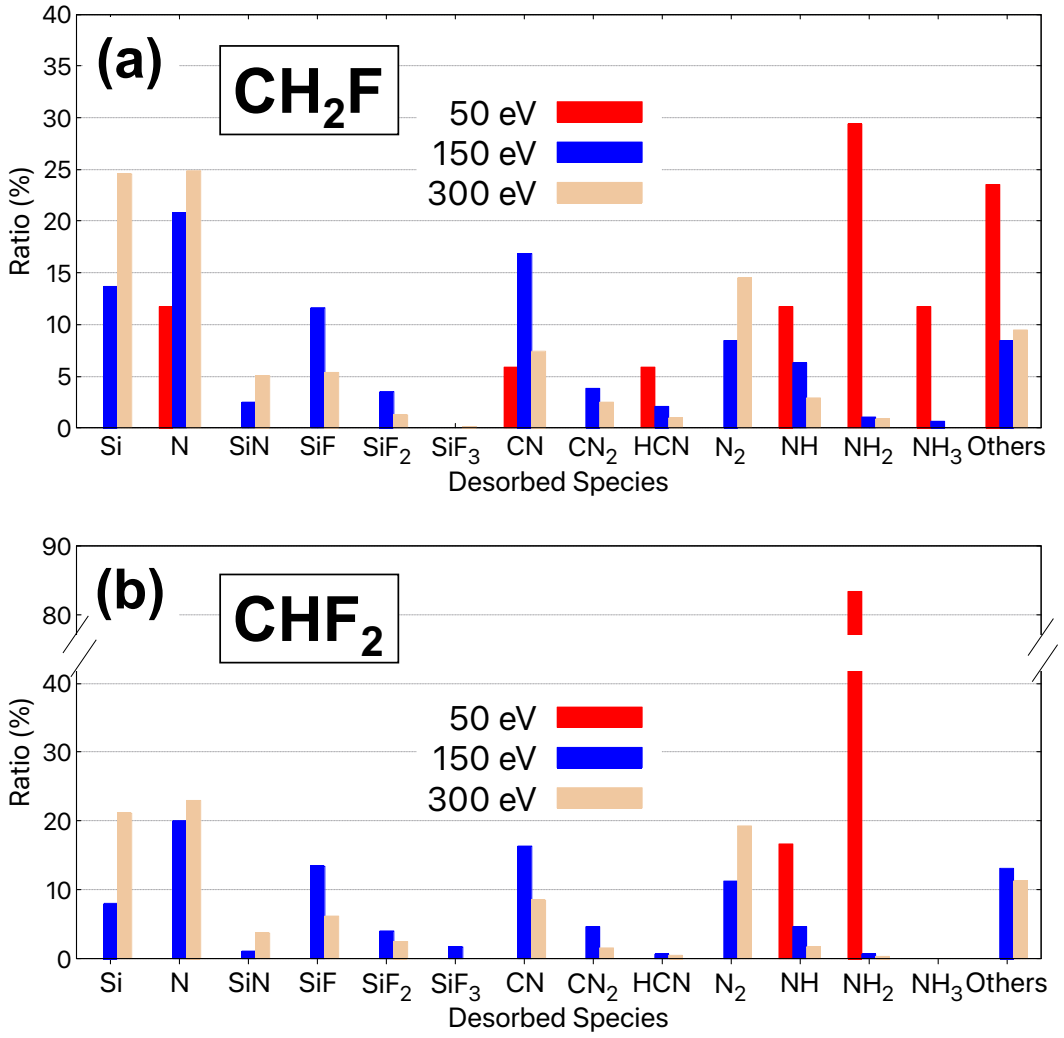

Figure 3.6: Ratios of the number of Si- or N-containing desorbed species to the total number of all Si- or N-containing desorbed species from (a) CH_2F and (b) CHF_2 adsorbed surfaces during Ar^+ ions irradiation up to an ion dose of 1.86 x 10^{16} cm^{-2}, corresponding to the total ion dose of Fig. 3.3, at different ion energies. The 'Others' category is the sum of the corresponding (typically small) ratios for all other Si- or N- containing desorbed species.

ratios typically decrease with increasing ion energy. The fact that large portions of Si and N desorbed species are such reacted species indicates that the chemical modification of the surface through the adsorption of the HFC layer effectively aids the etching of SiN. It is also seen that N atoms are removed through interactions with C and H atoms, resulting in the formation of CN and HCN species. F atoms, which are known etchants for Si, also contribute to the removal process by generating SiF_x species. These observations demonstrate the significance of the HFC layer adsorption in selectively assisting the etching process.

3.3.3 Depth profiles

Figure 3.7 shows the depth profiles of atomic densities at the end of period III, i.e., at an Ar^+ ion dose of 1.86×10^{16} cm^{-2}. As in Fig. 3.1, the origin of the depth corresponds to the initial top surface of the SiN model material. At 50 eV, it is seen in (a) and (b) that thick layers of C, F, and H remained near the surface. As a result, 50 eV Ar^+ ions hardly penetrated the HFC layers, causing the low Si and N removal observed in Fig. 3.5. At 150 eV, some etching of the SiN material occurred. C, F, and H atoms were pushed more deeply toward the bulk through knock-on collisions caused by incident Ar^+ ions. At 300 eV, the preferential removal of N atoms over Si atoms is evident and the densities of remnants of HFC atoms are much lower but more deeply penetrated the bulk of the materials. The undulating profiles of Si and N on the deeper side indicate that the SiN material is crystalline, as in its initial state. The smoother profiles near the top surface indicate that the material is amorphized there by ion bombardment.

Figure 3.8 presents the depth profiles of covalent bond densities except for the Si-N bonds at the end of period III, i.e., at an Ar^+ ion dose of 1.86×10^{16} cm^{-2},

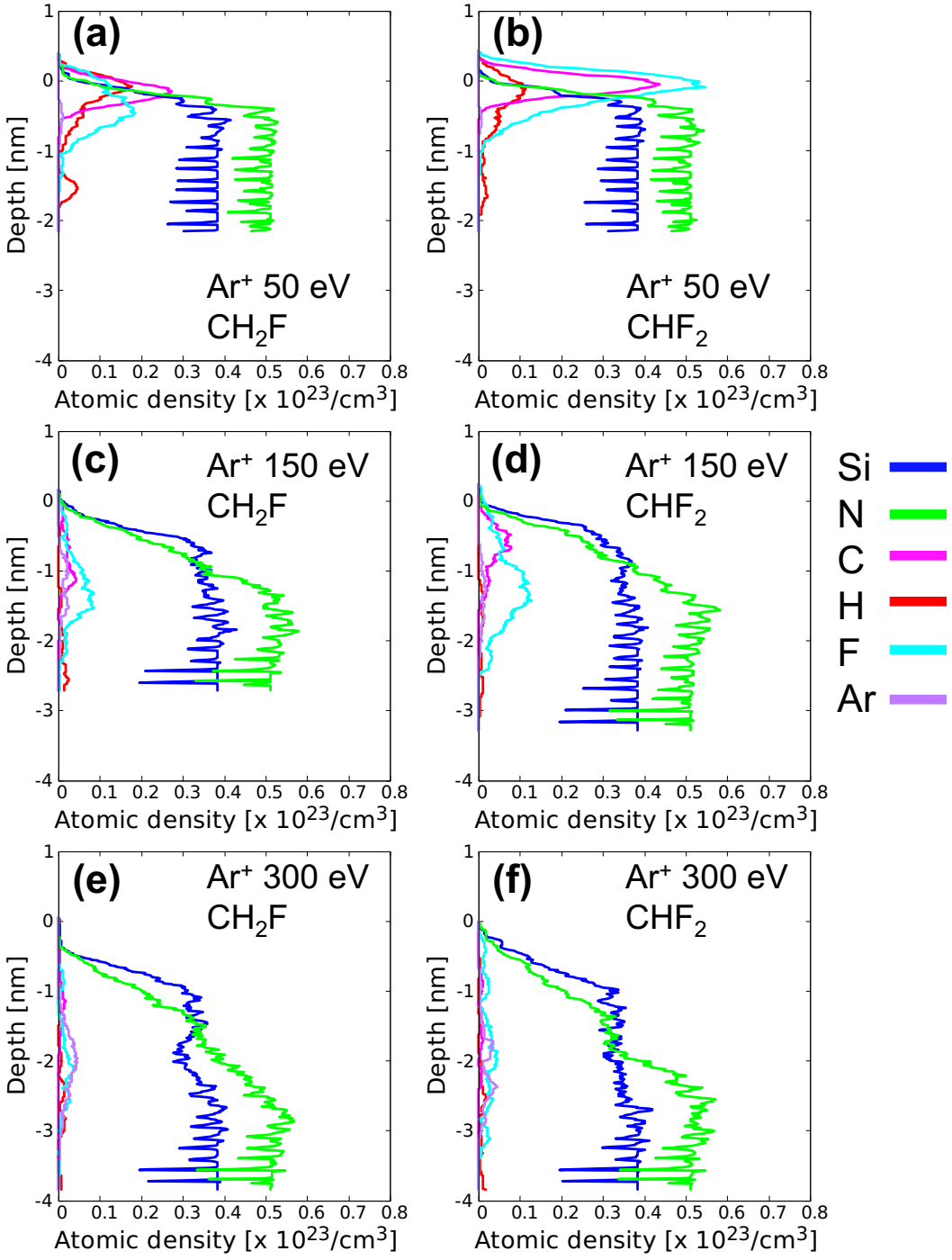

Figure 3.7: Depth profiles of atomic densities for (a),(c), (e) CH_2F and (b), (d), (f) CHF_2 adsorbed surfaces after Ar^+ ion irradiation of 1.86 $\times$ 10^{16} cm^{-2}. The incident ion energies are (a), (b) 50 eV, (c),(d) 150 eV, and (e), (f) 300 eV. The density curve for Si is blue, N green, C magenta, H red, and F cyan.

corresponding to Fig. 3.7. Our interest here is in the newly formed bonds during the Ar^+ ion irradiation process, so the Si-N bond density, which is much larger than the newly formed bonds shown here, is not plotted in Fig. 3.8. The densities of dominant newly formed bonds are shown by colored curves with labels of the corresponding colors. All other bond densities are depicted in gray, indicating that they are much lower than the labeled bond densities.

In (a), although the HFC layer was largely removed, some remaining bonds of C-C, C-H, C-N, and Si-C are observed near the top surface. In (b), thick and dominant layers of C-F and C-C bonds are seen whereas C-N, C-H, Si-F, and N-H bonds were also formed. Due to the high F density and a higher bond dissociation energy of C-F (5.33 eV) compared to C-H (3.46 eV), C atoms are more likely to bond with F atoms than H atoms.

As seen in (c) and (d), at 150 eV, the HFC layer was mostly removed, but some HFC atoms remained by forming Si-C, C-N, and Si-F bonds. The high density of Si-Si bonds signifies the preferential removal of N atoms near the top layer. The observed C-N bonds are consistent with previous observations, [23] as well as the presence of Si-C bonds. [27, 102] At 300 eV, the C-C and Si-C bonds are hardly seen because the extensive physical sputtering mostly removed C atoms, as seen in (e) and (f) of Fig. 3.7.

3.3.4 Multi-cycle analysis of SiN ALE

From Fig. 3.3, it is clear that, for the PE-ALE of SiN with Ar^+ ion irradiation to be feasible, the ion energy must be much higher than the sputtering threshold energy. Therefore, multi-cycle simulations of SiN ALE were performed with 300 eV Ar^+ ion irradiation. This selection of the ion energy is also consistent with earlier

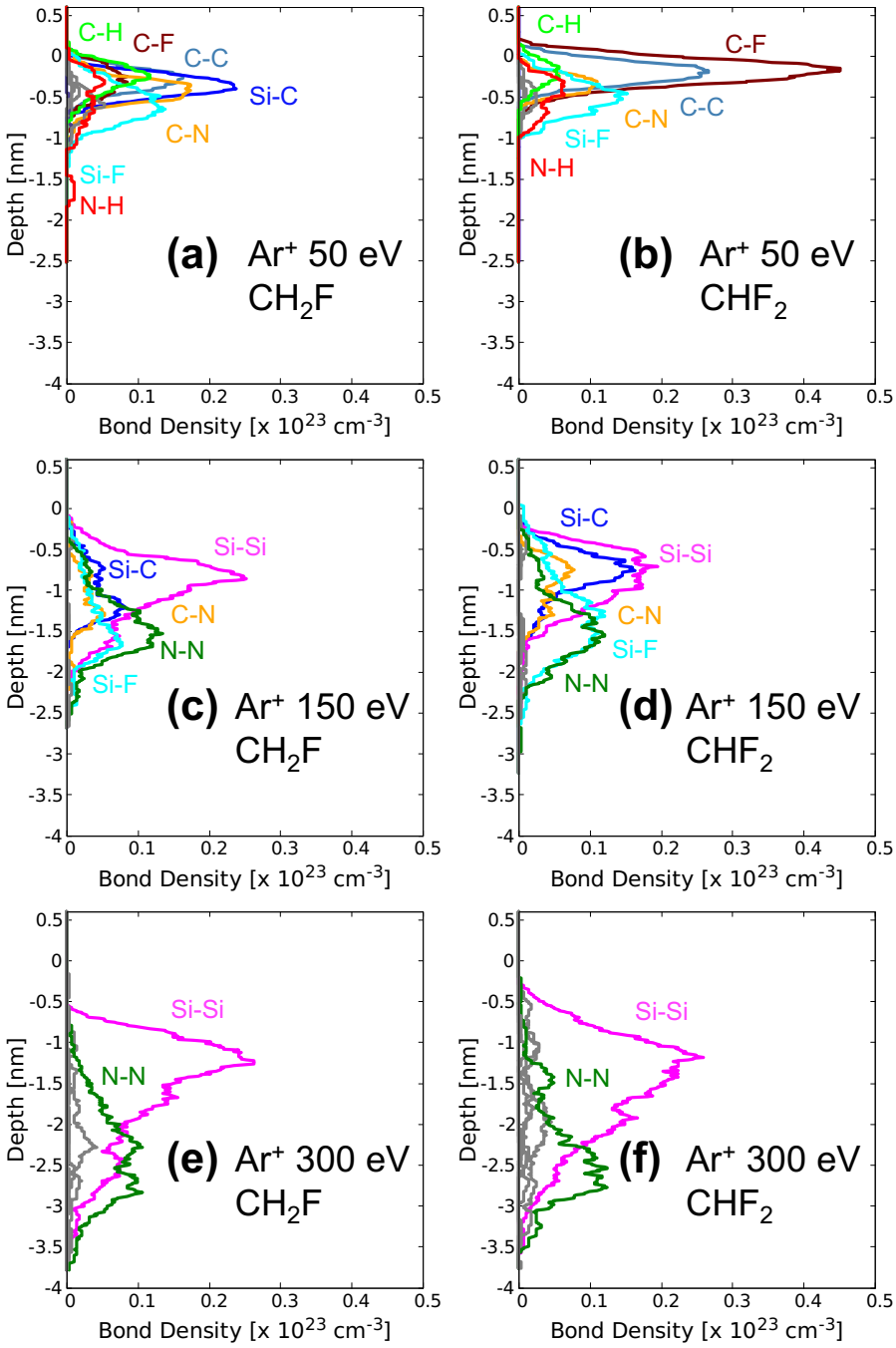

Figure 3.8: Depth profiles of dominant bond densities (except for the most dominant Si-N bonds) for (a),(c), (e) CH_2F and (b), (d), (f) CHF_2 adsorbed surfaces after Ar^+ ion irradiation of 1.86×10^{16} cm^{-2}. The incident ion energies are (a), (b) 50 eV, (c),(d) 150 eV, and (e), (f) 300 eV. The label is for the curve of the same color. All other bond densities are depicted in gray, indicating that they are much lower than the labeled bond densities.

experimental studies of Refs. 23, 75 and 35 and simulation studies of Refs. 83 and 77. The total ion dose for the desorption step was set at 3.19×10^{15} cm^{-2}, i.e., the same ion dose as the one at the end of slope II of Fig. 3.3(c), to minimize the effects of physical sputtering of SiN by Ar^+ ion bombardment. It should be noted that the Ar^+ ion dose in each desorption step here is much lower than that used in the cases of Fig. 3.7.

The change in surface height during the four SiN PE-ALE cycles is shown in Fig. 3.9. As in the earlier figures, the position of the initial SiN model material's top surface is the origin of the vertical axis. The horizontal axis is proportional to time if the CH_2F or CHF_2 radical flux and Ar^+ ion flux are constant in time. The adsorption and desorption steps of the first cycle are labeled with ① and ② delineated with vertical lines. Similarly, in each cycle, the surface height increases during the adsorption step and decreases during the desorption step. Figure 3.5 shows that some Si and N atoms were removed from the surface by the end of the 1st cycle (with an ion dose of 3.19×10^{15} cm^{-2}), so some etching of SiN took place. However, from the second cycle on, the surface height at the end of each cycle continued to increase or at least mostly stayed above 0, indicating that the HFC layer accumulated on the surface and SiN etching may eventually stop completely.

Figure 3.10 shows the depth profiles of atomic densities at the end of the 4th PE-ALE cycle of Fig. 3.9. It is observed in both (a) and (b) that relatively thick HFC layers, mostly consisting of C and F atoms, remained on the SiN surface even after bombardment by Ar^+ ions irradiation. It is also seen that the resulting surface became Si-rich, indicating preferential removal of N atoms from the surface. As seen in Fig. 3.8, the higher densities of Si and C atoms induce further deposition of C atoms by forming Si-C and C-C bonds. As observed in the earlier study of

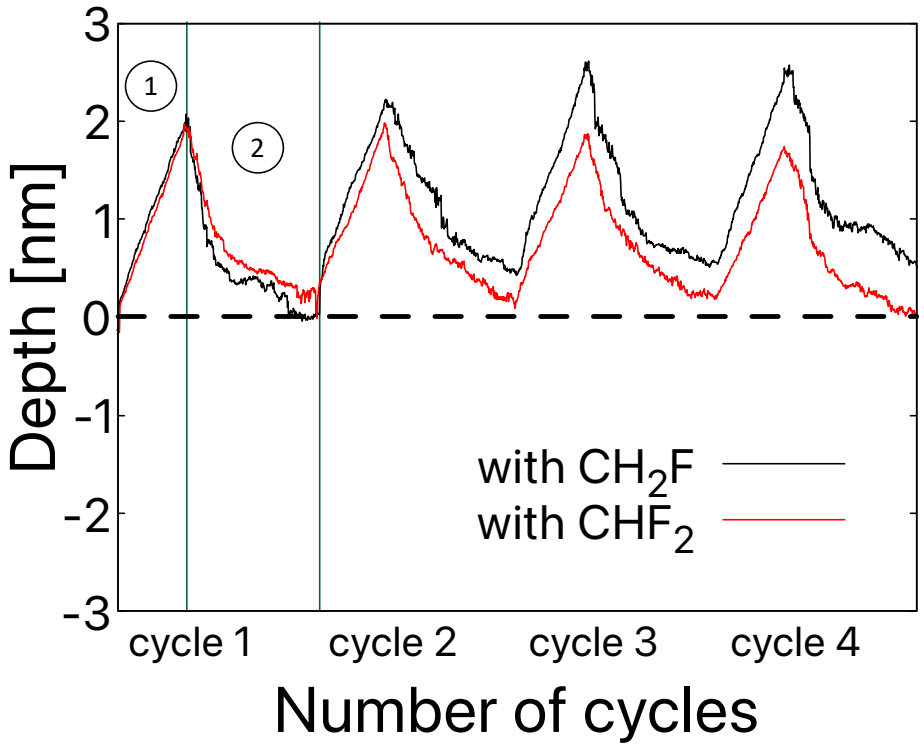

Figure 3.9: Changes in surface height for HFC adsorption and Ar^+ ion irradiation over four PE-ALE cycles. Each PE-ALE cycle consists of the adsorption step (denoted by ①), desorption step (denoted by ②). The incident ion energy is 300 eV and the ion dose in each desorption step is 3.19×10^{15} cm^{-2}, corresponding to phases I and II of Fig. 3.3(c).

Ref. 83, a similar SiN ALE process with a longer sputtering period or an additional oxygen (O) irradiation step can avoid an etch stop.

Figure 3.11 shows the depth profiles of bond densities at the end of the 1st and 4th PE-ALE cycles of Fig.3.9. As in Fig.3.8, no Si-N bond density is shown here and the other dominant bonds are shown by colored curves with the labels of the same colors. All other bond densities are depicted in gray, indicating that they are much lower than the labeled bond densities.

It is seen that the C-C, Si-C, and other C bond densities increased from the first

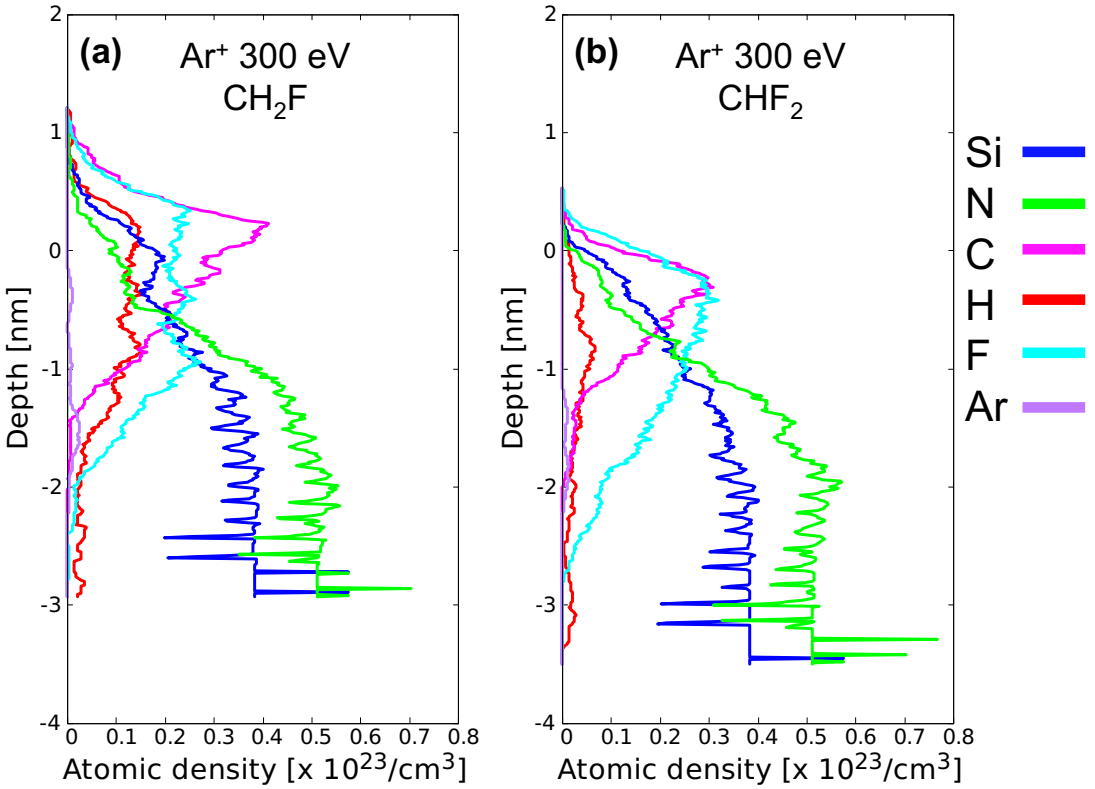

Figure 3.10: Depth profiles of atomic densities for (a) CH_2F and (b) CHF_2 adsorbed surfaces at the end of the 4th SiN PE-ALE cycle of Fig. 3.9. The density curve for Si is blue, N green, C magenta, H red, F cyan, and Ar purple. It should be noted that the Ar^+ ion dose in each desorption step here is 3.19×10^{15} cm^{-2}, much lower than that in the cases of Fig. 3.7.

cycle to the 4th cycle, indicating that, in each cycle, more C atoms accumulated by forming those bonds. Therefore, although the surface position may not seem to have increased much over the first 4 cycles (especially in the case of CHF_2 adsorption) in Fig. 3.9, it is likely that the surface eventually accumulates sufficient C atoms and the etching of SiN completely stops.

After the 4th cycle, the Si-C density is higher in the case of CH_2F adsorption than CHF_2 adsorption, which is consistent with the fact that the C density is higher in the case of CH_2F adsorption than CHF_2 adsorption, as seen in Fig. 3.10.

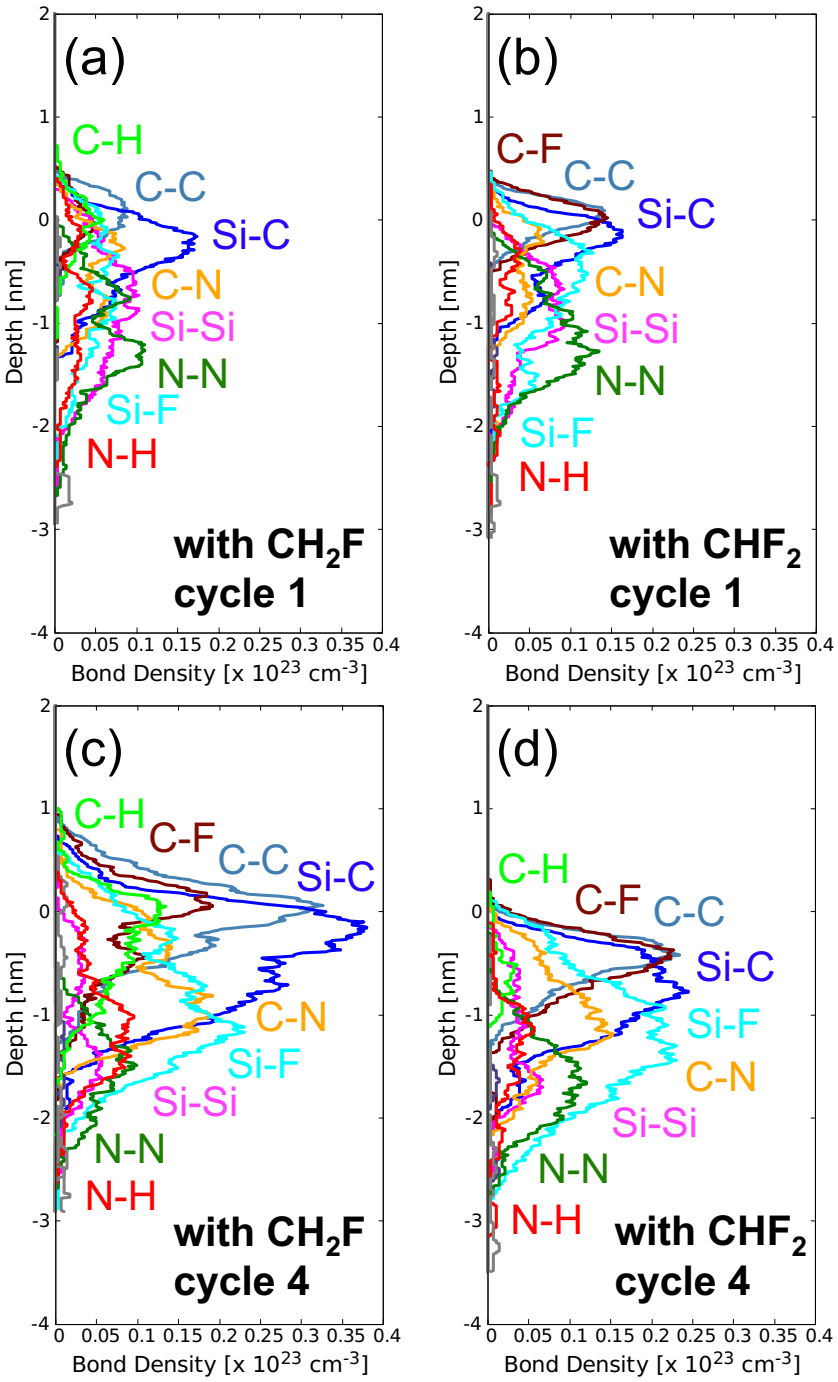

Figure 3.11: Depth profiles of dominant bond densities (except for the most dominant Si-N bonds) for (a),(c) CH_2F and (b), (d) CHF_2 adsorbed surfaces at the end of the 1st and 4th SiN PE-ALE cycle of Fig. 3.9. The label is for the curve of the same color. All other bond densities are depicted in gray, indicating that they are much lower than the labeled bond densities.

However, this is likely because the dose of CH_2F in each adsorption step (1.49 $\times$ 10^{16} cm^{-2}) is slightly higher than that of CHF_2 (1.17 $\times$ 10^{16} cm^{-2}) in each adsorption step, as mentioned earlier.

3.4 Conclusions

Classical MD simulations were employed to clarify the etch-stop mechanism of the SiN PE-ALE process observed in the earlier experiments[23], where each ALE cycle consisted of the HFC adsorption step and Ar^+ ion irradiation step. The influence of the amount of H or F in the adsorbed HFC layer was examined with CH_2F and CHF_2 as representative HFC precursor radicals.

The simulation results revealed that, in the Ar^+ ion irradiation step, there were three distinct phases; in phase I, the accumulated HFC layer was etched away and a mixed layer of the HFC atoms and SiN was formed at the interface of the HFC layer and SiN; in phase II, chemically enhanced etching of SiN took place as the etching proceeded through the mixed layer; and in phase III, HFC atoms were nearly or completely exhausted and the SiN surface was etched by physical sputtering. The analysis of desorbed species showed that C and H atoms of the adsorbed HFC layer interacted with N atoms of the SiN surface, leading to the desorption of CN, HCN, NH, NH_2, etc., while F acted as the primary etchant for Si, resulting in the desorption of SiF, SiF_2, etc. The atomic density depth profiles showed that some C, F, and H atoms remained in the material, with H atoms penetrating deeply into the material by knock-on collisions. At higher incident ion energy, preferential sputtering of N atoms was evident; the surface of SiN became Si rich. The analysis of the bond density distributions showed that the accumulated C atoms were mostly bonded with Si atoms. Such excess C atoms

promoted further accumulation of C atoms in the subsequent cycles, leading to an etch stop. If the ion energy is sufficiently high or the physical sputtering phase III is sufficiently long, more C atoms may be sputtered away from the surface but PE-ALE with such extensive Ar^+ ion sputtering has little self-limiting properties. Therefore, for achieving a stable etch per cycle in PE-ALE of SiN with appreciable ("quasi-") self-limiting properties, the efficient removal of excess C atoms on the surface is crucial for a SiN PE-ALE process to be stable. One way to remove C atoms efficiently from the surface is to introduce a short oxygen irradiation step discussed in the earlier studies of Refs. 35 and 83.

Chapter 4

Surface chemical reactions of etch stop prevention in PE-ALE of SiN

4.1 Introduction

Atomic layer etching (ALE) has garnered significant attention in the semiconductor industry as a highly precise method for removing thin layers of material. Unlike conventional reactive ion etching (RIE) [54, 56, 59, 68] , where etching takes place continuously, ALE is a cyclic process, and a thin layer of the surface material is removed or etched in each cycle [1–4, 73] . In a typical ALE, each cycle consists of two steps or half-cycles. In the first step or half-cycle, a thin top layer of the material is modified by exposure to gaseous species. The first step typically involves the adsorption of gaseous species and therefore is often called an "adsorption step." In the second step or half-cycle, the modified surface layer is removed by desorption. The second step is, therefore often called the "desorption step". In some ALE processes, surface modification also takes place during the desorption step. Some ALE processes have additional steps in

their single cycle. If plasma is used in an ALE process, it is called plasma-enhanced ALE (PE-ALE).

In a stable ALE process, the etched depth in a single cycle is nearly constant over many cycles, so the total etched depth can be precisely controlled by the total number of ALE cycles. The etched depth in a single ALE cycle is often called an etch-per-cycle (EPC). In an ideal ALE, the EPC is constant regardless of the processing time that a single cycle takes. In other words, the etched depth does not increase with the cycle time, or more specifically, the time for the desorption step, once a certain etched depth is achieved. Such a step is called a "self-limit" process.

In typical ALE processes for semiconductor applications, the EPC is much larger than the thickness of a single atomic layer of the material, unlike what the process name suggests. It is often intentional because a larger EPC increases the production yield of semiconductor manufacturing, requiring a fewer number of cycles for a given total etched depth.

For semiconductor applications, a PE-ALE process of silicon (Si) surface was first introduced by Horiike et al. in 1990, where halogen adsorption was used in the adsorption step and Ar plasma irradiation was used in the desorption step [5, 24] . Later chlorine (Cl)-based PE-ALE processes were extensively studied [6, 7, 9, 74] . Similar techniques were also extended to PE-ALE of silicon dioxide(SiO_2) [8, 10–15, 33] and silicon nitride (SiN) [16–23, 75]. . As the technology continues to advance, control of etch selectivity and damages to the final product [1–3, 14, 70, 72, 103] has become crucial issues in the development of ALE processes.

The present study concerns PE-ALE of SiN. Recent studies by Hirata et al. have shown that PE-ALE of SiN consisting of a hydrofluorocarbon (HFC) radical

adsorption step and an Ar plasma irradiation step eventually stops after multiple cycles [23, 75] . This phenomenon occurs due to the accumulation of HFC on the etched surface, which is caused by the remaining carbon (C) atoms from the previous PE-ALE cycles that enhance HFC deposition during the subsequent adsorption steps. The presence of such an HFC layer hinders the ion impact and subsequent removal of the modified surface layer by energetic Ar ions, ultimately leading to an etch stop.

Similar C accumulation phenomena were observed for ALE of SiO_2 [12, 32–34] and an additional oxygen irradiation step was found to mitigate the etch stop [13] . Hirata et al. also stabilized the SiN PE-ALE process by introducing an additional O_2 plasma irradiation step (i.e., oxidation step) and suppressing the etch-stop [23, 35].

The goal of this study is to understand the surface reaction mechanisms of the additional O_2 plasma irradiation step in PE-ALE of SiN, using a theoretical model of the ALE processes. More specifically, we are interested in knowing how effective the O_2 plasma irradiation step can be in removing C atoms and how much it ends up oxidizing SiN to avoid an etch stop. For this purpose, we use molecular dynamics (MD) simulation to evaluate atomic motions during PE-ALE processes of SiN. A better understanding of PE-ALE surface reactions at the atomic level can facilitate the optimization of the current PE-ALE processes as well as the development of ALE processes of new materials.

The rest of this article is organized in the following manner. Section II outlines the MD simulation method used in this study. Section III presents the simulation results and a discussion of the results. Conclusions are given in the final section.

4.2 MD simulation

To investigate the effects of additional O_2 plasma irradiation steps on the performance of SiN PE-ALE processes, we use MD simulations. As shown in Fig. 4.1, our SiN model material consists of a rectangular structure representing a Si_3N_4 slab with dimensions of 4.035 nm $\times$ 2.33 nm $\times$ 2.25 nm. Here Si atoms are shown as beige spheres and nitrogen (N) atoms as blue spheres. Periodic boundary conditions are applied in the horizontal directions to mimic an infinitely large surface. Although the depth or height in the z-direction is typically set at 2.25 nm initially, it can be extended to a larger depth if a deeper material model is needed for our simulation. For example, injected or recoiled atoms reach or pass the bottom layer or an incident ion increases the temperature of the model material too much, the simulation of this particular ion injection event is discarded and additional layers of SiN atoms are added to the bottom of the model material. The positions of atoms in the bottom layer of the model material are held fixed during the simulations to prevent a downward drift of the material model due to the momentum transfer from the incident ions.

In this study, all species are injected at a specified incident energy and the angle of incidence is normal to the initial top surface. The injected species hit the surface at random positions. To simplify the simulations, all the species, including ions, are assumed to be charge neutral in terms of interatomic interactions, and no direct Coulomb interaction is taken into account. In other words, incident ions are treated as the corresponding charge-neutral atoms with the same kinetic energies. This may be justified if an incident ion is charge-neutralized right before it interacts with surface atoms due to the Auger effects.

In the simulations, we first prepare the model material by allowing their atoms

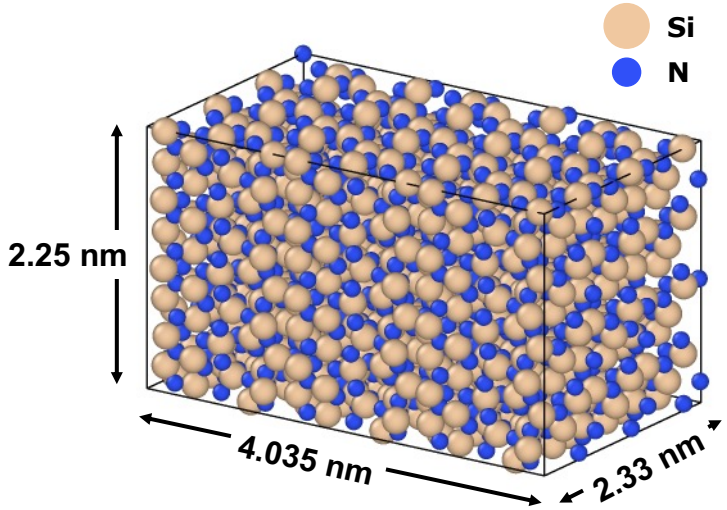

Figure 4.1: The initial structure of the SiN model system used in this study, thermalized at 300 K. The initial height of this material model is typically 2.25 nm but can be extended to a sufficiently large value automatically during the simulation to account for the interaction of incident gaseous species such as radicals and energetic ions with atoms of the material properly. The beige and blue spheres represent Si and N atoms.

to relax at 300 K. The motion of each atom was determined from the solutions of Newton's equations of motion with interatomic force field obtained from modified Stillinger-Weber-type potential functions [45, 46, 104] . For more technical details of the simulations and comparisons with experimental results, the reader is referred to References 35, 84, 91–94, 96, 97, 105.

The simulation of gas or plasma interaction with a material surface consists of a series of gaseous-species (e.g., ion or radical) injection cycles. In each gaseous-species injection cycle, single or multiple gaseous species are injected into the surface. The duration of each injection cycle is 2 ps. During this period, MD simulation is performed under the microcanonical ensemble (i.e., NVE) conditions for the first 700 fs, where the total energy of the system is conserved. Then the

system is cooled for 1,300 fs such that the temperature of the model material is brought back to the initial temperature of 300 K gradually. The cooling is first performed with the Langevin thermostat [51, 98] for 1,200 fs and then the Berendsen thermostat for the final 100 fs [99, 100].

In our simulation, we deposit CH_2F radicals as representative molecules of HFC in the adsorption step. In each radical injection cycle of MD simulation, four CH_2F radicals are injected as described above with an incident energy of 0.5 eV. This incident energy is higher than the typical thermal energy of radicals in plasma but much lower than typical bond energies, so the irradiation of a surface with such radicals only allows the adsorption of incident species without much affecting the surface chemical compositions or structures. On the other hand, the incident energy of 0.5 eV, slightly higher than the thermal energy, speeds up the gas-phase transport of such species, which makes the simulation more efficient. The simulated radical adsorption process leads to the formation of a polymer-like layer, similar to the experimental observations [23, 35, 75] . The radical injection cycle of MD simulation is repeated 225 times so that the total dose of CH_2F radicals is 9.56×10^{15} cm^{-2} in the adsorption step of each ALE cycle.

For the desorption process, the surface covered with the HFC polymer is irradiated with energetic Ar ions. In each ion-injection cycle of our MD simulation, a single Ar ion is injected into the material surface with a given kinetic energy. We examined the cases with 150 eV and 300 eV ion energies. The durations of NVE and cooling simulations are the same as above. The Ar ion injection cycle of MD simulation is repeated 1000 times so that the total dose of Ar ions is 1.06×10^{16} cm^{-2} in the desorption step of each ALE cycle.

To represent an O_2 plasma irradiation step, we irradiate the surface with low-

Incident gas species			Energies and doses
Adsorption step	CH_2F	Incident Energy Radical dose	0.5 eV 9.56×10^{15} cm^{-2}
Desorption step	Ar^+	Incident Energy Ion dose	150 - 300 eV 1.06×10^{16} cm^{-2}
O_2 plasma irradiation step	O	Incident Energy Ion dose	15 eV 1.596×10^{15} cm^{-2}

Table 4.1: The MD simulation conditions of this study for each SiN PE-ALE cycle.

energy O ions only, without O radicals, to focus on the effects of the formation of an oxidized layer with a finite thickness, allowing fast-moving O atoms to penetrate the surface slightly. In each ion-injection cycle of our MD simulation, two O ions with a kinetic energy of 15 eV are injected into the material surface. The durations of NVE and cooling simulations are the same as above. The O ion injection cycle of MD simulation is repeated 75 times so that the total dose of O ions is 1.596×10^{15} cm^{-2} in the O_2 plasma irradiation step of each ALE cycle.

In reality, a far larger number of O radicals are expected to arrive at the surface with thermal energy than O ions. However, the oxidation effects by O radicals are limited only to the top surface due to their low kinetic energy and excess O radicals that do not bond with surface atoms are bounced back to the gas phase. In our simulation, our simplified model of 15 eV O injection into the surface is expected to include the oxidation effects by thermal-energy O radicals qualitatively.

Table 4.1 summarises the simulation conditions discussed above. In this study, the standard ALE process of SiN without an O_2 plasma irradiation step is called two-step ALE, as its cycle consists of the adsorption and desorption steps only. With an additional O_2 plasma irradiation step right after the desorption step in each ALE cycle, the process is called a three-step ALE.

4.3 Results and discussions

Figure 4.2 shows the side views of the model materials and the depth profiles of their atomic densities before and after the adsorption step of the 1st ALE cycle of SiN, obtained from MD simulation. As in Fig. 4.1, the beige and blue spheres represent Si and N atoms. The gray, sky blue, and black spheres represent hydrogen (H), fluorine (F), and C atoms, respectively. The origin of the depth profiles indicates the position of the initial top surface. The depth profile of the atomic densities is taken as the number density averaged over a depth of 0.3 nm around the indicated depth.

The initial model material shown in Fig. 4.1 is given in (a). It is seen that the ratio of the Si density to the N density is about 3:4, representing the stoichiometry of the model material of Si_3N_4. The depth profiles are given by sharply undulating curves, reflecting the crystalline structure of the initial model material. The model material after the adsorption step of the first ALE cycle is given in (b), where the SiN model material was exposed to CH_2F radicals. It is seen that the HFC film thickness is about 2 nm.

In the subsequent desorption step, the surface shown in Fig. 4.2(b) is irradiated by energetic Ar ions. In the three-step ALE, an additional step of O ion irradiation follows. In our MD simulation, we repeated ALE cycles 5 times. Figure 4.3 shows the surface heights (measured from the initial surface position) as functions of the radical and ion dose under different ALE conditions. Shown in (a) and (b) are the two-step and three-step ALE processes. In both ALE processes, with 150 eV Ar ion irradiation during the desorption process, the surface heights increase, i.e., HFC film deposition continues without etching of the underlying SiN.

In both ALE processes, with 300 eV Ar ion irradiation during the desorption

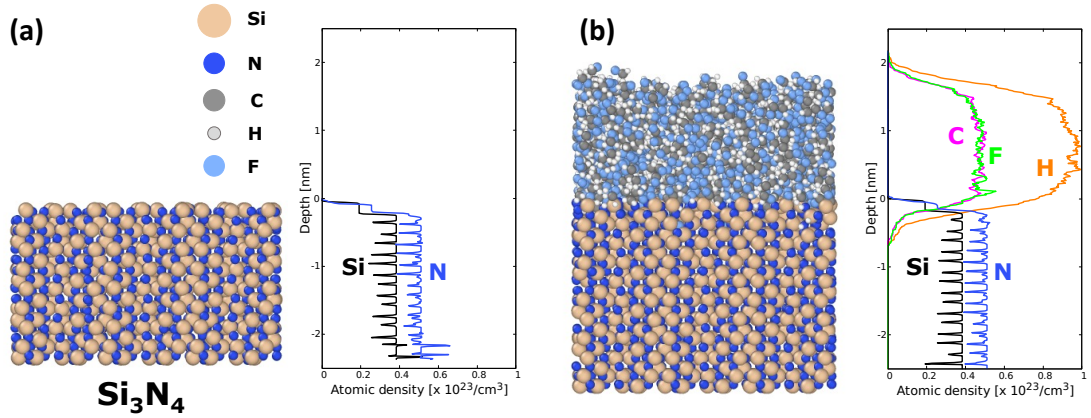

Figure 4.2: Side views of the model materials and the depth profiles of their atomic concentrations (a) before and (b) after the adsorption step of the 1st ALE cycle of SiN, obtained from MD simulation. The horizontal axis of the depth profile represents the atomic concentrations, and the vertical axis represents the depth or height measured from the position of the top surface of the initial model material. As in Fig. 4.1, the beige and blue spheres represent Si and N atoms. The gray, sky blue, and black spheres represent H, F, and C atoms, respectively.

process, net etching is seen to take place. In the two-step ALE process of (a), however, the decay of height is slower than in the three-step ALE process of (b). At 300 eV in (b), during the latter half of the desorption process, the surface height decreases with the same rate as that of physical sputtering of SiN, indicating that deposited HFC hardly exists on the SiN surface during this period. It indicates that the 3rd step of O ion irradiation in (b) contributes to the efficient removal of HFC from the surface.

It is also seen that the total etched depth after 5 ALE cycles in (b) is somewhat larger than that in (a). After many cycles, this difference is expected to increase. This result qualitatively agrees with the previous experimental observations by Hirata et al. [23] with a capacitively coupled plasma (CCP) system and desorption steps with an Ar ion energy of about 330 eV, which showed that the three-step ALE, with O_2 plasma irradiation step, enhanced the total etched depth.

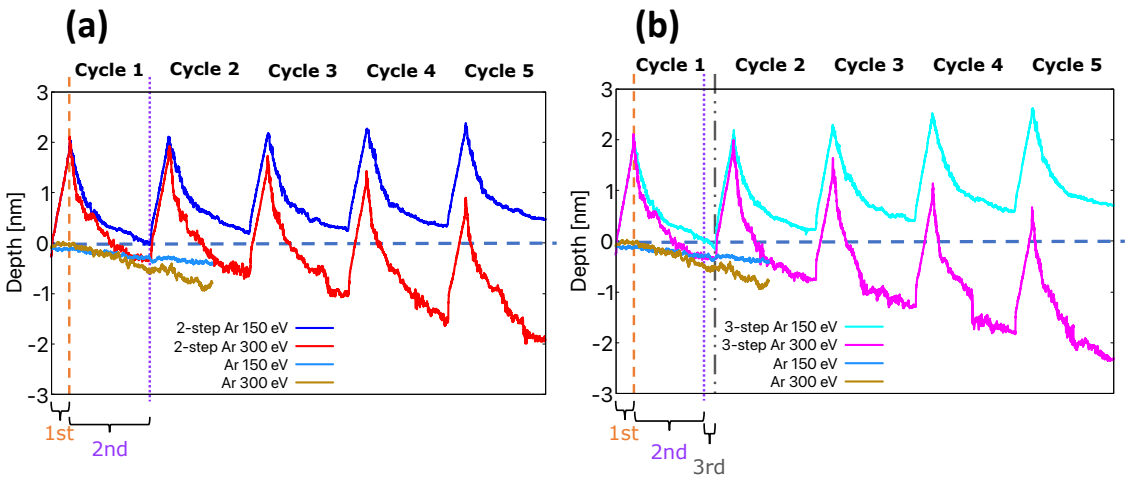

Figure 4.3: Depths (i.e., the positions of the top surface) as functions of the radical and ion dose for (a) two-step and (b) three-step ALE processes obtained from MD simulations. The ALE process conditions are the same, as given in Table 4.1, and the only difference is the Ar ion energy in the desorption process. The blue and sky blue curves represent the cases with 150 eV Ar ions, and the red and pink curves represent the cases with 300 eV Ar ions. The vertical broken and dotted lines indicate the dose at which the 1st and 2nd steps of the 1st ALE cycle end, and the vertical dotted-broken line of (b) indicates the dose at which the O ion irradiation step ends. The blue and brown curves represent the position of the SiN model surface exposed only to Ar ion irradiation with an ion energy of 150 and 300 eV as functions of the ion dose, i.e., the change in SiN surface position due to physical sputtering by Ar ions only.

Figure 4.4 shows the depth profiles of atomic densities after the 5th PE-ALE cycle for SiN. The process conditions are the same as those of Fig. 4.3. With 150 eV Ar ion irradiation, the accumulation of the HFC layer is observed in both two-step and three-step processes, corresponding to the increase in surface heights observed in Fig. 4.3. It is clear that the Ar ion energy is not sufficient to remove the thick HFC layer within this desorption time (or Ar ion dose).

With 300 eV Ar ion irradiation, a deeper mixing of C, F, and H atoms takes place, and the net etching of material is achieved, with an etched depth of approximately 1.5 - 2 nm after five PE-ALE cycles in both two-step and

three-step processes. A noticeable difference between the two cases is a lower concentration of C atoms in the three-step process. This indicates that the presence of O atoms in the three-step process effectively suppresses or slows down the accumulation of the C layer on the surface. This finding suggests that introducing an additional O injection step helps mitigate the build-up of C species during the ALE process.

It is seen in Fig. 4.4(b) that, in the three-step process, the surface is oxidized rather extensively. This finding is qualitatively consistent with the experimental observations by Hirata et al. in 2022, where they demonstrated the presence of SiO_2 on the surface after multiple ALE cycles [35] . However, it is not necessary to have an oxidation step in the very last cycle of a three-step PE-ALE because the role of the oxidation step is to reduce a C accumulation in the subsequent adsorption step. Figure 4.5 shows the depth profiles of atomic densities right after the desorption (i.e., Ar ion irradiation) step of the 5th cycle of the three-step PE-ALE process. It is seen that the O density here is much lower than after the oxidation step shown in Fig. 4.4(b), indicating most of the O atoms seen in Fig. 4.4(b) were deposited during the very last oxidation step.

Figure 4.6 shows the depth profiles of the Si-N, Si-C, and Si-O bond densities after the 5th cycle of the two-step and three-step PE-ALE processes for SiN with an Ar ion energy of 300 eV. It is seen that, in both processes, the Si-C bonds are formed. Because the Si-C bond energy (3.73 eV) is slightly higher than the C-C bond energy (3.60 eV) or C-N bond energy (3.16 eV) [106] , the formation of Si-C bonds makes those C atoms less escapable from the surface and promotes further C accumulation in the subsequent cycles. However, in the three-step process, the Si-C bond density is lower than that in the two-step process, indicating that the

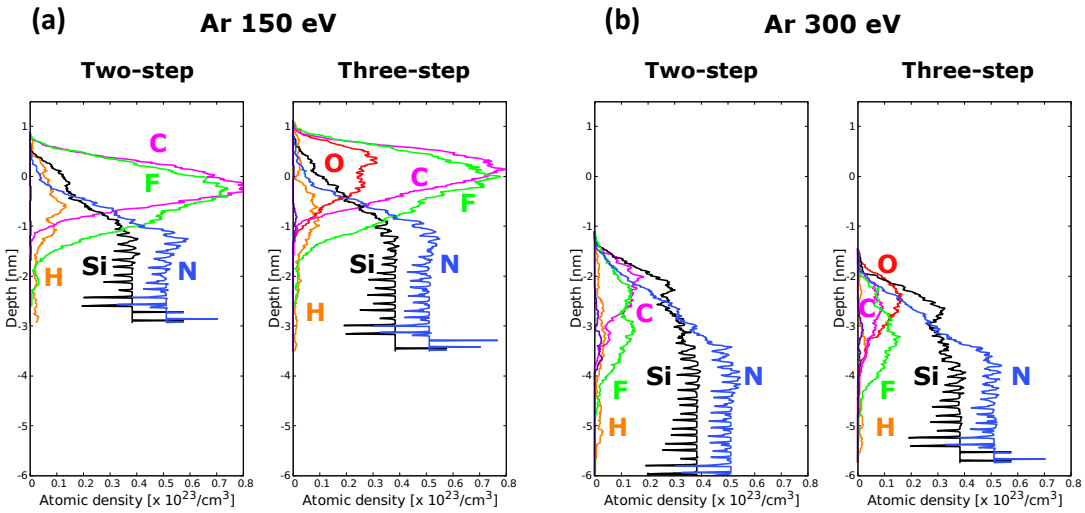

Figure 4.4: Depth profiles of atomic densities after the completion of the 5th cycle of the two-step and three-step PE-ALE processes for SiN with Ar ion energies of (a) 150 eV and (b) 300 eV, obtained from MD simulation.

oxidation step effectively reduces the Si-C bond formation by removing C atoms from the surface.

Figure 4.7 shows the ratios of desorbed gaseous species containing O atoms during the Ar irradiation steps of all 5 cycles of the three-step PE-ALE of SiN with an Ar ion energy of 300 eV. To assess the impact of the oxidation step (i.e., O ion irradiation step) on the PE-ALE process, we focus only on O-containing desorbed species during the Ar ion irradiation steps here. It is seen that a large number of monoatomic O atoms are sputtered off from the surface by Ar ion impact. It is also seen that a significant number of C atoms are removed from the surface as CO. It indicates that the oxidation step significantly aids the removal of C atoms from the surface, preventing further accumulation of C atoms in the subsequent adsorption steps.

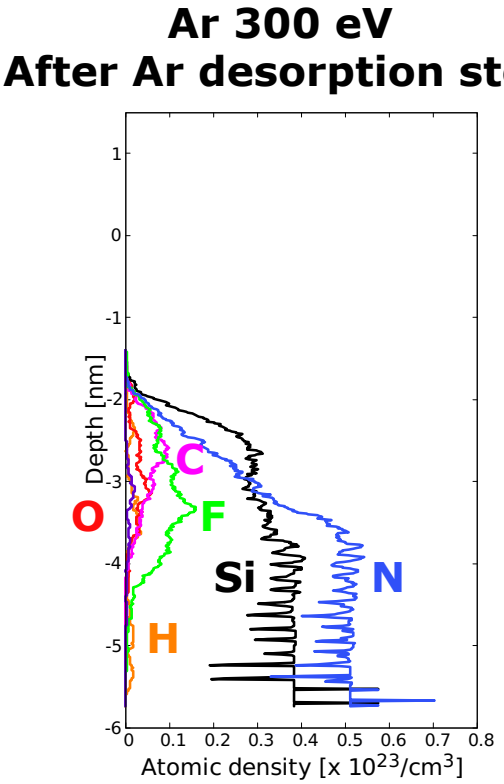

Figure 4.5: Depth profiles of atomic densities right after the desorption (i.e., Ar irradiation) step of the 5th cycle of the three-step PE-ALE process for SiN with an Ar ion energy of 300 eV, obtained from MD simulation.

4.4 Conclusions

In this study, we conducted MD simulations to examine the surface reactions during the two-step and three-step SiN PE-ALE processes. In the three-step PE-ALE, we added an O_2 plasma irradiation step after the Ar ion irradiation step of the two-step PE-ALE for SiN. An earlier experimental study [23] has shown that an introduction of an O_2 plasma irradiation step to the standard two-step ALE of SiN can mitigate an etch-stop problem. In our simulation study, we did not show any specific example where a PE-ALE process of SiN that leads to an etch stop can continue to etch the material with an addition of an O_2 plasma

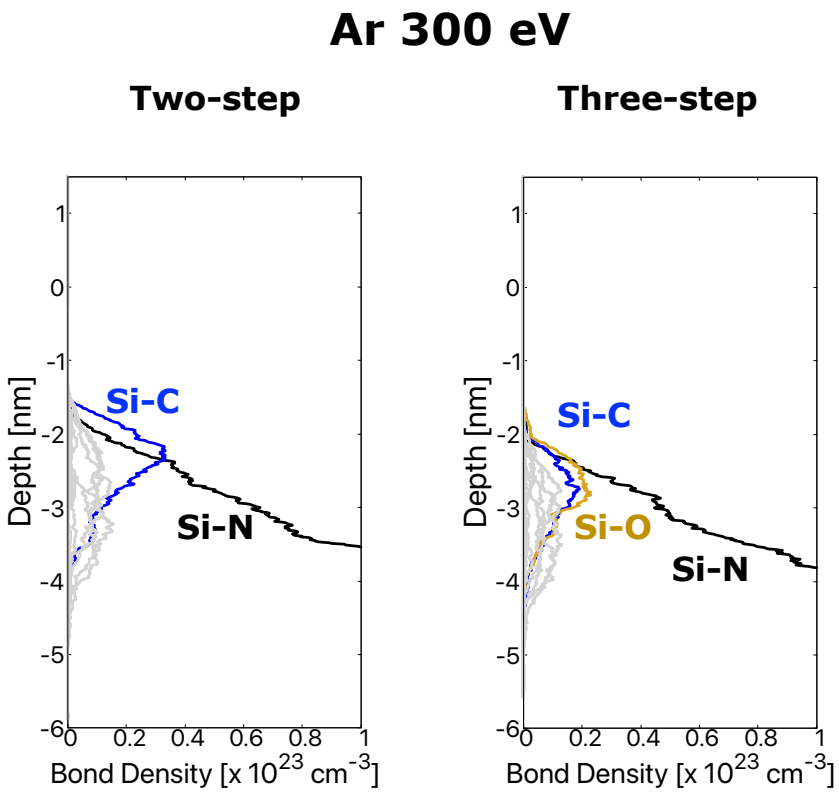

Figure 4.6: Depth profiles of the Si-N, Si-C, and Si-O bond densities after the 5th cycle of the two-step and three-step PE-ALE processes for SiN with an Ar ion energy of 300 eV, obtained from MD simulation. The densities of other bonds are lower than those of the three types of bonds above, as shown with the gray curves.

irradiation step. Instead, we examined the difference in C accumulation between PE-ALE processes that can etch SiN up to 5 ALE cycles and demonstrated that the three-step PE-ALE of SiN could more efficiently remove the deposited HFC layer together with the underlying SiN and reach the self-limit. It also shows that the presence of O atoms played a crucial role in preventing or minimizing C accumulation by facilitating the formation of CO species. This mechanism effectively removed excess C atoms from the surface, preventing the build-up of the HFC layer. The results are in good agreement with experimental observations.

We have also shown that the damage caused by surface oxidation can be

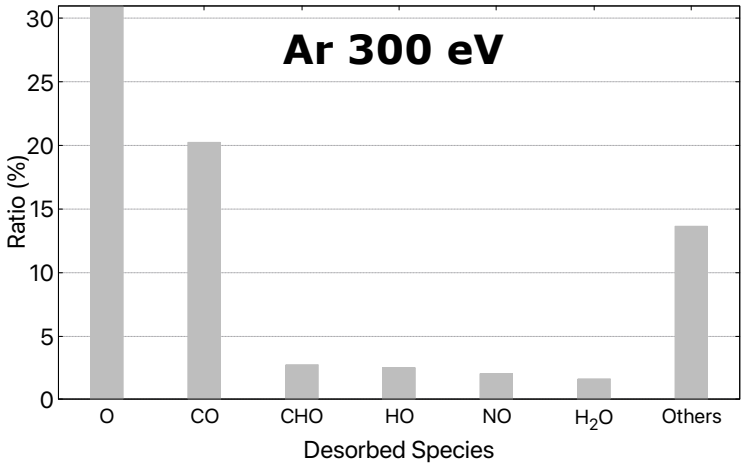

Figure 4.7: Ratios of desorbed gaseous species containing O atoms during the Ar irradiation steps of all 5 cycles of the three-step PE-ALE of SiN with an Ar ion energy of 300 eV, obtained from MD simulation. It should be noted that any species that do not contain O atoms, such as SiF, are not counted here and the desorbed or reflected species during the adsorption or oxidation step are not counted, either.

minimized by not performing the O_2 plasma irradiation step in the final PE-ALE cycle. Thus our results corroborate the experimental observation that the additional O_2 plasma irradiation step can be a valuable tool in enhancing the precision and control of the SiN PE-ALE technique.

Chapter 5

PE-ALE of SiN with Ar, Kr, and Xe ion irradiations

5.1 Introduction

Plasma-enhanced atomic layer etching (PE-ALE) is a technique to etch a material's surface, ideally in a layer-by-layer manner, typically using surface irradiation with low-energy ions generated in a plasma formed with an inert gas such as argon (Ar) [1, 2, 58, 59, 70, 71, 73].The PE-ALE process is made of cyclic processes involving sequential and typically self-limiting surface reaction processes. More specifically, each cycle of a PE-ALE process typically consists of adsorption and desorption steps. Some PE-ALE steps have more than two steps in a single cycle, as seen in this article later. In a typical adsorption step, the material surface to be etched is exposed to gas-phase molecules or radicals that modify the material surface. In the desorption step, the modified surface is exposed to low-energy inert-gas ions and some surface atoms are removed by chemically enhanced sputtering. Ideally, the energy of the incident inert gas ions should be high enough to etch the modified

layer, but low enough to etch the pristine material surface. In this way, once the deposited species introduced in the adsorption are nearly exhausted, the etching stops and thus a self-limiting desorption of the surface material can be achieved.

PE-ALE has been extensively studied due to its importance in meeting the current needs of the semiconductor industry. As the dimensions of advanced semiconductor devices continue to diminish and complex three-dimensional device structures are employed, demand for more precise etching to remove thin layers has increased [4, 27, 67, 72].Horiike et al. performed pioneering research on PE-ALE of silicon (Si) in 1990 [5, 24].In their method, the adsorption step was performed with halogen coverage and the desorption step was performed with Ar plasma irradiation. Since then, most studies on PE-ALE of Si have been performed with chlorine (Cl) adsorption [6–9, 74].PE-ALE processes are often used together with more conventional reactive ion etching (RIE) [54, 56, 68] to achieve the most efficient and precise etching results.

Gaining a comprehensive understanding of PE-ALE processes is important for further development of this etching technology. In this study, we examine atomic-scale surface reactions during silicon nitride (SiN) PE-ALE processes, using numerical simulations. In what follows, the abbreviation SiN denotes a general silicon nitride with an arbitrary stoichiometry, i.e., SiNx, as typical SiN films used in the semiconductor industry are not crystalline. In a typical SiN PE-ALE process, the surface is first exposed to hydrofluorocarbon (HFC) precursors, which modify the material surface chemically, in its adsorption step. In the subsequent desorption step, the modified surface layer is irradiated with low-energy Ar ions. In the current fabrication methods, Ar ions are usually employed due to their wide availability and low cost. However, other non-reactive ions can be also used

in the desorption step. Although, in the adsorption step, HFC precursor radicals are expected to deposit on the surface, too much carbon (C) deposition can result in an etch stop [20, 23]. Therefore, O_2 plasma irradiation is employed to help minimize C accumulation on the surface [13, 35, 83].

The goal of this study is to clarify the surface reactions on the atomic scale during SiN PE-ALE processes with ions made of different inert gases, i.e., Ar, krypton (Kr), and xenon (Xe) under the otherwise same conditions, using molecular dynamics (MD) simulations. It is known that while being non-reactive species, these inert gas species exhibit unique characteristics originating from differences in atomic sizes, mass, and ionization energies. There have been a few attempts to understand their influence on etching in general [107–109] but, to the best of the authors' knowledge, no study has been published on the effects of Kr^+, and Xe^+ ion irradiation in PE-ALE processes although there have been several studies on Kr and Xe low-temperature plasmas [110–112].

5.2 MD simulation

We performed MD simulations to study the effect of different inert gas ions in the desorption step on the SiN PE-ALE process. The simulation method is essentially the same as that of Ref. 83. A rectangular SiN model material used in the simulations of this study represents a nearly crystalline Si_3N_4 with a surface area of 4.035×2.33 nm^2 and an initial depth of 2.25 nm. Although typical SiN films used in semiconductor processes are amorphous and may contain some hydrogen (H) atoms, we use a crystalline SiN as the initial material structure for simplicity, assuming that the simulations would effectively represent the qualitative nature of PE-ALE processes of SiN with a low H content. This is because, as we shall see in Sect. 5.3, the surface is amorphized by ion bombardment in any way.

For the model to mimic an infinitely large surface layer, periodic boundary conditions were applied in the horizontal, i.e., x and y, directions. The depth of the SiN model material in the negative z-direction increases during the simulation as the etching proceeds. More specifically additional layers of the same SiN material are added whenever the system temperature exceeds a pre-defined threshold value or incident atoms pass through the bottom. During the simulations, the atoms in the bottom two monolayers of the model material were fixed in position to prevent the downward drift of the surface model due to the momentum transfer from the incident ions.

All atomic species involved in the simulations, including incident ions, were treated as charge-neutral atoms in terms of interatomic interactions, as Ref. 83. This is likely to be justified because of a possible neutralization of incident ions by the Auger effect immediately before the [113]. Incident species were injected at randomly selected horizontal positions with pre-specified incident energies from

sufficiently above the top material surface. The angle of incidence was set to be normal to the initial top surface. The initial surface temperature was 300 K. The equation of motion for each atom in the system was integrated numerically. For the interactions with inert-gas ions, the two-body interactions were integrated using the Moliére repulsive pair potential function [46, 114]. The other force-field models were, as in Ref. 83, based on the modified Stillinger-Weber-type interatomic potential functions, [45, 46, 104] whose parameters are [83] found in Appendix A. Comprehensive details and technical information on the comparisons between simulations and experimental results can be found in Refs. 9, 35, 83, 91–94, 96, 97.

The simulation of a SiN PE-ALE process is composed of computational surface-irradiation cycles of radical or ion irradiation. At the start of each computational surface-irradiation cycle, a single ionic species or multiple radical species are injected into the SiN model material, as described above, and the MD simulation continues under microcanonical ensemble (NVE) conditions for 0.5 ps. Then the system temperature is gradually brought down toward the initial temperature of 300 K by the Langevin thermostat [51, 98]for the following 1.4 ps and then, by the Berendsen thermostat [99, 100] for the following 0.1 ps. The total time for a computation surface-irradiation cycle is thus 2.0 ps.

In this study, the SiN PE-ALE process consists of three separate steps, i.e., the adsorption step, the desorption step, and the O_2 plasma irradiation step [35, 83]. Each step is simulated with a series of corresponding computation surface-irradiation cycles. The details of the simulation conditions and parameters are presented in Table 5.1.

In the adsorption step, CH_2F radicals, a representative radical species from a

Incident gas species			Energies and doses
Adsorption step	CH_2F	Incident Energy Radical dose	0.5 eV 9.56×10^{15} cm^{-2}
Desorption step	Ar^+, Kr^+, Xe^+	Incident Energy Ion dose	300 eV 1.06×10^{16} cm^{-2}
O_2 plasma irradiation step	O	Incident Energy Ion dose	15 eV 1.596×10^{15} cm^{-2}

Table 5.1: Simulation conditions for each cycle of the SiN PE-ALE process.

plasma formed with HFC molecules, are deposited on the surface. The choice of CH_2F radicals was motivated by the experimental study by Hirata et al. of Ref. [23], where a CH_3F/Ar gas mixture was used. Among possible C-containing species (as C is the primary focus of this work) generated from a CH_3F gas in a plasma, we selected CH_2F because it is a radical species (having a higher sticking coefficient), contained both H and fluorine (F) (both of which are known to etch SiN), and contained more H atoms than F atoms (because the etch rate of SiN typically increases with a higher H content in a fluorocarbon plasma).[79, 80, 91, 115]

In each computational surface-irradiation cycle, four CH_2F radicals are injected into the surface at randomly selected horizontal positions with an incident energy of 0.5 eV each. This energy, higher than typical thermal energies but lower than typical bond energies, enables computationally faster adsorption of those radicals without significantly affecting the surface chemical compositions. The angle of incidence is assumed to be normal to the initial surface for simplicity. For each adsorption step, this computational radical injection cycle was repeated 225 times to simulate a total CH_2F radical dose of 9.56×10^{15} cm^{-2}. As will be seen later, a 2 nm thick HFC polymer layer is deposited on the SiN model material in a single adsorption step.

In the desorption step, the SiN model material surface with an HFC polymer

layer deposited on it is exposed to energetic inert gas ions (Ar^+, Kr^+, and Xe^+) with an incident energy of 300 eV and an ion dose of 1.06×10^{16} cm^{-2}. In each computational surface-irradiation cycle for this step, a single inert-gas ion is injected into the surface at a randomly selected horizontal position with an incident energy of 300 eV. This computational inert-ion injection cycle was repeated 1000 times.

The O_2 plasma irradiation step, in which the surface was exposed to O_2 plasmas without a bias voltage, followed the desorption step discussed above. In the actual O_2 plasma irradiation step, the surface was irradiated with both ions and radicals (as well as O_2 molecules). For example, when the surface is irradiated with O radicals, it takes a long time for the adsorbed O atoms to diffuse into the subsurface region, where they interact with the remaining C atoms. Therefore, in the simulation, we neglected the irradiation of O atoms and injected only low-energy O ions that penetrated the surface more rapidly, to expedite the simulation while maintaining the physical effects of O atoms interacting with remaining subsurface C atoms. To further speed up the simulation, in each computational surface-irradiation cycle for this step, two separate atomic O ions (rather than a single O ion) were injected at random locations, typically away from each other, with each O ion having an incident energy of 15 eV. The computational O ion injection cycle was repeated 75 times, equivalent to an ion dose of 1.596×10^{15} cm^{-2}.

5.3 Results and discussions

5.3.1 Different regimes of surface desorption

Figure 5.1 shows changes in the height of the SiN material surfaces with and without HFC adsorption as functions of the Ar^+ ion irradiation dose, obtained from the MD simulations. The ion incident energy is 300 eV. After the SiN model material with the flat top surface is exposed to CH_2F radicals, as described above, an HFC layer is deposited and the position of its top surface is about 2 nm above the position of the initial top surface of the SiN model material (denoted as 0 nm). The top curve of Fig. 5.1 (labelled as "with HFC") represents the position of the top surface of the material with an HFC layer. (More precisely, it represents the position of the atom whose z-coordinate value is the largest among all atoms covalently attached to the surface material.) On the other hand, the bottom curve (labelled as "without HFC") indicates the position of the top surface of the SiN model material without HFC deposition as a function of the Ar^+ ion dose. In other words, the height of the SiN model material when its surface is physically sputtered by 300 eV Ar^+ ions. As we discussed in Sect. 5.2, the atomic interactions of all species, including incident ions, were treated as charge-neutral atoms.

In the case of HFC adsorption, three different regimes of surface desorption were observed as denoted by I, II, and III in Fig. 5.1. During regime I, adsorbed C, fluorine (F), and hydrogen (H) atoms were mostly removed from the surface while incident ion impact also move such atoms toward the bulk, forming a mixing layer (i.e., layer where the desorbed atoms and the surface atoms are mixed) around the interface between the HFC layer and the SiN top surface. During regime II, Si and nitrogen (N) atoms were also removed, together with C, F, and H atoms. In

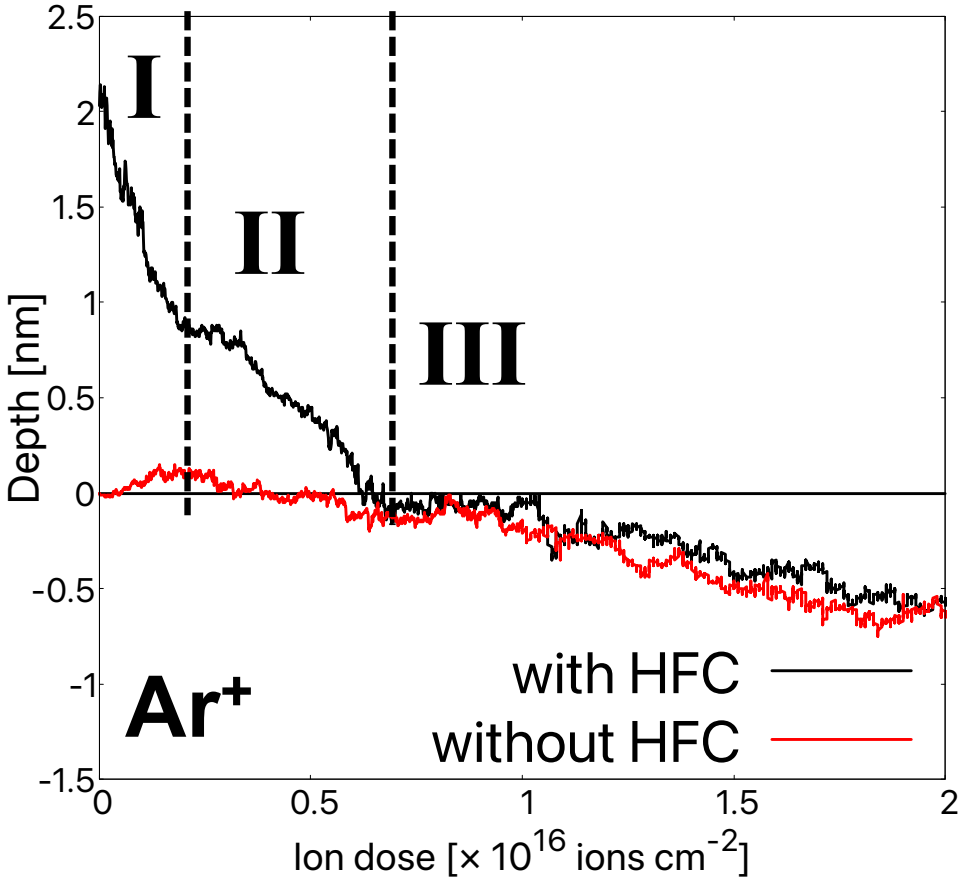

Figure 5.1: Changes in the heights of the material surfaces ion during 300 eV Ar^+ ion irradiation, obtained from MD simulations. With HFC, an about-2-nm-thick HFC layer was deposited on the flat model SiN surface. Without HFC, the flat model SiN surface was etched without HFC deposition. The horizontal axis represents the ion dose. Two vertical broken lines delineate different desorption regimes I, II, and, III, discussed in the main text. For the atomic representations of the surfaces, the reader is referred to Appendix B.

regime III, the deposited C, N, and H atoms were mostly exhausted and physical sputtering of SiN took place. Indeed, the etch rate (which is proportional to the rate of change in height per unit ion dose) for the SiN with HFC adsorption is essentially the same as that by SiN physical sputtering. These three regimes of surface etching are similar to those observed in SiN PE-ALE experiments [20, 75].In what follows, we irradiate inert-gas ions only up to an ion dose of 1.06×10^{16} cm^{-2}, close to the end of regime II in the case of Ar^+ ion irradiation, to minimize the physical sputtering of the SiN film.

5.3.2 SiN PE-ALE mechanisms

Figure 5.2 shows changes in the height of the SiN material surfaces in the case of PE-ALE and physical sputtering (i.e., HFC adsorption) as PE-ALE cycles proceed, obtained from the MD simulations. For the curves representing the cases of physical sputtering (labeled as "physical sputtering"), the horizontal axis is proportional to the inert-gas ion dose. The sputtering yield (i.e., the number of Si atoms removed from the SiN surface per ion injection) can be evaluated from the MD simulations.

In the case of PE-ALE cycles, the adsorption step for CH_2F deposition, the desorption step by inert-gas ion irradiation, and the oxidation step of the first cycle are denoted by ①, ②, and ③, respectively, with delineation by vertical broken lines. From the second cycle on, the different steps are not explicitly delineated for the sake of simplicity, but every cycle consists of those three steps. For the PE-ALE simulations, the horizontal axis is proportional to the dose of incident species in each step with the total dose in each step being given in Table 5.1. Especially in the desorption step, the horizontal axis is proportional to the inert-gas ion dose,

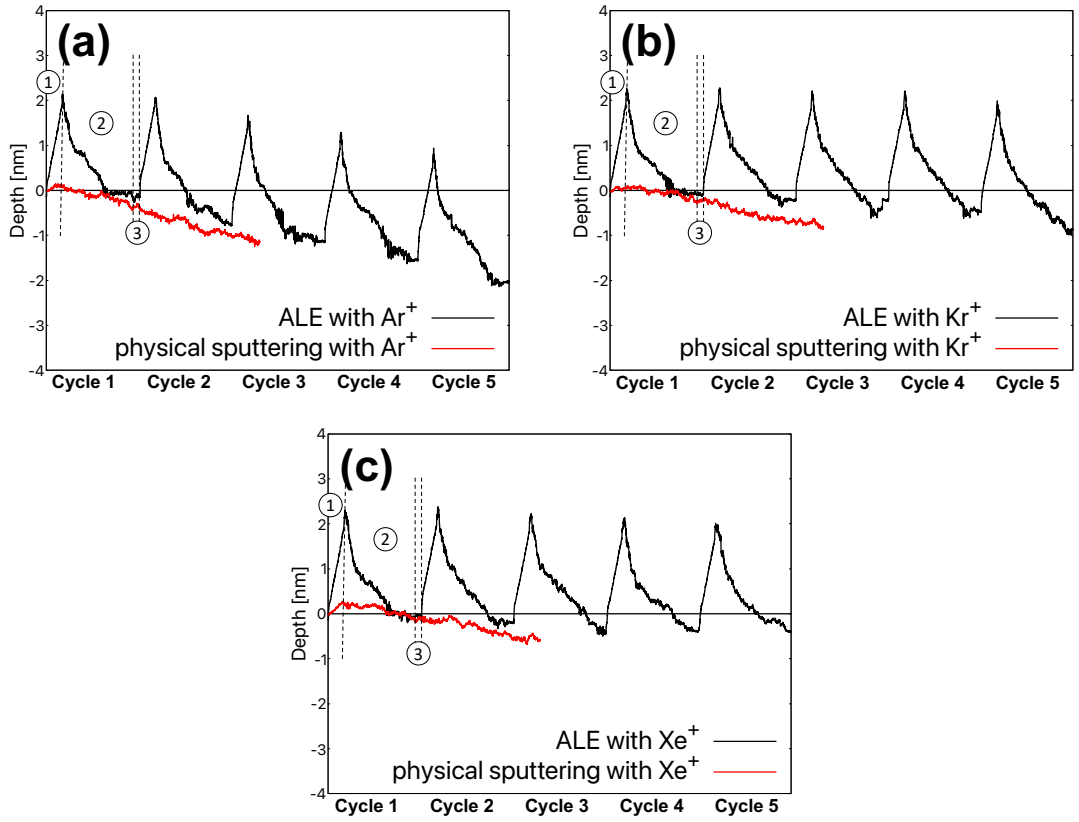

Figure 5.2: Changes in the heights of the material surface during three-step SiN PE-ALE with (a) Ar^+, (b) Kr^+, and (c) Xe^+ ion irradiations over the first five cycles, obtained from MD simulations. Each PE-ALE cycle consists of the adsorption step (denoted by ①), desorption step (②), and oxidation step (③). The lower curves denoted as "physical sputtering" indicate the changes in the SiN material surface positions by physical sputtering with the corresponding ions as functions of the ion dose. For the curves representing the PE-ALE processes, the height changes are also represented as functions of the ion dose during the desorption step and a unit length of the horizontal axis represents the same ion dose for both PE-ALE and physical sputtering curves. The PE-ALE simulation conditions are summarized in Table 5.1.

as for the curves of the corresponding physical sputtering.

As seen in Fig. 5.2, the simulations were performed for five SiN PE-ALE cycles. The cases with Ar^+, Kr^+, and Xe^+ ions are given in (a), (b), and (c), respectively. Similarly to Fig. 5.1, the depth of 0 nm corresponds to the location of the initial top surface of the SiN model material. It is seen that, in each adsorption step, the surface increases by about 2 nm. In each desorption step, the surface height gradually decreases, indicating the etching of the surface material takes place with different etching regimes discussed in the preceding subsection. In the oxidation step, there seems no significant increase in the surface height, suggesting that the incident O ions effectively remove the remaining C atoms without much oxidizing the SiN film [23, 35].

It is seen in all cases that, toward the end of the desorption step, the etch rate slowed down and sometimes became close to that of the corresponding physical sputtering at least in some cycles. This indicates that self-limiting etching was (nearly) achieved. However, it is also observed the total etched depth is much lower in the cases of Kr^+ and Xe^+ ion irradiation.

Figure 5.3 shows the cycle number dependence of the total etched depth of SiN in the PE-ALE processes with Ar^+, Kr^+, and Xe^+ ion irradiations after five cycles, obtained from Fig. 5.2. The total etched depth is defined as the position of the surface (measured from the initial SiN top surface) at the end of each cycle. The average etched depth in a single PE-ALE cycle is called an etch-per-cycle (EPC). From Fig. 5.3, we obtained an EPC of 0.41, 0.17, and 0.08 nm/cycle for the PE-ALE process with Ar^+, Kr^+, and Xe^+ ion irradiations, respectively. However, it is also seen that the etching nearly stopped after the third cycle in the case of Xe^+ ion irradiation.

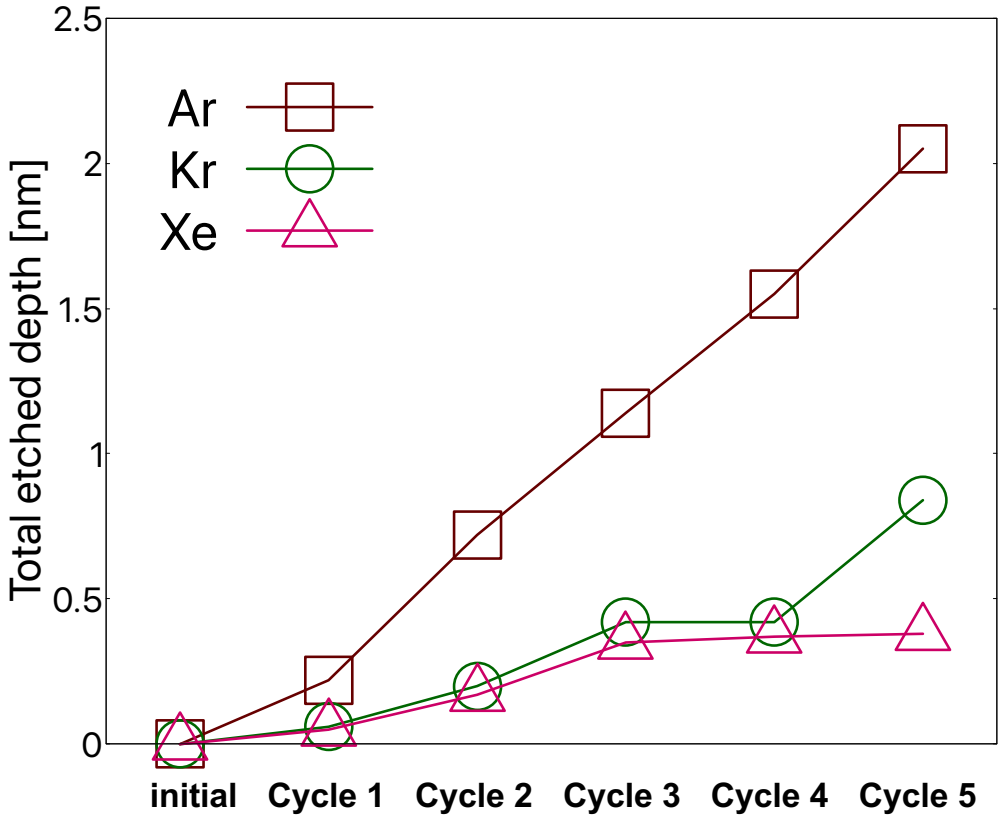

Figure 5.3: Total etched depths after each cycle of the SiN PE-ALE processes with Ar^+, Kr^+, and Xe^+ ion irradiations, evaluated from the MD simulations of Fig. 5.2. The EPC averaged over the five cycles are 0.41, 0.17, and 0.08 nm for the PE-ALE processes with Ar^+, Kr^+, and Xe^+ ion irradiations, respectively.

Figure 5.4 shows the depth profiles of the atomic concentrations at the end of the first SiN PE-ALE cycle (i.e., at the end of the oxidation step of the first cycle) with (a) Ar^+, (b) Kr^+, and (c) Xe^+ ion irradiation. The height or depth is measured from the initial SiN top surface. It is seen in Fig. 5.4 that, some adsorbed C, F, and H atoms penetrated the bulk SiN, due to the knock-on collisions with the incident energetic ions. Some H atoms even reached a depth of about 4 nm. After the oxidation step of the first cycle, the amount of Si oxidation is rather limited (in the sense that the Si density is significantly higher than the O density

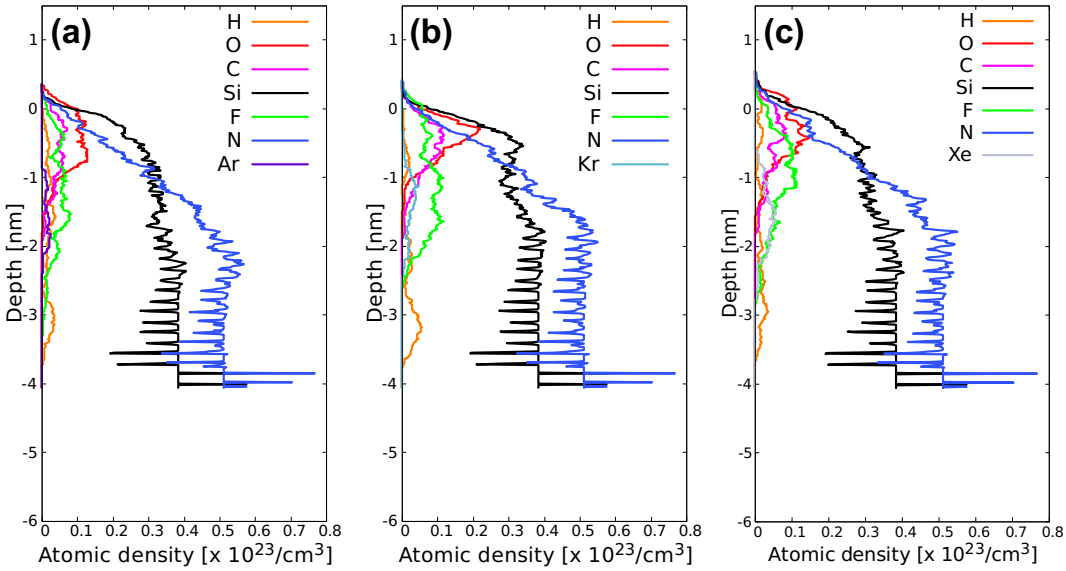

Figure 5.4: Depth profiles of atomic concentrations at the end of the oxidation step of the first SiN PE-ALE cycle with (a) Ar^+, (b) Kr^+, and (c) Xe^+ ion irradiations, obtained from MD simulations.

near the top surface region) and the amount of remaining C species is nearly the same among the three cases.

Figure 5.5 shows the depth profiles of atomic compositions near the etched SiN surfaces right after the desorption step (and before the oxidation step) of the 5th cycle, obtained from the MD simulations. In (a), (b), and (c), atoms of specific species are represented by spheres of the corresponding colors, as indicated in the figure. In (d), (e), and (f), the depth profiles of atomic concentrations are presented, as in Fig. 5.4. The results of the PE-ALE with Ar^+, Kr^+, and Xe^+ ion irradiations are given in (a)/(d), (b)/(e), and (c)/(f), respectively. The top black broken line represents the depth of the material surface measured from the original SiN top surface in each case. The bottom black broken line represents the bottom of the mixed layer, above which a large number of incident atomic species such as C and F exist. (More precisely, the top broken black line is placed at the

depth where the sum of the Si and N atomic densities is one-half of that in the bulk, and the bottom black broken line is placed at which the sum of the C, F, H, and O densities is 10% of the sum of Si and N densities in the bulk.)

Unlike Fig. 5.4, here we plotted the depth profiles after the desorption step and before the oxidation step in the 5th cycle because the oxidation step is needed to remove excess carbon that could enhance the deposition of HFC and hinder the etching in the subsequent step. In addition, in this way, we could see the effects of C accumulation up to the adsorption step of the 5th cycle on the etching of surface atoms in the preceding desorption step.

As we saw in Figs. 5.2 and 5.3, the etched depths in the PE-ALE with Kr^+ and Xe^+ ion irradiations are much lower than that with Ar^+ ion irradiation. This is because there is a significant amount of C accumulation in the cases of Kr^+ and Xe^+ ion irradiations compared with the case of Ar^+ ion irradiation. Such C accumulation hinders the ion impact on the surface and thus the sputtering yield during the desorption step is reduced. Especially in the PE-ALE with Xe^+ ion irradiation, a relatively thick fluorocarbon (FC) layer is formed, which can cause an etch stop. In the simulations, we used the same desorption time (or ion dose in the desorption step) for each inert-gas ion species to evaluate the damage formation under the same conditions. Of course, a longer desorption time allows better removal of remaining C atoms (especially in the case of Kr^+ or Xe^+ ion irradiation), but the thickness of the damaged layer can be also higher under such conditions due to the extended knock-on collision effects. The comparison of the results with Fig. 5.4 suggests that more C atoms accumulate over the PE-ALE cycles in the cases of Kr^+ and Xe^+ ion irradiations than in the case of Ar^+ ion irradiation. (It should be noted that, in Fig. 5.4, the C densities are relatively

small because the profiles were taken after the oxidation step, which is designed to remove excess C atoms.)

5.3.3 Surface damage analysis

The surface damage formation during the SiN PE-ALE process was also evaluated using different inert-gas ions in the desorption step. In Fig. 5.5, it is seen that a mixing layer, i.e., a layer where a large number of the incident species, i.e., C, F, H, and O atoms, form covalent bonds with the bulk atoms, i.e., Si and N, is formed in each case. The thickness of the mixing layer can be defined between the two broken lines, as indicated in the figure. It is seen that the mixing layer thicknesses are nearly the same (about 2 nm) for the three cases with different inert-gas ion irradiations. The results are consistent with experimental observations [20, 75].

On the other hand, it is seen that H atoms more deeply penetrated the bulk SiN in the cases of Kr^+ and Xe^+ ion irradiations. The penetration of H atoms was caused by the knock-on collisions with the energetic incident inert gas ions. It is interesting to note that heavier and thus slower ions, such as Xe^+, do not cause less damage than lighter and thus faster ions such as Ar^+ under the same ion kinetic energy. Because the incident momentum of a heavier ion is higher than that of a lighter ion with the same kinetic energy, the knock-on collision effects by Kr^+ and Xe^+ ions can be stronger than Ar^+, depending on the way the momentum transfer occurs in the mixing layer.

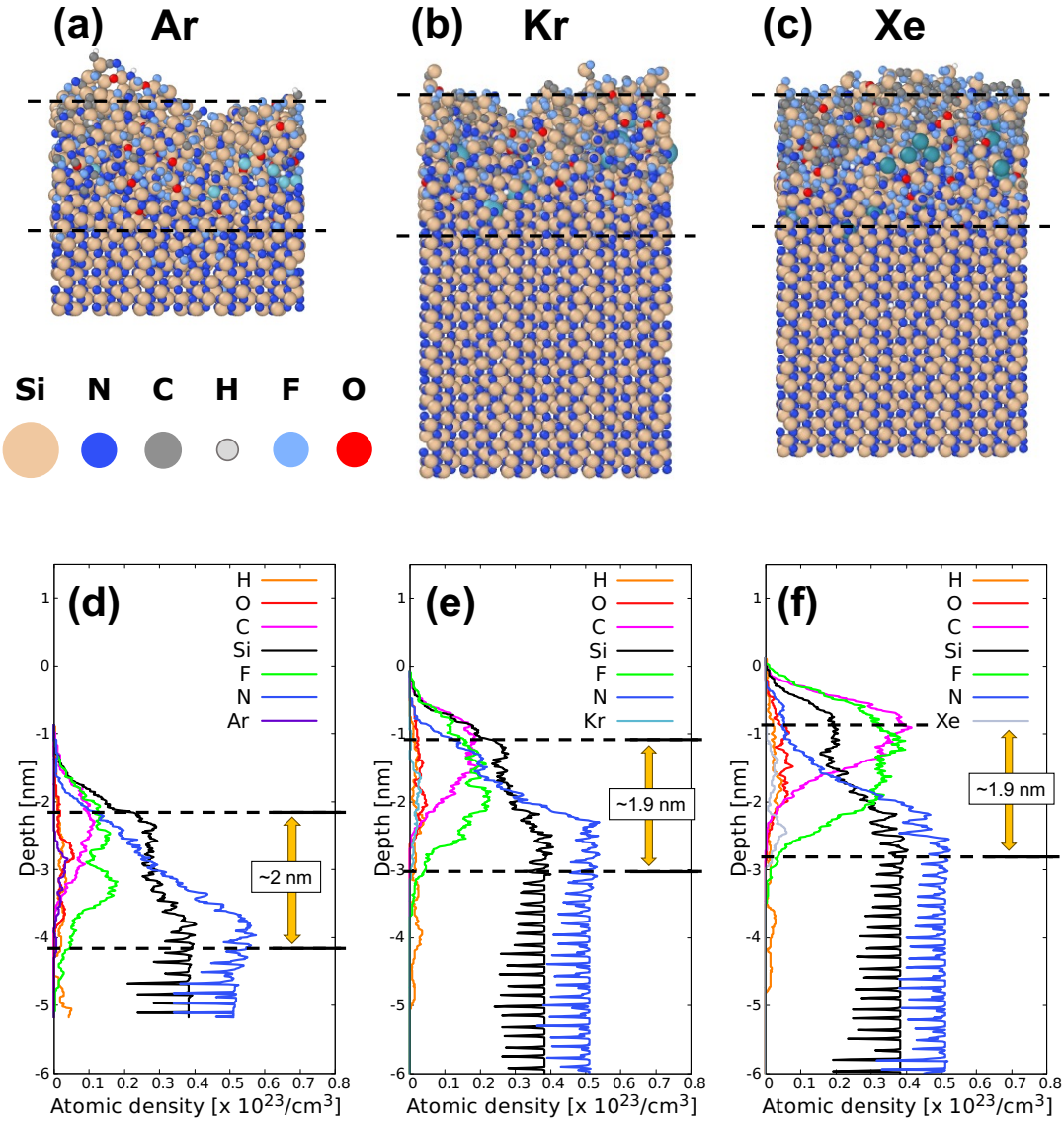

Figure 5.5: Depth profiles of atomic compositions near the etched SiN surfaces right after the desorption step (and before the oxidation step) of the 5th cycle, obtained from the MD simulations of Fig. 5.2. In (a), (b), and (c), atoms of specific species are represented by spheres of the corresponding colors, as indicated in the figure. In (d), (e), and (f), the depth profiles of atomic concentrations are presented, as in Fig. 5.4. The results of the PE-ALE with Ar^+, Kr^+, and Xe^+ ion irradiations are given in (a)/(d), (b)/(e), and (c)/(f), respectively. The region between the two horizontal broken lines represents the mixing layer, which is also considered to be a damaged region of the etched surface.

5.4 Conclusions

MD simulations of 5 cycles of SiN PE-ALE processes were performed with different inert-gas ions, i.e., Ar^+, Kr^+, and Xe^+, in their desorption steps. The study was motivated by the expectation that heavier ions typically have a shorter penetration depth and therefore cause less damage to the etched surface.

First, we examined the first cycle of SiN PE-ALE with an extended period of Ar^+ ion irradiation for the desorption step. It is found that there are three different regimes of surface desorption or etching in the desorption step, denoted by I, II, and III in Fig. 5.1. In the first regime, the removal of the HFC film dominates; in the second regime, the chemical etching of SiN takes place until reactive F and H species are nearly exhausted; and in the third regime, physical sputtering of SiN dominates. This observation is consistent with the experimental observation reported in Ref. 20, 75.

Second, the MD simulations have revealed that the etched depth by PE-ALE with Ar^+ ion irradiation is much larger than those with Kr^+, and Xe^+ ion irradiations. In other words, under the same PE-ALE conditions with HFC adsorption, Ar^+ ion irradiation removes the surface material much more efficiently than Kr^+ or Xe^+ ion irradiation. Less efficient etching by Kr^+ or Xe^+ ion irradiation allows the accumulation of a C layer on the surface over the PE-ALE cycles and the oxidation step used in our study was not efficient enough to remove the excess C. The gradual formation of a C layer, in turn, hinders the effectiveness of ion impact and thus reduces the etch rate. Especially in the case of Xe^+ ion irradiation, we observed that a relatively thick FC layer was formed and the PE-ALE essentially stopped after the third cycle. Over the 5 cycles of SiN PE-ALE processes simulated in this study, the observed depths of EPC were

0.41, 0.17, and 0.08 nm for Ar^+, Kr^+, and Xe^+ ion irradiations, respectively.

Third, we evaluated the damage formation on the etched surfaces. The mixed layer that remains at the end of the desorption step process is considered to be a damaged layer caused by the PE-ALE process. The depths of the mixed layers after the 5th cycle are almost the same (about 2 nm) in all three cases, indicating that ion irradiation by heavier ions such as Kr^+ or Xe^+ ions does not necessarily cause less damage to the surface during the PE-ALE process.

Furthermore, H atoms were found to penetrate the SiN bulk deeply by knock-on collisions with heavier and thus slower incident ions injected into the surface under the same kinetic energy. The overall conclusion is that, for the PE-ALE of SiN, the etching proceeds most efficiently with Ar^+ ions irradiation among all three inert-gas ions examined in this study.

Chapter 6

General conclusion

Classical MD simulations were employed to study the etch-stop mechanism of the SiN PE-ALE process observed in experiments, where each PE-ALE cycle consisted of an HFC adsorption step and an Ar^+ ion irradiation step. The influence of the amount of H or F in the adsorbed HFC layer was examined using CH_2F and CHF_2 as representative HFC precursor radicals. The simulation results revealed three distinct phases during the Ar^+ ion irradiation step: Phase I showed the etching of the accumulated HFC layer and the formation of a mixed layer at the HFC-SiN interface; Phase II showed chemically enhanced etching of SiN through the mixed layer; and Phase III showed physical sputtering of the SiN surface after HFC atoms on the mixed layer were nearly or completely exhausted. Analysis of desorbed species showed that C and H atoms from the HFC layer interacted with N atoms of SiN, leading to the desorption of species like CN, HCN, NH, and NH_2, while F acted as the primary etchant for Si, desorbing SiF and SiF_2, etc. species. The atomic density depth profiles showed that some C, F, and H atoms remained in the material, with H atoms penetrating deeply into the material by knock-on collisions. At higher incident ion energy, preferential sputtering of N

atoms was evident, making the SiN surface Si-rich. The bond density distributions showed that excess C atoms bonded with Si, promoting further C accumulation and leading to etch-stop. Thus, removing excess C atoms is crucial for a stable PE-ALE process, and an additional short oxygen irradiation step could facilitate this removal, enhancing process stability.

Further simulations examined surface reactions during two-step and three-step SiN PE-ALE processes. The three-step process included an O_2 plasma irradiation step after the Ar ion irradiation step. An earlier experimental study showed that the introduction of an O_2 plasma irradiation step to the conventional two-step SiN PE-ALE can mitigate the etch-stop problem. Although the simulations did not show an explicit case where the addition of O_2 plasma continued etching after an etch-stop, we demonstrated that the three-step PE-ALE more efficiently removed the HFC layer and underlying SiN, reaching a self-limiting etch. O atoms played a crucial role by forming CO species, which effectively removed excess C atoms and prevented HFC layer accumulation. These findings are in good agreement with experimental observations. The results of our simulations also showed that surface oxidation damage can be minimized by omitting the O_2 plasma irradiation step in the final cycle. The additional O_2 plasma step enhances the precision and control of the SiN PE-ALE technique.

Simulations of five cycles of SiN PE-ALE processes using different inert-gas ions (Ar^+, Kr^+, Xe^+) in the desorption steps revealed that heavier ions typically have a shorter penetration depth and cause less damage. The first cycle of SiN PE-ALE with extended Ar^+ ion irradiation confirmed three etching regimes: removal of the HFC film, chemical etching of SiN, and physical sputtering of SiN. Ar^+ ions resulted in greater etched depths compared to Kr^+ and Xe^+ ions, with depths of

0.41 nm for Ar^+, 0.17 nm for Kr^+, and 0.08 nm for Xe^+. Less efficient etching by Kr^+ or Xe^+ ions led to C layer accumulation on the surface, reducing etch rates, particularly with Xe^+ ion irradiation, where a thick FC layer stopped the process after the third cycle. The damage layer thickness after the fifth cycle showed no significant difference ($\sim$2 nm) across all inert gas ions, indicating that heavier ions do not necessarily cause less surface damage. H atoms were found to penetrate deeply into the SiN bulk due to knock-on collisions with heavier, slower ions. Overall, Ar^+ ion irradiation was found to be the most efficient for SiN PE-ALE among the ions examined.

Chapter 7

Future Outlook and Recommendations

In this research, we explored the mechanisms of interaction during the SiN PE-ALE process to understand the challenges and problems observed during fabrication. We also investigated potential ways to prevent or minimize these problems, as they could significantly affect the performance of the manufactured devices. By understanding these problems and possible solutions, we are hoping to help improve the overall performance and efficiency of the SiN PE-ALE process.

Despite the findings of this study, achieving stable and uniform monolayer etching of SiN remains a major issue. Currently, comprehensive methods for achieving steady etching are not fully developed, which shows the need for additional research in this field. The precise control required for efficient SiN PE-ALE presents a significant challenge that must be addressed in order to improve device performance.

One possible solution for etching relatively thin layers of SiN involves using a

thin HFC layer during the adsorption step and employing very low ion incident energy with inert gas ions. In our research, we observed thick HFC accumulations during Kr^+ and Xe^+ ion irradiation. To address this, we suggest considering longer desorption periods. However, this could result in higher damage thickness due to extended knock-on collision effects. Therefore, a balanced approach or trade-off is needed.

Additionally, we found that H atoms play an important role in SiN PE-ALE. Therefore, providing an additional supply of H during the desorption step could be efficient. Our simulations show that this approach could improve the etching process. By addressing these specific challenges and enhancing our approaches, we aim to contribute to the development of a more reliable and efficient SiN PE-ALE process.

Bibliography

[1] Keren J. Kanarik, Thorsten Lill, Eric A. Hudson, Saravanapriyan Sriraman, Samantha Tan, Jeffrey Marks, Vahid Vahedi, and Richard A. Gottscho. Overview of atomic layer etching in the semiconductor industry. *Journal of Vacuum Science & Technology A: Vacuum, Surfaces, and Films*, 33:020802, 3 2015.

[2] G. S. Oehrlein, D. Metzler, and C. Li. Atomic layer etching at the tipping point: An overview. *ECS Journal of Solid State Science and Technology*, 4(6):N5041, mar 2015.

[3] Keren J. Kanarik, Samantha Tan, and Richard A. Gottscho. Atomic layer etching: Rethinking the art of etch. *The journal of physical chemistry letters*, 9 16:4814–4821, 2018.

[4] Karsten Arts, Satoshi Hamaguchi, Tomoko Ito, Kazuhiro Karahashi, Harm C M Knoops, Adriaan J M Mackus, and Wilhelmus M M (Erwin) Kessels. Foundations of atomic-level plasma processing in nanoelectronics. *Plasma Sources Science and Technology*, 31:103002, 10 2022.

[5] Hiroyuki Sakaue, Seiji Iseda, Kazushi Asami, Jirou Yamamoto, Masataka

Hirose, and Yasuhiro Horiike. Atomic layer controlled digital etching of silicon. *Japanese Journal of Applied Physics*, 29:2648, 11 1990.

[6] Takashi Matsuura, Junichi Murota, Yasuji Sawada, and Tadahiro Ohmi. Self-limited layer-by-layer etching of si by alternated chlorine adsorption and Ar^+ ion irradiation. *Applied Physics Letters*, 63:2803–2805, 11 1993.

[7] Satish D. Athavale. Realization of atomic layer etching of silicon. *Journal of Vacuum Science & Technology B: Microelectronics and Nanometer Structures*, 14:3702, 11 1996.

[8] Bum-Jun Kim, Saehoon Chung, and Sung M Cho. Layer-by-layer etching of cl-adsorbed silicon surfaces by low energy Ar^+ ion irradiation. *Applied Surface Science*, 187:124–129, 2 2002.

[9] Erin Joy Capdos Tinacba, Michiro Isobe, and Satoshi Hamaguchi. Surface damage formation during atomic layer etching of silicon with chlorine adsorption. *Journal of Vacuum Science & Technology A: Vacuum, Surfaces, and Films*, 39, 7 2021.

[10] H. Nishino, N. Hayasaka, and H. Okano. Damage-free selective etching of si native oxides using NH_3/NF_3 and SF_6/H_2O down-flow etching. *Journal of Applied Physics*, 74:1345–1348, 7 1993.

[11] S. Rauf, T. Sparks, P. L.G. Ventzek, V. V. Smirnov, A. V. Stengach, K. G. Gaynullin, and V. A. Pavlovsky. A molecular dynamics investigation of fluorocarbon based layer-by-layer etching of silicon and si o2. *Journal of Applied Physics*, 101, 2007.

[12] Dominik Metzler, Robert L. Bruce, Sebastian Engelmann, Eric A. Joseph, and Gottlieb S. Oehrlein. Fluorocarbon assisted atomic layer etching of SiO_2 using cyclic Ar/C_4F_8 plasma. *Journal of Vacuum Science & Technology A: Vacuum, Surfaces, and Films*, 32:020603, 3 2014.

[13] Takayoshi Tsutsumi, Hiroki Kondo, Masaru Hori, Masaru Zaitsu, Akiko Kobayashi, Toshihisa Nozawa, and Nobuyoshi Kobayashi. Atomic layer etching of SiO_2 by alternating an O_2 plasma with fluorocarbon film deposition. *Journal of Vacuum Science & Technology A: Vacuum, Surfaces, and Films*, 35:01A103, 1 2017.

[14] Chad M. Huard, Saravanapriyan Sriraman, Alex Paterson, and Mark J. Kushner. Transient behavior in quasi-atomic layer etching of silicon dioxide and silicon nitride in fluorocarbon plasmas. *Journal of Vacuum Science & Technology A*, 36:06B101, 11 2018.

[15] Stefano Dallorto, Andy Goodyear, Mike Cooke, Julia E. Szornel, Craig Ward, Christoph Kastl, Adam Schwartzberg, Ivo W. Rangelow, and Stefano Cabrini. Atomic layer etching of SiO_2 with Ar and CHF_3 plasmas: A self-limiting process for aspect ratio independent etching. *Plasma Processes and Polymers*, 16:1900051, 9 2019.

[16] J. A. Brewer. Ammonium fluoride deposition during plasma etching of silicon nitride. *Journal of Vacuum Science & Technology B: Microelectronics and Nanometer Structures*, 1:932, 1983.

[17] W. R. Knolle and R. D. Huttemann. Ammonium hexafluorosilicate formation during plasma etching of silicon nitride. *Journal of The Electrochemical Society*, 135:2574–2578, 10 1988.

[18] Takashi Matsuura, Yasuhiko Honda, and Junichi Murota. Atomic-order layer-by-layer role-share etching of silicon nitride using an electron cyclotron resonance plasma. *Applied Physics Letters*, 74:3573–3575, 6 1999.

[19] Kazunori Shinoda, Masaru Izawa, Tadamitsu Kanekiyo, Kenji Ishikawa, and Masaru Hori. Thermal cyclic etching of silicon nitride using formation and desorption of ammonium fluorosilicate. *Applied Physics Express*, 9:106201, 10 2016.

[20] Yohei Ishii, Kazumasa Okuma, Tiffany Saldana, Kenji Maeda, Nobuyuki Negishi, and Jim Manos. Atomic layer etching of silicon nitride using cyclic process with hydrofluorocarbon chemistry. *Japanese Journal of Applied Physics*, 56(6S2):06HB07, may 2017.

[21] Sonam D. Sherpa and Alok Ranjan. Quasi-atomic layer etching of silicon nitride. *Journal of Vacuum Science & Technology A*, 35(1), 11 2016. 01A102.

[22] Kazuya Nakane, René H.J. Vervuurt, Takayoshi Tsutsumi, Nobuyoshi Kobayashi, and Masaru Hori. In situ monitoring of surface reactions during atomic layer etching of silicon nitride using hydrogen plasma and fluorine radicals. *ACS Applied Materials and Interfaces*, 11:37263–37269, 10 2019.

[23] Akiko Hirata, Masanaga Fukasawa, Katsuhisa Kugimiya, Kojiro Nagaoka, Kazuhiro Karahashi, Satoshi Hamaguchi, and Hayato Iwamoto. Mechanism of SiN etching rate fluctuation in atomic layer etching. *Journal of Vacuum Science & Technology A*, 38(6), 11 2020. 062601.

[24] Y. Horiike, T. Tanaka, M. Nakano, S. Iseda, H. Sakaue, A. Nagata, H. Shindo, S. Miyazaki, and M. Hirose. Digital chemical vapor deposition

and etching technologies for semiconductor processing. *Journal of Vacuum Science & Technology A: Vacuum, Surfaces, and Films*, 8:1844–1850, 5 1990.

[25] B. E. E. Kastenmeier, P. J. Matsuo, and G. S. Oehrlein. Highly selective etching of silicon nitride over silicon and silicon dioxide. *Journal of Vacuum Science & Technology A*, 17(6):3179–3184, 11 1999.

[26] K. J. Weber and A. W. Blakers. A novel silicon texturization method based on etching through a silicon nitride mask. *Progress in Photovoltaics: Research and Applications*, 13(8):691–695, 2005.

[27] Romuald Blanc, François Leverd, Thibaut David, and Olivier Joubert. Patterning of silicon nitride for CMOS gate spacer technology. I. Mechanisms involved in the silicon consumption in CH_3F/O_2/He high density plasmas. *Journal of Vacuum Science & Technology B*, 31(5), 07 2013. 051801.

[28] Dina H. Triyoso, K. Hempel, S. Ohsiek, V. Jaschke, J. Shu, S. Mutas, K. Dittmar, J. Schaeffer, D. Utess, and M. Lenski. Evaluation of low temperature silicon nitride spacer for high-k metal gate integration. *ECS Journal of Solid State Science and Technology*, 2(11):N222, sep 2013.

[29] Derek Bassett, Wallace Printz, and Takahiro Furukawa. Etching of silicon nitride in 3d nand structures. *ECS Transactions*, 69(8):159, sep 2015.

[30] Taehyeon Kim, Changjin Son, Taegun Park, and Sangwoo Lim. Oxide regrowth mechanism during silicon nitride etching in vertical 3d nand structures. *Microelectronic Engineering*, 221:111191, 2020.

[31] Chung-Hao Fu, Hang-Ting Lue, Tzu-Hsuan Hsu, Wei-Chen Chen, Guan-Ru Lee, Chia-Jung Chiu, Keh-Chung Wang, and Chih-Yuan Lu. A novel

confined nitride-trapping layer device for 3-d nand flash with robust retention performances. *IEEE Transactions on Electron Devices*, 67(3):989–994, 2020.

[32] Lele Chen, Linda Xu, Dongxia Li, and Bill Lin. Mechanism of selective Si_3N_4 etching over SiO_2 in hydrogen-containing fluorocarbon plasma. *Microelectronic Engineering*, 86(11):2354–2357, 2009.

[33] Sanbir S. Kaler, Qiaowei Lou, Vincent M. Donnelly, and Demetre J. Economou. Atomic layer etching of silicon dioxide using alternating C_4F_8 and energetic Ar^+ plasma beams. *Journal of Physics D: Applied Physics*, 50, 5 2017.

[34] Kang-Yi Lin, Chen Li, Sebastian Engelmann, Robert L. Bruce, Eric A. Joseph, Dominik Metzler, and Gottlieb S. Oehrlein. Achieving ultrahigh etching selectivity of sio 2 over si 3 n 4 and si in atomic layer etching by exploiting chemistry of complex hydrofluorocarbon precursors. *Journal of Vacuum Science & Technology A*, 36:040601, 7 2018.

[35] Akiko Hirata, Masanaga Fukasawa, Jomar U. Tercero, Katsuhisa Kugimiya, Yoshiya Hagimoto, Kazuhiro Karahashi, Satoshi Hamaguchi, and Hayato Iwamoto. Five-step plasma-enhanced atomic layer etching of silicon nitride with a stable etched amount per cycle. *Japanese Journal of Applied Physics*, 61, 6 2022.

[36] B. J. Alder and T. E. Wainwright. Phase Transition for a Hard Sphere System. *The Journal of Chemical Physics*, 27(5):1208–1209, 11 1957.

[37] A. R. Leach. *Molecular Modelling: Principles and Applications*. Pearson Education, 2001.

[38] D. Frenkel and B. Smit. *Understanding Molecular Simulation: From Algorithms to Applications*. Academic Press, 2002.

[39] D. C. Rapaport. *The Art of Molecular Dynamics Simulation*. Cambridge University Press, 2004.

[40] S. Plimpton. Fast parallel algorithms for short-range molecular dynamics. *Journal of Computational Physics*, 117(1):1–19, 1995.

[41] Mark James Abraham, Teemu Murtola, Roland Schulz, Szilárd Páll, Jeremy C. Smith, Berk Hess, and Erik Lindahl. Gromacs: High performance molecular simulations through multi-level parallelism from laptops to supercomputers. *SoftwareX*, 1-2:19–25, 2015.

[42] A. P. Thompson, H. M. Aktulga, R. Berger, D. S. Bolintineanu, W. M. Brown, P. S. Crozier, P. J. in 't Veld, A. Kohlmeyer, S. G. Moore, T. D. Nguyen, R. Shan, M. J. Stevens, J. Tranchida, C. Trott, and S. J. Plimpton. LAMMPS - a flexible simulation tool for particle-based materials modeling at the atomic, meso, and continuum scales. *Comp. Phys. Comm.*, 271:108171, 2022.

[43] David A. Case, Thomas E. Cheatham III, Tom Darden, Holger Gohlke, Ray Luo, Kenneth M. Merz Jr., Alexey Onufriev, Carlos Simmerling, Bing Wang, and Robert J. Woods. The amber biomolecular simulation programs. *Journal of Computational Chemistry*, 26(16):1668–1688, 2005.

[44] J.B. Adams. Bonding energy models. In K.H. Jürgen Buschow, Robert W. Cahn, Merton C. Flemings, Bernhard Ilschner, Edward J. Kramer, Subhash

Mahajan, and Patrick Veyssière, editors, *Encyclopedia of Materials: Science and Technology*, pages 763–767. Elsevier, Oxford, 2001.

[45] Frank H. Stillinger and Thomas A. Weber. Computer simulation of local order in condensed phases of silicon. *Phys. Rev. B*, 31:5262–5271, Apr 1985.

[46] H. Ohta and S. Hamaguchi. Molecular dynamics simulation of silicon and silicon dioxide etching by energetic halogen beams. *Journal of Vacuum Science & Technology A*, 19(5):2373–2381, 09 2001.

[47] Wolfgang B. Paul. Molecular dynamics simulation, elementary methods. by j. m. haile, wiley, chichester 1992, 489 pp., hardcover, £ 47.50, isbn 0-471-81966-2. *Advanced Materials*, 5(3):223–224, 1993.

[48] M. P. Allen. Introduction to molecular dynamics simulation. In Norbert Attig, Kurt Binder, Helmut Grubmüller, and Kurt Kremer, editors, *Computational Soft Matter: From Synthetic Polymers to Proteins*, volume 23 of *Lecture Notes*, pages 1–28. John von Neumann Institute for Computing, Jülich, Jülich, 2004. NIC Series, Vol. 23.

[49] William C. Swope, Hans C. Andersen, Peter H. Berens, and Kent R. Wilson. A computer simulation method for the calculation of equilibrium constants for the formation of physical clusters of molecules: Application to small water clusters. *The Journal of Chemical Physics*, 76(1):637–649, 01 1982.

[50] M. P. Allen and D. J. Tildesley. *Computer Simulation of Liquids*. Oxford University Press, Oxford, UK, 2nd edition, 2017.

[51] T. Schneider and E. Stoll. Molecular-dynamics study of a three-dimensional one-component model for distortive phase transitions. *Physical Review B*, 17(3):1302–1322, 02 1978.

[52] J. Hermans, W. F. Van Gunsteren, H. J. C. Berendsen, and J. A. C. Rullmann. *Molecular Dynamics and Monte Carlo Simulations of Condensed Matter Systems*. Springer, Berlin, Germany, 1997.

[53] William G. Hoover. Canonical dynamics: Equilibrium phase-space distributions. *Physical Review A*, 31(3):1695–1697, 1985.

[54] B. Chapman and J. L. Vossen. Glow discharge processes: Sputtering and plasma etching. *Physics Today*, 34:62–62, 7 1981.

[55] S. Hamaguchi. Modeling and simulation methods for plasma processing. *IBM Journal of Research and Development*, 43(1.2):199–215, 1999.

[56] Michael A. Lieberman and Allan J. Lichtenberg. *Principles of Plasma Discharges and Materials Processing*. John Wiley & Sons, Inc., 4 2005.

[57] Toshiaki Makabe and Zoran Lj Petrovic. *Plasma Electronics*. Routledge, Florida, 2016.

[58] Gottlieb S Oehrlein and Satoshi Hamaguchi. Foundations of low-temperature plasma enhanced materials synthesis and etching. *Plasma Sources Science and Technology*, 27(2):023001, feb 2018.

[59] I Adamovich, S Agarwal, E Ahedo, L L Alves, S Baalrud, N Babaeva, A Bogaerts, A Bourdon, P J Bruggeman, C Canal, E H Choi, S Coulombe, Z Donkó, D B Graves, S Hamaguchi, D Hegemann, M Hori, H-H Kim,

G M W Kroesen, M J Kushner, A Laricchiuta, X Li, T E Magin, S Mededovic Thagard, V Miller, A B Murphy, G S Oehrlein, N Puac, R M Sankaran, S Samukawa, M Shiratani, M Šimek, N Tarasenko, K Terashima, E Thomas Jr, J Trieschmann, S Tsikata, M M Turner, I J van der Walt, M C M van de Sanden, and T von Woedtke. The 2022 plasma roadmap: low temperature plasma science and technology. *Journal of Physics D: Applied Physics*, 55:373001, 9 2022.

[60] D.W. Hess, K.F. Jensen, and T.J. Anderson. Chemical vapor deposition: A chemical engineering perspective. *Reviews in Chemical Engineering*, 3(2):97–186, 1985.

[61] D. R. Cote, S. V. Nguyen, A. K. Stamper, D. S. Armbrust, D. Tobben, R. A. Conti, and G. Y. Lee. Plasma-assisted chemical vapor deposition of dielectric thin films for ulsi semiconductor circuits. *IBM Journal of Research and Development*, 43(1.2):5–38, 1999.

[62] R. F. Bunshah and C. V. Deshpandey. Plasma assisted physical vapor deposition processes: A review. *Journal of Vacuum Science & Technology A*, 3(3):553–560, 05 1985.

[63] A. A. Mayo, S. Hamaguchi, J. H. Joo, and S. M. Rossnagel. Across-wafer nonuniformity of long throw sputter deposition. *Journal of Vacuum Science & Technology B: Microelectronics and Nanometer Structures Processing, Measurement, and Phenomena*, 15(5):1788–1793, 09 1997.

[64] S. M. Rossnagel. Thin film deposition with physical vapor deposition and related technologies. *Journal of Vacuum Science & Technology A*, 21(5):S74–S87, 09 2003.

[65] Ulf Helmersson, Martina Lattemann, Johan Bohlmark, Arutiun P. Ehiasarian, and Jon Tomas Gudmundsson. Ionized physical vapor deposition (ipvd): A review of technology and applications. *Thin Solid Films*, 513(1):1–24, 2006.

[66] L. M. Ephrath. Dry etching for vlsi review. *Journal of The Electrochemical Society*, 129(3):62C, mar 1982.

[67] Chris G N Lee, Keren J Kanarik, and Richard A Gottscho. The grand challenges of plasma etching: a manufacturing perspective. *Journal of Physics D: Applied Physics*, 47(27):273001, jun 2014.

[68] Kazuo Nojiri. *Dry Etching Technology for Semiconductors*. Springer International Publishing, 2015.

[69] Ankur Agarwal and Mark J. Kushner. Plasma atomic layer etching using conventional plasma equipment. *Journal of Vacuum Science & Technology A*, 27(1):37–50, 12 2008.

[70] T. Faraz, F. Roozeboom, H. C. M. Knoops, and W. M. M. Kessels. Atomic layer etching: What can we learn from atomic layer deposition? *ECS Journal of Solid State Science and Technology*, 4(6):N5023, mar 2015.

[71] S. U. Engelmann, R. L. Bruce, M. Nakamura, D. Metzler, S. G. Walton, and E. A. Joseph. Challenges of tailoring surface chemistry and plasma/surface interactions to advance atomic layer etching. *ECS Journal of Solid State Science and Technology*, 4(6):N5054, apr 2015.

[72] Colin T. Carver, John J. Plombon, Patricio E. Romero, Satyarth Suri, Tristan A. Tronic, and Robert B. Turkot. Atomic layer etching: An industry

perspective. *ECS Journal of Solid State Science and Technology*, 4(6):N5005, feb 2015.

[73] M. Honda, T. Katsunuma, M. Tabata, A. Tsuji, T. Oishi, T. Hisamatsu, S. Ogawa, and Y. Kihara. Benefits of atomic-level processing by quasi-ALE and ALD technique. *Journal of Physics D Applied Physics*, 50(23):234002, June 2017.

[74] Ivan L. Berry, Keren J. Kanarik, Thorsten Lill, Samantha Tan, Vahid Vahedi, and Richard A. Gottscho. Applying sputtering theory to directional atomic layer etching. *Journal of Vacuum Science & Technology A: Vacuum, Surfaces, and Films*, 36:01B105, 1 2018.

[75] A. Hirata, M. Fukasawa, K. Kugimiya, K. Nagaoka, K. Karahashi, S. Hamaguchi, and H. Iwamoto. On-wafer monitoring and control of ion energy distribution for damage minimization in atomic layer etching processes. *Japanese Journal of Applied Physics*, 59(SJ):SJJC01, mar 2020.

[76] Erin Joy Capdos Tinacba, Tomoko Ito, Kazuhiro Karahashi, Michiro Isobe, and Satoshi Hamaguchi. Molecular dynamics simulation for reactive ion etching of Si and SiO_2 by SF_5^+ ions. *Journal of Vacuum Science & Technology B: Microelectronics and Nanometer Structures*, 39(4):043203, July 2021.

[77] Jomar U. Tercero, Michiro Isobe, Kazuhiro Karahashi, and Satoshi Hamaguchi. Molecular dynamics simulations of silicon nitride atomic layer etching with ar, kr, and xe ion irradiations. submitted.

[78] Jeffery W. Butterbaugh, David C. Gray, and Herbert H. Sawin. Plasma–surface interactions in fluorocarbon etching of silicon dioxide. *Journal of Vacuum Science & Technology B*, 9:1461–1470, 1991.

[79] Tomoko Ito, Kazuhiro Karahashi, Masanaga Fukasawa, Tetsuya Tatsumi, and Satoshi Hamaguchi. Hydrogen effects in hydrofluorocarbon plasma etching of silicon nitride: Beam study with CF, CF_2^+, CHF_2^+, and CH_2F^+ ions. *Journal of Vacuum Science & Technology A*, 29(5), 07 2011. 050601.

[80] Kenichi Yanai, Kazuhiro Karahashi, Kenji Ishikawa, and Moritaka Nakamura. Mass-analyzed CFx^+(x=1,2,3) ion beam study on selectivity of SiO_2-to-SiN etching and a-C:F film deposition. *Journal of Applied Physics*, 97(5):053302, 02 2005.

[81] A.-P. Prskalo, S. Schmauder, C. Ziebert, J. Ye, and S. Ulrich. Molecular dynamics simulations of the sputtering of sic and si3n4. *Surface and Coatings Technology*, 204(12):2081–2084, 2010. Proceedings of the European Materials Research Socierty (E-MRS)Spring Meeting 2009.

[82] Shyam Sridhar, Peter L. G. Ventzek, and Alok Ranjan. Role of physisorption in atomic layer etching of silicon nitride. *Journal of Vacuum Science & Technology A*, 38(4):043007, 06 2020.

[83] Jomar U. Tercero, Akiko Hirata, Michiro Isobe, Kazuhiro Karahashi, Masanaga Fukasawa, and Satoshi Hamaguchi. Surface chemical reactions of etch stop prevention in plasma-enhanced atomic layer etching of silicon nitride. *Surface and Coatings Technology*, 477:130365, 2024.

[84] Satoshi Hamaguchi and Hiroaki Ohta. Surface molecular dynamics of Si/SiO_2 reactive ion etching. *Vacuum*, 66:189–195, 08 2002.

[85] J. Tersoff. New empirical model for the structural properties of silicon. *Phys. Rev. Lett.*, 56:632–635, Feb 1986.

[86] J. Tersoff. New empirical approach for the structure and energy of covalent systems. *Phys. Rev. B*, 37:6991–7000, Apr 1988.

[87] Donald W. Brenner. Empirical potential for hydrocarbons for use in simulating the chemical vapor deposition of diamond films. *Phys. Rev. B*, 42:9458–9471, Nov 1990.

[88] Steven J. Stuart, Alan B. Tutein, and Judith A. Harrison. A reactive potential for hydrocarbons with intermolecular interactions. *The Journal of Chemical Physics*, 112(14):6472–6486, 04 2000.

[89] Hideaki Yamada and Satoshi Hamaguchi. Molecular-dynamics simulations of organic polymer etching by hydrocarbon beams. *Journal of Applied Physics*, 96(11):6147–6152, 12 2004.

[90] David B Graves and Pascal Brault. Molecular dynamics for low temperature plasma-surface interaction studies. *Journal of Physics D: Applied Physics*, 42(19):194011, sep 2009.

[91] Keita Miyake, Tomoko Ito, Michiro Isobe, Kazuhiro Karahashi, Masanaga Fukasawa, Kazunori Nagahata, Tetsuya Tatsumi, and Satoshi Hamaguchi. Characterization of polymer layer formation during SiO_2/SiN etching by fluoro/hydrofluorocarbon plasmas. *Japanese Journal of Applied Physics*, 53(3S2):03DD02, mar 2014.

[92] Erin Joy Capdos Tinacba, Michiro Isobe, Kazuhiro Karahashi, and Satoshi Hamaguchi. Molecular dynamics simulation of Si and SiO_2 reactive ion etching by fluorine-rich ion species. *Surface and Coatings Technology*, 380:125032, 2019.

[93] Nicolas A. Mauchamp and Satoshi Hamaguchi. Molecular dynamics simulation of Si trench etching with SiO_2 hard masks. *Journal of Vacuum Science & Technology A*, 40:053004, 9 2022.

[94] Charisse Marie D. Cagomoc, Michiro Isobe, Eric A. Hudson, and Satoshi Hamaguchi. Molecular dynamics simulation of oxide-nitride bilayer etching with energetic fluorocarbon ions. *Journal of Vacuum Science & Technology A*, 40:063006, 12 2022.

[95] Joseph R. Vella, David Humbird, and David B. Graves. Molecular dynamics study of silicon atomic layer etching by chlorine gas and argon ions. *Journal of Vacuum Science & Technology B*, 40(2):023205, 02 2022.

[96] Charisse Marie D. Cagomoc, Michiro Isobe, Eric A. Hudson, and Satoshi Hamaguchi. Inert-gas ion scattering at grazing incidence on smooth and rough Si and SiO_2 surfaces. *Journal of Vacuum Science & Technology A*, 41:023003, 3 2023.

[97] Charisse Marie D. Cagomoc, Michiro Isobe, and Satoshi Hamaguchi. Molecular dynamics study of SiO_2 nanohole etching by fluorocarbon ions. *Journal of Vacuum Science & Technology A*, 41:023001, 3 2023.

[98] Daan Frenkel, Berend Smit, and Mark A. Ratner. Understanding Molecular

Simulation: From Algorithms to Applications. *Physics Today*, 50(7):66–66, 07 1997.

[99] H. J. C. Berendsen, J. P. M. Postma, W. F. van Gunsteren, A. DiNola, and J. R. Haak. Molecular dynamics with coupling to an external bath. *The Journal of Chemical Physics*, 81:3684–3690, 10 1984.

[100] Stephen C. Harvey, R.-Z. Tan, and Thomas E. Cheatham. The flying ice cube: Velocity rescaling in molecular dynamics leads to violation of energy equipartition. *Journal of Computational Chemistry*, 19, 1998.

[101] V A Godyak, R B Piejak, and B M Alexandrovich. Electron energy distribution function measurements and plasma parameters in inductively coupled argon plasma. *Plasma Sources Science and Technology*, 11(4):525, nov 2002.

[102] Romuald Blanc, Cécile Jenny, Sébastien Lagrasta, François Leverd, and Olivier Joubert. Patterning of silicon nitride for CMOS gate spacer technology. II. Impact of subsilicon surface carbon implantation on epitaxial regrowth. *Journal of Vacuum Science & Technology B*, 32(2), 02 2014. 021806.

[103] Chang Fang, Yanqiang Cao, Di Wu, and Aidong Li. Thermal atomic layer etching: Mechanism, materials and prospects, 12 2018.

[104] P C L Stephenson, M W Radny, and P V Smith. A modified stillinger-weber potential for modelling silicon surfaces, 1996.

[105] Hiroaki Ohta and Satoshi Hamaguchi. Effects of van der waals interactions on SiO_2 etching by CFx plasmas. *J. Plasma Fusion Res. SERIES*, 6:0–000, 2004.

[106] Gorton Carruth and Eugene Ehrlich. *Bond Energies*, volume 1. Southwestern, volume library edition, 2002.

[107] Dong Ho Kim, Gun Hwan Lee, Seung Yup Lee, and Do Hyun Kim. Atomic scale simulation of physical sputtering of silicon oxide and silicon nitride thin films. *Journal of Crystal Growth*, 286:71–77, 1 2006.

[108] Yusuke Kondo, Kenji Ishikawa, Toshio Hayashi, Yudai Miyawaki, Keigo Takeda, Hiroki Kondo, Makoto Sekine, and Masaru Hori. Silicon nitride etching performance of CH_2F_2 plasma diluted with argon or krypton. *Japanese Journal of Applied Physics*, 54, 4 2015.

[109] Youngseok Lee, Heejung Yeom, Daehan Choi, Sijun Kim, Jangjae Lee, Junghyung Kim, Hyochang Lee, and Shin Jae You. Database development of sio2 etching with fluorocarbon plasmas diluted with various noble gases of ar, kr, and xe. *Nanomaterials*, 12, 11 2022.

[110] K. H. Bai, S. J. You, H. Y. Chang, and H. S. Uhm. Plasma parameters analysis of various mixed gas inductively coupled plasmas. *Physics of Plasmas*, 9:2831–2838, 6 2002.

[111] Hyungjoo Shin, Weiye Zhu, Demetre J. Economou, and Vincent M. Donnelly. Ion energy distributions, electron temperatures, and electron densities in ar, kr, and xe pulsed discharges. *Journal of Vacuum Science & Technology A: Vacuum, Surfaces, and Films*, 30, 5 2012.

[112] Yusuke Kondo, Yudai Miyawaki, Kenji Ishikawa, Toshio Hayashi, Keigo Takeda, Hiroki Kondo, Makoto Sekine, and Masaru Hori. Hydrofluorocarbon ion density of argon- or krypton-diluted ch2f2 plasmas: Generation of ch2f+ and chf2+ by dissociative-ionization in charge exchange collisions. *Journal of Physics D: Applied Physics*, 48, 4 2015.

[113] M. Toth, B. L. Thiel, and A. M. Donald. On the role of electron–ion recombination in low vacuum scanning electron microscopy. *Journal of Microscopy*, 205(1):86–95, 2002.

[114] I.M.C. Torrens. *Interatomic Potentials*. Elsevier Science, 1972.

[115] Kazuhiro Karahashi, Ken-ichi Yanai, Kenji Ishikawa, Hideo Tsuboi, Kazuaki Kurihara, and Moritaka Nakamura. Etching yield of SiO2 irradiated by F+,CFx+(x=1,2,3) ion with energies from 250 to 2000 eV. *Journal of Vacuum Science & Technology A*, 22(4):1166–1168, 06 2004.

Chapter 8

Research Achievements

Publications list

- **Jomar U. Tercero**, Akiko Hirata, Michiro Isobe, Kazuhiro Karahashi, Masanaga Fukasawa, and Satoshi Hamaguchi, Surface chemical reactions of etch stop prevention in plasma-enhanced atomic layer etching of silicon nitride, Surface and Coatings Technology 477 (2024) 130365.

- **Jomar U. Tercero**, Michiro Isobe, Kazuhiro Karahashi, and Satoshi Hamaguchi, Molecular dynamics simulations of silicon nitride atomic layer etching with Ar, Kr, and Xe ion irradiations, Japanese Journal of Applied Physics, 63 (2024) 07SP03.

- **Jomar U. Tercero**, Michiro Isobe, Kazuhiro Karahashi, Magdaleno Vasquez, Jr., and Satoshi Hamaguchi, Etch-stop mechanisms in plasma-enhanced atomic layer etching of silicon nitride: a molecular dynamics study, Journal of Vacuum Science & Technology A 42 (2024) 052603.

- Akiko Hirata, Masanaga Fukasawa, **Jomar U. Tercero**, Katsuhisa Kugimiya, Yoshiya Hagimoto, Kazuhiro Karahashi, Satoshi Hamaguchi, Hayato Iwamoto, Five-step plasma-enhanced atomic layer etching of silicon nitride with a stable etched amount per cycle, Japanese Journal of Applied Physics 61 (2022) 066002.

- Akiko Hirata, Masanaga Fukasawa, **Jomar U. Tercero**, Katsuhisa Kugimiya, Yoshiya Hagimoto, Kazuhiro Karahashi, Satoshi Hamaguchi, Hayato Iwamoto, High-throughput SiN ALE: surface reaction and ion-induced damage generation mechanisms, Japanese Journal of Applied Physics 62 (2023) SI1015.

International Conferences (Oral Presentations)

- **J.U. Tercero**, A. Hirata, M. Isobe, M. Fukasawa, M.R. Vasquez, Jr., and S. Hamaguchi, Molecular dynamics study on multi-steps plasma-assisted atomic layer etching of silicon nitride, American Vacuum Society (AVS) 67th Virtual Symposium, October 25-28, 2021.

- **J.U. Tercero**, A. Hirata, M. Isobe, K. Karahashi, M. Fukasawa, M.R. Vasquez, Jr., and S. Hamaguchi, Molecular dynamics simulation of post-etch damage formation in silicon nitride, DPS 2021 Online Symposium, 42nd International Symposium on Dry Processes, November 18-19, 2021.

- **J.U. Tercero**, A. Hirata, M. Isobe, K. Karahashi, M. Fukasawa, and S. Hamaguchi, Damage formation in the underlying silicon after the removal of silicon nitride by atomic layer etching: a molecular dynamics study, 22nd

International Conference on Atomic Layer Deposition (ALD 2022) featuring the 9th International Atomic Layer Etching Workshop, International Convention Center (ICC), Ghent, Belgium, June 26-29, 2022.

- **J.U. Tercero**, A. Hirata, M. Isobe, K. Karahashi, M. Fukasawa, and S. Hamaguchi, Molecular dynamics simulations of plasma-enhanced atomic layer etching of silicon nitride using hydrofluorocarbon and oxygen plasmas, American Vacuum Society (AVS) 68th International Symposium & Exhibition, David L. Lawrence Convention Center, Pittsburgh, PA, USA, November 6-11, 2022.

- **J.U. Tercero**, M. Isobe, K. Karahashi, and S. Hamaguchi, Effects of oxygen addition on plasma-enhanced atomic layer etching of silicon nitride: A molecular dynamics study, Society of Vacuum Coaters 66th annual Technical Conference and Exhibition (TechCon), Gaylord National Resort and Convention Center, National Harbor, Maryland, USA, May 6-11, 2023.

- **J.U. Tercero**, M. Isobe, K. Karahashi, and S. Hamaguchi, Damage formation analyses of steady plasma-enhanced atomic layer etching for silicon nitride with molecular dynamics simulations, AVS 69th International Symposium & Exhibition, Oregon Convention Center, Portland, OR, USA, November 5-10, 2023.

- **J.U. Tercero**, M. Isobe, K. Karahashi, and S. Hamaguchi, Molecular dynamics simulations of the effect of Ar, Kr, and Xe irradiation on silicon nitride atomic layer etching, 44th International Symposium on Dry Process (DPS 2023), Winc Aichi, Nagoya, Japan, November 21-22, 2023.

- **J. U. Tercero**, M. Isobe, T. Ito, K. Karahashi, and S. Hamaguchi, Surface reaction mechanisms in silicon nitride plasma-enhanced atomic layer deposition: Insights from density functional theory, 5th International Symposium of the Vacuum Society of the Philippines (ISVSP 2024), Orchard Hotel, Baguio City, Philippines, January 17-19, 2024.

International Conferences (Poster Presentations)

- **J.U. Tercero**, M. Isobe, K. Karahashi, and S. Hamaguchi, Surface-reaction analyses of multi-step plasma-enhanced atomic layer etching for SiN with molecular dynamics simulation, 14th EU-Japan Joint Symposium on Plasma Processing (JSPP-14), Okinawa Institute of Science and Technology, Okinawa, Japan, April 16-21, 2023.

- **J.U. Tercero**, Y. Okada, M. Isobe, and S. Hamaguchi, Molecular dynamics simulations of silicon dioxide atomic layer etching using fluorocarbon and oxygen plasmas, 25th International Symposium on Plasma Chemistry, Miyako Messe Exhibition Center, Kyoto, Japan, May 21-26, 2023.

- **J.U. Tercero**, A. Y. Jaber, EJ. C. Tinacba, N. A. Mauchamp, M. Isobe, T. Ito, K. Karahashi, M. Krstić, and S. Hamaguchi, Numerical simulation of surface reactions during plasma-enhanced atomic layer deposition (PE-ALD) of silicon nitride (SiN), 23rd International Conference on Atomic Layer Deposition featuring the 10th International Atomic Layer Etching Workshop, Hyatt Regency Bellevue in Bellevue, Washington, USA, July 23-26, 2023.

- **J.U. Tercero**, M. Isobe, T. Ito, K. Karahashi, and S. Hamaguchi, Decomposition and adsorption mechanisms of chlorosilanes and methylchlorosilanes on Si(100) surface, 25th International Plasma School on "Low-Temperature Plasma Physics: Basics and Applications" and its Master Class "Electric Propulsion", (October 1-8, 2022 at Physikzentrum Bad Honnef, Germany).

Domestic Conference (Oral Presentation)

- **J.U. Tercero** and S. Hamaguchi,Effects of oxygen addition on plasma-enhanced atomic layer etching of silicon nitride: A molecular dynamics study, QLEAR Fellowship Research Exchange Workshop, Nanbu Yoichiro Hall, Osaka University, Toyonaka Campus, March 6-8, 2024.

Domestic Conferences (Poster Presentations)

- **J.U. Tercero**, M. Isobe, T. Ito, K. Karahashi, and S. Hamaguchi, Decomposition and adsorption mechanisms of chlorosilanes and methylchlorosilanes on Si(100) surface, 69th Japan Society of Applied Physics (JSAP) Spring Meeting 2022, Aoyama Gakuin University, Sagamihara Campus & Online, March 22-26, 2022.

- **J.U. Tercero** and S. Hamaguchi,Effects of oxygen addition on plasma-enhanced atomic layer etching of silicon nitride: A molecular dynamics study, QLEAR Fellowship Research Exchange Workshop, Nanbu Yoichiro Hall, Osaka University, Toyonaka Campus, March 6-8, 2024.

Awards

- Recipient, Student Sponsorship Program, Society of Vacuum Coaters, May 2023.
- Finalist, Coburn and Winters (C&W) Student Award in Plasma Science and Technology Division (PSTD) of the American Vacuum Society (AVS), November 2023.
- Best Paper Presenter, Surface reaction mechanisms in silicon nitride plasma-enhanced atomic layer deposition: Insights from density functional theory, Computational Materials Science (CMS) Session, 5th International Symposium of the Vacuum Society of the Philippines (ISVSP 2024), Orchard Hotel, Baguio City, January 17-19, 2024.
- Recipient, Osaka University Fellowship "Quantum Leader Resources" (QLEAR Fellowship) April 2022 – September 2024.

Newsletter

- **J.U. Tercero**, M. Isobe, K. Karahashi, and S. Hamaguchi, Effects of oxygen addition on plasma-enhanced atomic layer etching of silicon nitride: A molecular dynamics study, Society of Vacuum Coaters Bulletin Summer 2024 pages 55-65.

Appendix A

Atomic Interactions Potential Parameters

Interaction	a (eVÅ^{2q})	b(eVÅ^{q})	q	d(Å)	r_c(Å)
Si-Si	170.0	38.3	1.89	0.614	3.6
Si - N	425.042	83.5068	1.7302	1.6060	2.99
Si - C	122.0	44.9	2.86	0.176	2.8
Si-H	83.04	34.76	1.34	1.75	3.2
Si-F	75.6	41.7	2.21	0.269	2.6
Si - O	122.0	44.6	2.52	0.453	2.5
N - N	76.9	24.7	1.69	1.14	2.4
N = N	76.9	95.1	1.23	1.98	2.4
N ≡ N	76.9	258	0.806	2.99	2.4
N - C	42.5	26.4	1.8	0.363	2.4
N = C	42.5	51.2	1.57	0.864	2.4
N ≡ C	42.5	83.7	1.43	1.27	2.4
N - H	77.5	39.0	1.10	1.96	2.5
N - F	43.3	23.1	1.88	0.477	2.3
N - O	78.3	30.3	1.71	0.910	2.4
N = O	78.3	83.2	1.55	1.78	2.4
C - C	90.1	36.4	1.30	0.972	2.5
C = C	90.1	41.9	1.73	0.678	2.5
C ≡ C	90.1	103.0	1.02	1.82	2.5
C - H	52.08	31.38	1.16	1.62	2.6
C - F	20.2	20.2	2.39	0.113	2.3
C - O	35.1	23.1	2.16	0.302	2.3
C = O	35.1	45.7	2.18	0.616	2.3
C ≡ O	35.1	51.8	2.04	0.652	2.3
H - H	34.86	26.41	0.73	1.642	2.2
H - F	73.0	42.68	1.11	1.84	2.4
H - O	55.06	33.87	1.285	1.741	2.4
F - F	13.8	9.59	2.58	0.137	2.2
F - O	47.4	20.8	2.33	0.659	2.2
O - O	20.7	11.0	2.06	0.481	2.4
O = O	20.7	69.6	0.209	2.34	2.4

Table A.1: Parameters of the two-body potentials.

	ijk	k (eV)	Θ (°)	γ
h_{sp3}	H – C – H	2.31	-0.333	2.209
C center	H – C – O	2.466	-0.333	1.944
	H – C – C	2.57	-0.333	1.952
	O – C – O	3.67	-0.333	2
	H – C – Si	1.662	-0.333	2.015
	O – C – C	3.66	-0.333	2
	H – C – F	3.384	-0.333	1.985
	C – C – C	4.76	-0.333	2
	O – C – Si	2.72	-0.333	2
	N – C – H	6.59	-0.333	2.6
	O – C – F	4.54	-0.333	2
	C – C – Si	2.96	-0.333	2
	C – C – F	4.28	-0.333	2
	N – C – O	14.4	-0.333	2.7
	Si – C – Si	2.17	-0.332	2
	C – C – N	13.2	-0.333	2.63
	Si – C – F	3.09	-0.33	2
	F – C – F	6.39	-0.333	2
	N – C – Si	5.32	-0.333	2.55
	N – C – F	13.2	-0.333	2.67
	N – C – N	13.1	-0.333	2.69

Table A.2: Parameters of the three-body potentials (h_{sp3} with C as central atom).

	ijk	k (eV)	Θ (°)	γ
h_{sp3}	H - Si – H	2.34	-0.333	2.038
Si center	H – Si – O	1.612	-0.333	1.941
	H – Si – C	2.452	-0.333	2.083
	O – Si – O	3.07	-0.333	2
	H – Si – Si	1.565	-0.333	1.942
	O – Si – C	2.81	-0.333	2
	H – Si – F	2.235	-0.333	2.034
	C – Si – C	3.42	-0.333	2
	O – Si – Si	1.72	-0.333	2
	H – Si – N	6.73	-0.333	2.77
	O – Si – F	2.26	-0.333	2
	C – Si – Si	2.6	-0.333	2
	C – Si – F	2.62	-0.333	2
	N – Si – O	7.65	-0.333	2.63
	Si – Si – Si	2.14	-0.333	2
	C – Si – N	7.8	-0.333	2.67
	Si – Si – F	2.08	-0.333	2
	F – Si – F	2.75	-0.333	2
	N – Si – Si	4.28	-0.333	2.64
	N – Si – F	6.96	-0.333	2.52
	N – Si – N	8.48	-0.333	2.69

Table A.3: Parameters of the three-body potentials (h_{sp3} with Si as central atom).

	ijk	k (eV)	Θ (°)	γ
h_{sp3}	H – O – H	2.551	-0.283	2.081
O center	H – O – O	4.044	-0.231	2.219
	H – O – C	3.018	-0.302	2.215
	O – O – O	5	0	0
	H – O – Si	2.323	-0.348	2.412
	O – O – C	2.21	-0.494	2
	H – O – F	4.678	-0.139	2.491
	C – O – C	4.78	-0.413	2
	O – O – Si	5	0	0
	N – O – H	3.62	-0.216	2.184
	O – O – F	3.53	-0.214	2
	C – O – Si	2.86	-0.524	2
	C – O – F	2.08	-0.468	2
	N – O – O	11.4	-0.339	2.65
	Si – O – Si	1.31	-0.721	2
	N – O – C	8.35	-0.365	2.569
	Si – O – F	2.98	-0.4	2
	F – O – F	6.22	-0.273	2
	N – O – Si	2.91	-0.329	2.574
	N – O – F	7.6	-0.342	2.545
	N – O – N	12.4	-0.382	2.734

Table A.4: Parameters of the three-body potentials (h_{sp3} with O as central atom).

	ijk	k (eV)	Θ (°)	γ
h_{sp3}	H – N – H	3.83	-0.28	2.37
N center	O – N – H	5.61	-0.229	2.46
	C – N – H	5.05	-0.34	2.26
	O – N – O	12.7	-0.341	2.742
	H – N – Si	3.16	-0.442	1.85
	O – N – C	9.36	-0.326	2.558
	H – N – F	5.31	-0.192	2.445
	C – N – C	12.7	-0.406	2.97
	O – N – Si	5.33	-0.29	2.568
	H – N – N	6.27	-0.273	2.51
	O – N – F	12.4	-0.324	2.762
	C – N – Si	6.62	-0.498	2.67
	C – N – F	8.68	-0.3	2.515
	N – N – O	12.3	-0.342	2.619
	Si – N – Si	8.7	-0.544	3.02
	C – N – N	10	-0.36	2.58
	Si – N – F	3.86	-0.27	2.534
	F – N – F	10.5	-0.292	2.58
	N – N – Si	3.55	-0.361	2.31
	N – N – F	11.3	-0.345	2.746
	N – N – N	5	0	0

Table A.5: Parameters of the three-body potentials (h_{sp3} with N as central atom).

	ijk	k (eV)	Θ (°)	γ
h_{sp2}	O = C – H	3.2	-0.488	1.836
C center	C = C – H	2.22	-0.434	1.953
	O = C – O	5.68	-0.46	2
	C = C – O	4.59	-0.447	2
	C = C – C	4.62	-0.469	2
	O = C – Si	3.24	-0.575	2
	N = C – H	4.76	-0.412	1.88
	O = C – F	7.48	-0.575	2
	C = C – Si	3.57	-0.976	2
	C = C – F	5.4	-0.461	2
	N = C – O	14	-0.472	2.31
	N – C = O	14	-0.472	2.31
	C = C – N	14.8	-0.505	2.68
	C – C = N	14.8	-0.505	2.68
	N = C – Si	3.87	-0.448	1.94
	N = C – F	14.6	-0.437	2.37
	N = C – N	14.6	-0.475	2.43

Table A.6: Parameters of the three-body potentials (h_{sp2} with C as central atom).

	ijk	k (eV)	Θ (°)	γ
h_{sp2}	O = N – H	5.93	-0.304	2.17
N center	C = N – H	3.67	-0.373	2.2
	O = N – O	16.8	-0.373	2.65
	O = N – C	12.3	-0.412	2.61
	O – N = C	12.3	-0.412	2.61
	C = N – C	24.6	-0.492	3.8
	Si – N = O	3.11	-0.401	1.86
	N = N – H	4.64	-0.294	2.11
	O = N – F	13.1	-0.369	2.66
	C = N – Si	8.39	-0.576	3.31
	C = N – F	12.7	-0.364	2.72
	N = N – O	12.6	-0.386	2.35
	N – N = O	12.6	-0.386	2.35
	C = N – N	16.1	-0.46	3.02
	C – N = N	16.1	-0.46	3.02
	N = N – Si	3.87	-0.442	2.31
	N = N – F	13.9	-0.336	2.6
	N = N – N	5	0	0

Table A.7: Parameters of the three-body potentials (h_{sp2} with N as central atom).

	ijk	k (eV)	Θ (°)	γ
h_{sp1}	C ≡ C – H	1.08	-1	1.56
	O = C = O	6.62	-1	1.2
	C = C = O	2.44	-1	1.33
	C = C = C	2.56	-1	1.73
	N ≡ C – H	1.91	-1	1.04
	C ≡ C – Si	1.67	-1	1.13
	C ≡ C – F	2.74	-1	1.2
	N ≡ C – O	5.27	-1	1.39
	N = C = O	5.27	-1	1.39
	C ≡ C – N	4.47	-1	1.16
	C = C = N	4.47	-1	1.16
	C – C ≡ N	4.47	-1	1.16
	N ≡ C – Si	1.4	-1	1
	N ≡ C – F	4.49	-1	1.29
	N ≡ C – N	5.79	-1	1.31
	N = C = N	5.79	-1	1.31

Table A.8: Parameters of the three-body potentials (h_{sp1}).

Appendix B

Molecular configurations of regimes I, II, and III

Figure B.1 shows the side views of atomic structures at specified ion doses during the desorption step of PE-ALE of SiN. The initial structure (i.e., right after the adsorption step) is shown in (a), (b) shows the structure during the desorption step after most of the HFC layer has been removed, (c) shows the structure after the removal of the mixed SiN-HFC layer, and (d) shows the structure when the etch rate becomes similar to that of physical sputtering of SiN by Ar^+ ions.

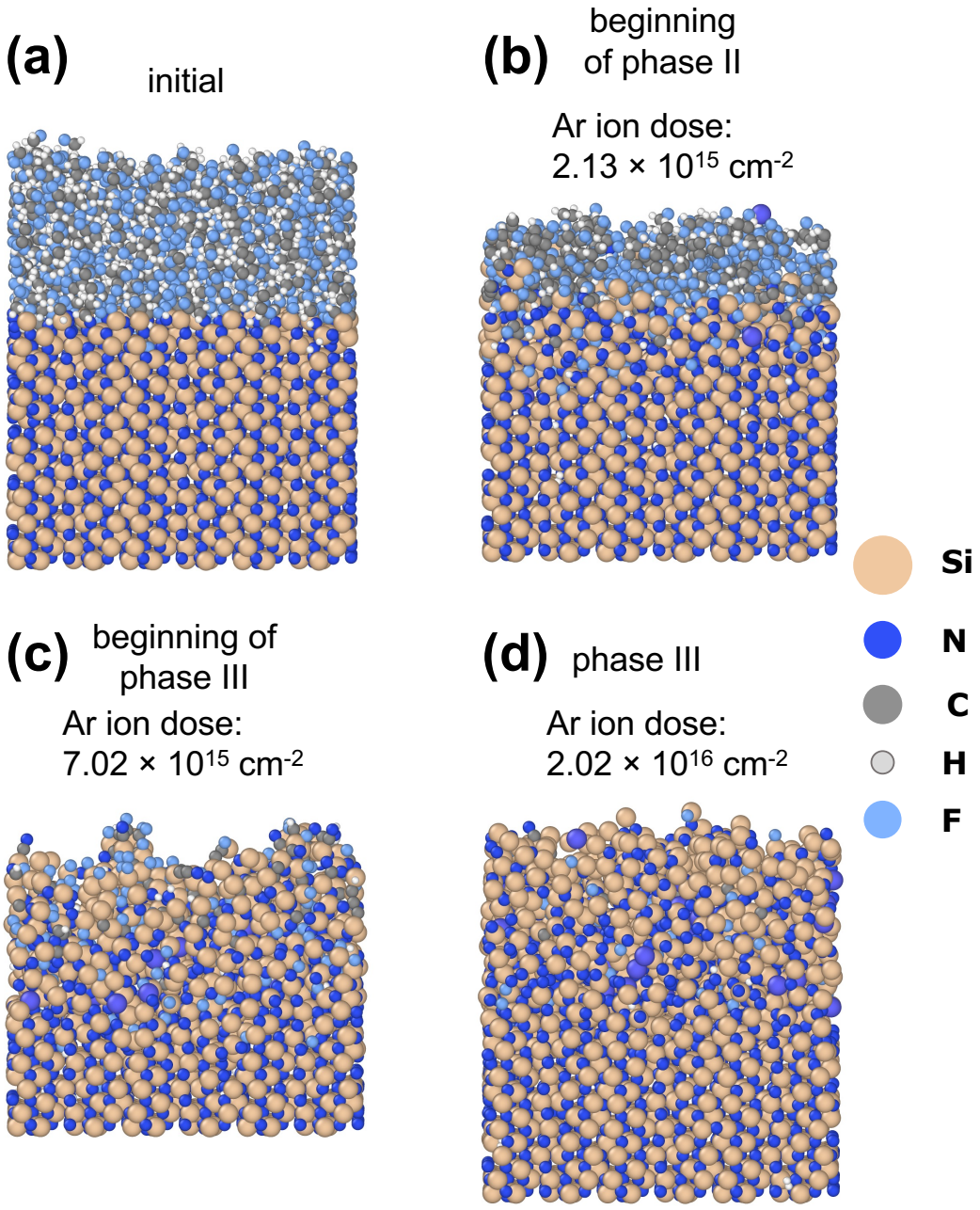

Figure B.1: Side views of the atomic structures of the system during the Ar^+ ion desorption step of PE-ALE of SiN: (a) the initial structure right after the adsorption step, (b) the beginning of phase II, (c) the beginning of phase III, and (d) at the specified ion dose in phase III.